

Evaluating Fatigue Cracks in Steel Bridges with Thermoelastic Stress Analysis

A Thesis

Presented to
the faculty of the School of Engineering and Applied Science
University of Virginia

in partial fulfillment
of the requirements for the degree

Master of Science

by

Matthew Ott Kantner

May

2012

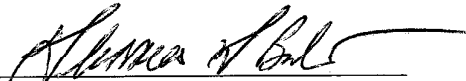
APPROVAL SHEET

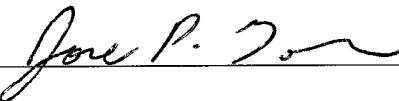
The thesis
is submitted in partial fulfillment of the requirements
for the degree of
Master of Science


AUTHOR

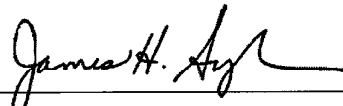
The thesis has been read and approved by the examining committee:


Advisor





Accepted for the School of Engineering and Applied Science:



Dean, School of Engineering and Applied Science

May
2012

ABSTRACT

Fatigue cracks in bridges are becoming a larger problem for the aging civil infrastructure in the United States due to ever-increasing truck loads and deficient funding for civil infrastructure. A project sponsored by the Center for Transportation Studies is looking at a new approach to evaluate high-risk bridge details. This approach is based on thermoelastic stress analysis (TSA). Much like gases, solids heat up or cool down when they are compressed and expanded, respectively. For solids this is known as the Coulomb Effect. Although the temperature change is small, when stresses are large enough it can be measured with an infrared camera. The project's goal is to use a relatively inexpensive infrared camera to monitor bridge details and evaluate stress concentrations to detect the presence of fatigue cracks or to predict the likelihood of the formation of a fatigue crack. With that knowledge, steps can be taken to mitigate the effect of the crack or prevent the crack from forming in the first place. This thesis is focused on the "proof of concept" for this project using multi-physics simulation and laboratory testing, as well as a comprehensive literature review of prior work, particularly work which relates to fatigue evaluation and bridges. Understanding the thermoelastic response to random bridge loading is the main technical obstacle in this work. This will be addressed by future work.

ACKNOWLEDGEMENTS

This research would not be possible without the sponsorship of the Mid-Atlantic Universities Transportation Center (MAUTC). This project was the brainchild of my advisor, Dr. Steve Chase. I owe him a great deal of gratitude for his guidance, willingness to answer all of my questions, and for his work, particularly with the simulation and data processing work in Matlab. The project would not have been possible without the assistance of Dr. Paul Fuchs of Fuchs Consulting, Inc.. Dr. Fuchs provided us with the camera used for the laboratory testing. His expertise with the camera and image processing was crucial to the project. Jim Danberg also provided assistance with the MTS machine. Finally I would like to thank the Civil and Environmental Engineering department at the University of Virginia, who gave me a chance to pursue this project.

Table of Contents

1.	Motivation	10
2.	Literature Review	10
2.1	Thermoelastic Stress Analysis.....	10
2.2	Use of Infrared Detector Technology	13
2.2.1	Infrared Technology Background	14
2.2.2	Thermodynamic Principles Involved	16
2.3	Lock-In Amplifier.....	20
2.4	Fatigue in Steel Bridges	25
3.	Multi-physics Modeling	29
3.1	The ANSYS Software	30
3.2	“Solid 226” Element.....	31
3.3	Cube Model	34
3.3.1	Introduction.....	34
3.3.2	Uniaxially loaded cube simulation.....	34
3.3.3	Three-dimensionally loaded cube simulation	36
3.3.4	Out-of-phase three-dimensional loading cube simulation	39
3.3.5	Non-uniform fixed load cube example.....	42
3.3.6	Conclusions from cube simulations.....	45
4.	Hole-In-Plate.....	46
4.1	Hole-in-Plate Theory.....	46
4.2	ANSYS Simulations.....	50
4.3	Matlab Simulations.....	54

4.3.1	Sinusoidal reference signal.....	54
4.3.2	Truck Event Simulations	58
4.4	Laboratory Tests	60
4.4.1	Testing Setup	60
4.4.2	Testing Procedure.....	63
4.4.3	Processing Methods	65
4.4.3.1	Determining Loading Rate with Beats	66
4.4.3.2	Idealized Sine Wave Reference Signal	68
4.4.3.3	MTS Output Reference Signal.....	69
4.4.4	Data and Analysis	71
5.	Conclusions.....	80
6.	Future Work.....	81
7.	Appendices	83
	Works Cited	110

LIST OF FIGURES AND TABLES

Figure 1: Focal plane array (FPA) schematic. Borrowed from Dulieu-Barton 1999, p. 28 (Dulieu-Barton, 1999).....	16
Figure 2: Demonstration of conduction effects on thermoelastic stress analysis	19
Figure 3: Atmospheric infrared transmission windows. Borrowed from Dulieu-Barton 1999, p. 21 (Dulieu-Barton, 1999).....	20
Figure 4: Block diagram for a lock-in amplifier.....	22
Figure 5: Lock-in Algorithm Text Output	24
Figure 6: Graphical output of Matlab lock-in algorithm.....	24
Figure 7: Illustration of web-gap distortion. Borrowed from URS report, p. 11 (URS Corporation, 2011).....	26
Figure 8: Web-gap fatigue crack on I-70 EBR bridge over Antietam Creek in Hagerstown, Md. Photo Borrowed from URS report p. 8 (URS Corporation, 2011).....	27
Figure 9: Simulation of a truck passing over the Route 15 bridge over I-66 in Haymarket, VA. Simulated stress response at 0.4L into the first span of a two-span continuous bridge	28
Figure 10: Filtered strain gage data from I-70 bridge over Antietam Creek. Borrowed from URS report p. 122 (URS Corporation, 2011). Dashed vertical lines separate 30 second intervals	29
Figure 11: Layout of a 10-Node Tetrahedral Element, from the Element Reference in ANSYS 13.0.....	32
Figure 12: <i>Temperature versus time plot for a cube under uniaxial pressure loading</i>	36
Figure 13: <i>Applied stresses to the cube in x, y, and z. The total (summed) stress is also plotted, and it completely overlaps with the x-direction stress</i>	37
Figure 14: Strain components in second cube simulation	38
Figure 15: Temperature plot for the cube under synchronized three-dimensional loading	39
Figure 16: Third cube trial applied stresses.....	40
Figure 17: Strains in the third cube trial with out of phase stresses.....	41
Figure 18: Temperature versus time graph for the out of phase stresses on the cube model.....	42

Figure 19: Loading diagram for the final cube trial	43
Figure 20: Temperature versus time plots for the four points on the cube indicated in Figure 19	44
Figure 21: Diagram for infinite plate with a hole	47
Figure 22: Effect of d/H on stress concentration factor. Borrowed from Pilkey (1997)	49
Figure 23: Von Mises stresses in the hole-in-plate ANSYS simulation	51
Figure 24: Principal stresses at point "A" of ANSYS simulation. Turquoise is total (the largest amplitude), purple is principal stress in y, light blue is principal stress in x, red is principal stress in z	52
Figure 25: Temperature results from ANSYS hole-in-plate simulation	53
Figure 26: Unfiltered image from Matlab camera simulation. This image is taken at the maximum applied stress.....	56
Figure 27: Images from Matlab simulation which have been filtered and averaged with the SimulateDataEdit file. Data acquired for 5 and 20 seconds respectively.....	58
Figure 28: Change in principal stresses in truck simulation, used as loading signal for truck simulation	59
Figure 29: Final image from 5 simulated truck events	60
Figure 30: One test specimen ready to be tested	61
Figure 31: Microbolometer imager used in laboratory testing.....	62
Figure 32: Testing schematic	63
Figure 33: A cropped, raw image taken from test A1. No TSA is possible without advanced filtering of these images	65
Figure 34: Beats example: Sine waves at 10 Hz and 11 Hz are multiplied together and the result produces beats which occur at 1 Hz.....	67
Figure 35: Sample of method used to determine actual loading frequency. This graph shows the loading signal from test C4 multiplied by a sine wave at 3.0177 Hz. The peaks are flat because 3.0177 Hz is the actual loading frequency	68
Figure 36: Comparison of results from the MTS-referenced test A1 : (a) no normalizing algorithm for reference signal (b) normalized	71

Figure 37: Camera recorded values for a pixel directly to the right of the hole (where the highest stress concentrations are) from test A1 vs. frame (30 frames per second).....	74
Figure 38: Load curve and elongation curve for the ramped test.....	79
Figure 39: Unprocessed image showing temperature variations in a specimen due to plastic deformation.....	80
Table 1: Graphic displaying deleted / retained data when reduced from 100 to 30 Hz sampling rate	70
Table 2: Index for tests and phase-shift results	72
Table 3: Quantitative analysis of final processed images.....	77

1. Motivation

One of the major problems that the United States will face in the coming years and decades is our aging civil infrastructure. Many of our nation's bridges, highways, and other transportation structures are nearing the end of their expected lifespans. The average age of a bridge in the United States is 43 years old, and most of these bridges were built to last fifty years ((AASHTO), July 2008). Unlike buildings and other structures with mainly static loading, bridges experience very dynamic loading regularly throughout their usable lives. Some steel components of bridges are stressed near their yield strength every time a fully loaded truck travels over them. Bridges experience millions of truck loadings throughout their lifetimes, and the chronic loading near the yield strength of the steel causes fatigue in the steel. Sometimes this fatigue can lead to fatigue cracking, which is a serious structural problem for the bridge. A reliable way to predict these fatigue cracks would save time and money in the long run because preventative maintenance could be used to stop the cracks from ever forming. If fatigue cracks can be predicted, and eliminated before they become a problem, the amount of time a bridge must be closed for retrofitting and maintenance can be reduced, while the lifespan of the bridge can be increased. Obviously this saves money, and potentially lives, in the long term as well.

2. Literature Review

2.1 Thermoelastic Stress Analysis

Thermoelastic Stress Analysis is a type of non-destructive evaluation which is very useful in locating areas with high stress concentrations (which are susceptible to fatigue cracking) in

steel bridges. Thermoelastic Stress Analysis relies on a basic physical effect known as the Coulomb effect. It is well known that gases change temperature with volume. The Coulomb effect is analogous for solids. As a solid material is compressed, the temperature of the material increases slightly and vice versa for a material in tension. A brief derivation of the relationships between applied stresses and temperature changes, which follows Dulieu-Barton's paper entitled "Introduction to thermoelastic stress analysis", is below (Dulieu-Barton, 1999).

The relationship between strain and thermoelastic temperature change in an isotropic, homogeneous material is governed by Equation 1.

$$\Delta T = \frac{T}{\rho C_\epsilon} \sum \frac{\partial \sigma_{ij}}{\partial T} \epsilon_{ij} + \frac{Q}{\rho C_\epsilon} \quad \text{for } i, j = 1, 2, 3 \quad \text{Equation 1}$$

Where: T is the absolute temperature of the material (i.e. K)

ρ is the density (e.g. kg/m³)

C_ϵ is the specific heat at constant strain (e.g. J/kg*K)

σ_{ij} is the stress change tensor (e.g. Pa)

ϵ_{ij} is the strain change tensor (unitless)

Q is the heat input (e.g. J)

Under adiabatic conditions (i.e. when the specimen is cycled quickly enough that no heat conduction takes place within the material) the second term in Equation 1 can be neglected. This is a reasonable assumption when the specimen is loaded at over 3 Hz (Haldorsen, 1998). The following stress-strain-temperature relationships, Equation 2, are valid for an isotropic material in a state of plane stress.

$$\begin{aligned} \sigma_{11} &= \frac{E}{(1-\nu^2)} (\epsilon_1 + \nu \epsilon_2) - \frac{E\alpha}{(1-\nu)} \Delta T \\ \sigma_{22} &= \frac{E}{(1-\nu^2)} (\epsilon_2 + \nu \epsilon_1) - \frac{E\alpha}{(1-\nu)} \Delta T \\ \sigma_{12} &= \frac{E}{(1+\nu)} \epsilon_{12} \end{aligned} \quad \text{Equation 2}$$

Where: E is the Young's modulus (e.g. Pa)
 ν is the Poisson's ratio (unitless)
 α is the linear coefficient of thermal expansion (i.e. K^{-1})

Assuming that the Young's modulus and the Poisson's ratio are independent of temperature (these "constants" do not vary substantially unless at a very high temperature; the temperature changes generated by this effect are less than $1^\circ C$) we can rewrite Equation 1 as seen below in Equation 3 (Dulieu-Barton, 1999).

$$\Delta T = \frac{T}{\rho C_\varepsilon} \frac{E\alpha}{(1-\nu)} \Delta \varepsilon_{ii} \quad \text{Equation 3}$$

Assuming a linear stress-strain relationship, and knowing the relationship between the specific heat at a constant strain and the specific heat at a constant pressure ($C_\varepsilon = C_p - \frac{2E\alpha^2 T}{\rho(1-\nu)}$), the relationship between the change in stress and the temperature change can be written as below in Equation 4.

$$\Delta T = -\frac{T_o \alpha}{\rho C_p} \Delta \sigma_{ii} \quad \text{Equation 4}$$

According to this equation, the change in temperature under ideal conditions is directly proportional to the change in volume, which is directly proportional to the first stress invariant (the sum of the principal stresses).

Thermoplastic Stress Analysis is also possible, but is much more complicated due to the complications that occur with the permanent deformation of a material at the atomic level. As inter-particle bonds break, a relatively large amount of heat is released. For this reason, a material which is being stretched beyond its plastic capacity will cool down in the elastic range,

then heat up as it begins to deform plastically. One laboratory trial was done in this work that looked at plastic deformation and its thermal effects. This is discussed in section 4.4.4.

Thermoelastic Stress Analysis has been researched before, but has never been successfully applied to civil infrastructure in the field. Boyce and Leomark tried to measure stresses on a bridge in the field but were unsuccessful. TSA has been successfully applied on specimens in the laboratory (Haldorsen, 1998). Although it is a bit dated, Haldorsen provides a very good background of TSA theory, as well as its applications (Haldorsen, 1998). There are many complications that must be dealt with in applying TSA in practice, and these are discussed later in the report. The novelty of this research is that a relatively inexpensive uncooled microbolometer camera is used for acquisition of the temperature data. Microbolometer detectors are a relatively inexpensive type of infrared detector that relies on an internal change in electrical resistance when the detector is acted on by infrared radiation. These cameras do not need to be cooled as many of the more accurate and more expensive cameras do (Kaplan, 2007). Thermoelastic Stress Analysis has been applied successfully in the past but has always relied on expensive, cooled, photon detector based cameras.

2.2 Use of Infrared Detector Technology

With the help of defense funding, infrared detector technology has improved significantly over the last few decades. New cameras which are relatively inexpensive can measure temperature over a two-dimensional array of points with speed and precision that was not possible twenty years ago. Infrared cameras detect heat radiation from a material to accurately gauge the temperature in a non-contacting manner. The advancement of infrared

cameras is the impetus behind this research. Because the price of the cameras continue to fall and sensitivity continues to improve, technology has improved to the point where using these cameras regularly in the field may not be too costly. Ultimately, the “product” that this research hopes to deliver will rely heavily on commercially available infrared detection technology.

2.2.1 Infrared Technology Background

The military’s desire for night-vision goggles was the impetus behind the early advancement of IR camera technology. These real-time cameras were first deployed in the 1970s (Kaplan, 2007). These early cameras used a mechanical scanning mirror to produce a two-dimensional image. Until recently, many of the best cameras used this type of technology, which was slow and prone to mechanical problems. There are a myriad of infrared cameras available today. Many of them are used for qualitative information, and do not record temperatures. Others are called measuring infrared cameras, and they record temperatures with varying levels of precision. Some high-end models, which can cost over \$200,000, can measure temperatures across an array with accuracy down to 0.001°C . This is precise enough to measure stress changes of 1MPa in steel or 0.4MPa in aluminum (Hardwood & Cummings, 1991). Less expensive microbolometer based models, which cost around \$10,000 can measure temperature as precisely as about 0.05°C to 0.07°C . The temperature changes expected from mild steel which is loaded cyclically near its yield limit is around 0.20°C (Hardwood & Cummings, 1991), so these stresses should be visible with a relatively inexpensive microbolometer camera.

There are two main types of infrared radiation detectors: thermal detectors and photon detectors. Photon detectors are made of semiconductors. When a carrier becomes excited by an

incident photon, it moves to a mobile conduction band. Thermal detectors change temperature due to the incoming radiation, and this change in temperature causes a change in another property of the detector. For example, the temperature change causes a change in resistance in a bolometric detector, the optical properties of a liquid crystal detector, or the electric field properties in a pyroelectric detector (Hardwood & Cummings, 1991).

The camera which is used for this research has a microbolometer detector which operates in the $7.5\mu\text{m}$ to $13\mu\text{m}$ range. The advantage of operating in this range is that it has a more consistent and higher transmissivity through air. One disadvantage to this range is that ordinary glass is opaque in this range; however other materials can be used for optics (Kaplan, 2007). The detector which is used for this research is very similar to the FLIR A325 camera. The difference is that the FLIR A325 is a full camera package which has mechanical focusing, on-board digital processing, and a 60 Hz imaging rate. The “thermal imager” that we are using is essentially just a microbolometer detector without any on-board aids. It also has only half the frame rate of the A325, at 30 Hz. It uses a Focal Plane Array (FPA). This is called a staring imager, because it can measure the temperature at all points in the image simultaneously without any moving parts. All modern IR cameras utilize focal plane arrays, a schematic for which can be seen in Figure 1. Older imagers used internal moving mirrors to scan an entire image. The A325 (as well as the detector used in this research) has an image size of 256 by 324 pixels and a thermal sensitivity of less than 0.07°C (FLIR Systems, Inc., 2008).

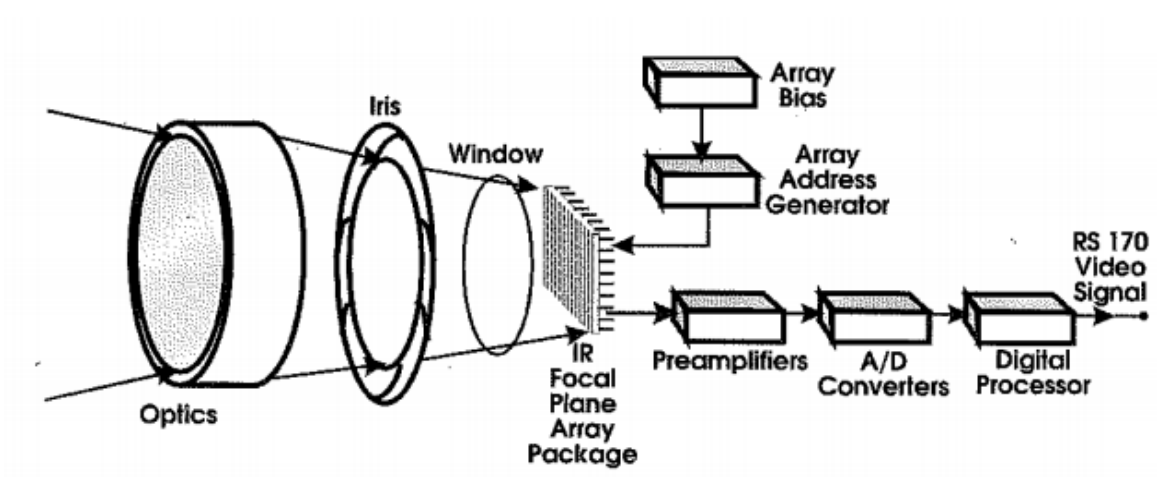


Figure 1: Focal plane array (FPA) schematic. Borrowed from Dulieu-Barton 1999, p. 28 (Dulieu-Barton, 1999)

2.2.2 Thermodynamic Principles Involved

With some theoretical exceptions, all materials radiate energy. When some materials get hot, they even radiate energy in the visual spectrum (e.g. “red-hot” molten steel). Even at lower temperatures, materials radiate energy, but not in the visual spectrum. At lower temperatures, one of the best ways to “see” the energy radiation of a material is in the infrared (IR) spectrum. The IR spectrum has longer wavelengths than the visible spectrum, but shorter than radio waves (Kaplan, 2007). In this infrared spectrum it is possible to detect the amount of energy radiating off of a surface, and calculate its temperature from the energy.

The three methods of heat transfer are conduction, convection, and radiation. This research is most interested in radiation, but it is important to understand the other two because they can affect the amount of radiation measured by an IR camera. Conduction is the transfer of

heat from a material to another stationary material that it is touching (Kaplan, 2007). Conduction creates a problem for thermoelastic stress analysis testing, because if a load is not applied rapidly, the heat built up at stress concentrations transfers, via conduction, to nearby material (because the specimen tries to obtain thermal equilibrium in the absence of an active load). This can also be problematic in the laboratory, but can be easily overcome by increasing the loading frequency. Figure 2 depicts this phenomenon. In this example, a pressure load is applied upwards at the red part of the component. This load is a step pressure load which is instantaneously applied and then remains constant throughout the simulation. The temperature concentrations are obvious in the first image, taken just as the pressure is applied. In the second image, taken about 0.94 seconds later, conduction has already redistributed much of the heat away from the areas under the most stress.

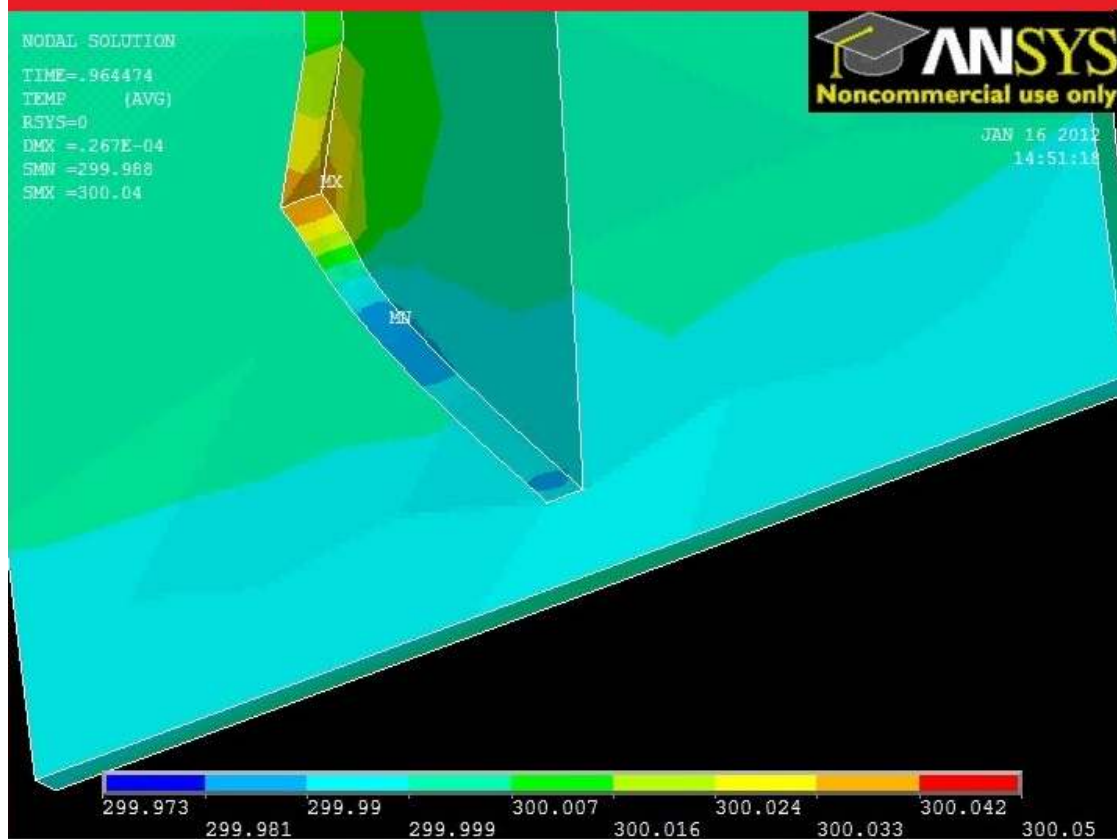
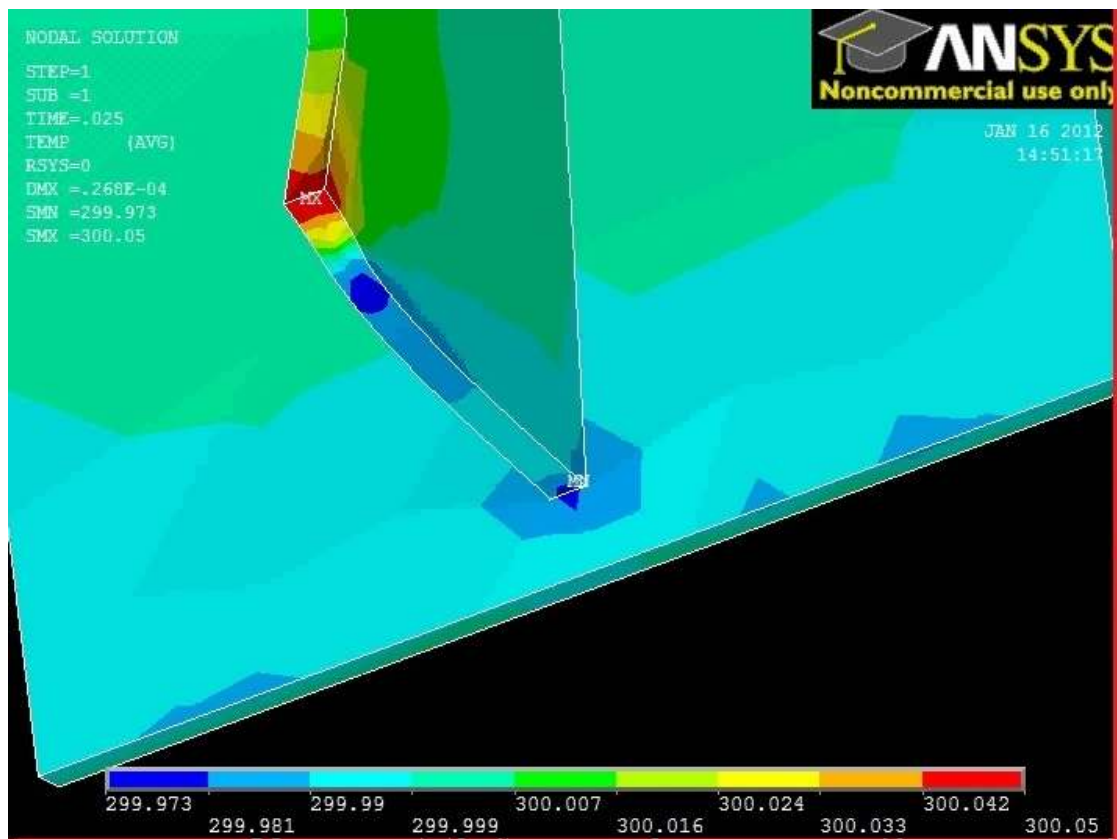


Figure 2: Demonstration of conduction effects on thermoelastic stress analysis

The next method of heat transfer, convection, transfers heat from an object to a moving medium (e.g. air) (Kaplan, 2007). Convection is the reason that there is a “wind chill” factor. On a cool day, the wind can steal the heat from one’s skin and make one feel much colder. Convection is another hurdle that must be overcome in field testing, because there is wind in the field and it is very unpredictable. We will try to mitigate wind’s effects by shielding the area under test from the wind.

Radiation is the third method of heat transfer, and is the most important one for the purposes of this research. Radiation is the fastest of the three methods. All real objects radiate energy. Two fundamental and important equations model the amount of radiation, as well as the peak wavelength of radiation. They are the Stephan-Boltzmann law (Equation 5) and Wien’s displacement law (Equation 6) respectively.

$$W = \delta \epsilon T^4 \quad \text{Equation 5}$$

Where: W = radiant flux emitted per unit area (e.g. W/cm^2)

ϵ = emissivity (unitless, 1 for a blackbody)

T = absolute temperature of the body (e.g. K)

δ = Stephan-Boltzmann constant = $5.673 \times 10^{-12} \text{ watts} \cdot \text{cm}^{-2} \cdot \text{K}^{-2}$

*note: a blackbody is a perfect emitter; a material that absorbs all of the energy that acts on it

$$\lambda_m = \frac{b}{T} \quad \text{Equation 6}$$

Where: λ_m = wavelength of maximum radiation (e.g. μm)

b = Wien’s displacement constant = $2897 \mu\text{m} \cdot \text{K}$

As always, there are more complications in practice than in the theory. Air has constituents which absorb infrared radiation, such as suspended water particles and CO_2 , and this

creates a “window”, or rather, two windows through which IR radiation is best measured. Those two windows, with high transmissivity through the atmosphere, are at roughly 1-5 μm and 8-14 μm (Kaplan, 2007) (see Figure 3). Because of this phenomenon, IR cameras are produced to operate in one of these windows or the other. The camera used in this research is a microbolometer camera which operates in the 8-14 μm window.

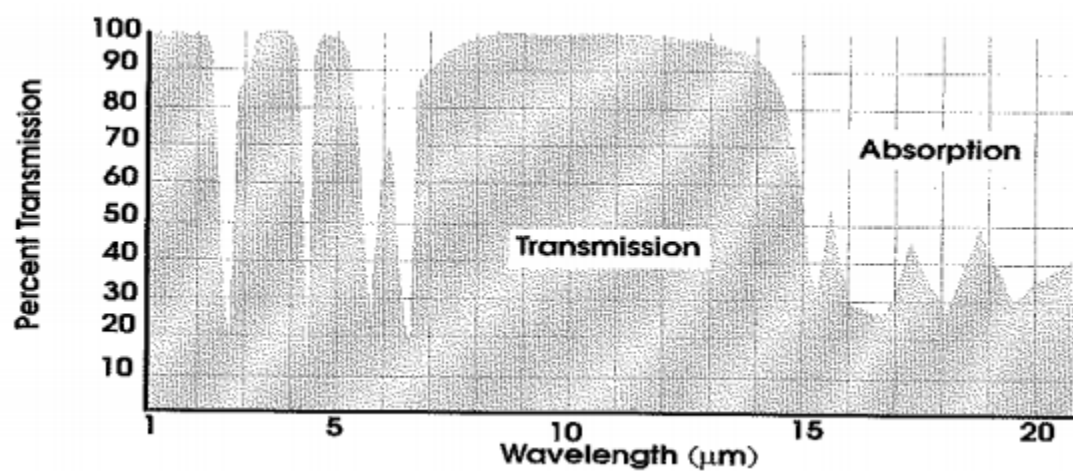


Figure 3: Atmospheric infrared transmission windows. Borrowed from Dulieu-Barton 1999, p. 21 (Dulieu-Barton, 1999)

2.3 Lock-In Amplifier

One of the inherent difficulties of attempting TSA with a relatively inexpensive camera is that the temperature changes are very near the absolute sensitivity of the camera. This means that there will be a weak signal buried in noise. One way to try to isolate the true signal is to use a bandpass filter. This is a very basic analog signal processing technique which essentially passes the signal through a low pass filter (filtering out high frequency noise) and a high pass filter

(filtering out low frequency noise). The problem with this technique is that the attenuation outside of the desired frequency is not very sharp, so it still allows a good deal of noise which is near the signal frequency to pass through. Furthermore, if the signal is extremely noisy, the bandpass filter may filter out some of the signal itself. Other possible techniques include signal averaging, digital filters, and Fourier transforms (Guinon, Ortega, García-Antón, & Pérez-Herranz). These techniques are useful, but would be insufficient to pull a signal which is truly buried in noise.

A better technique which can be used for TSA is known as a lock-in amplifier. This technique can pull a discrete signal out of very deep noise if there is a known reference signal (one which behaves in the same way as the expected signal). Lock-in thermography has been used before in TSA, and Agema Infrared Systems AB even offered a lock-in unit that plugged directly into its camera (Haldorsen, 1998). The good thing about TSA in the laboratory is that the expected signal is known. An exact loading signal (i.e. force vs. time) can often be extracted from the loading apparatus. Even if this is not possible, a well-placed strain gage can provide a signal which is very highly correlated to the loading. With this reference signal (either directly from the loading apparatus or a strain gage), a lock-in amplifier can be used to pull out the buried signal. A block diagram for a lock-in amplifier can be seen in Figure 4. Basically, the noisy signal which is being measured is multiplied by the reference signal, then passed through a low-pass filter, and then integrated over a period of time (i.e. the average is found). Because most of this is being done digitally, the “integration” can be accomplished with a simple arithmetic mean of the data points. The multiplier is a phase-sensitive detector (PSD). When this process is done completely with analog electronics, the output is a DC signal which corresponds to the true signal value. Digital processing gives a scalar value which is related to the original signal intensity.

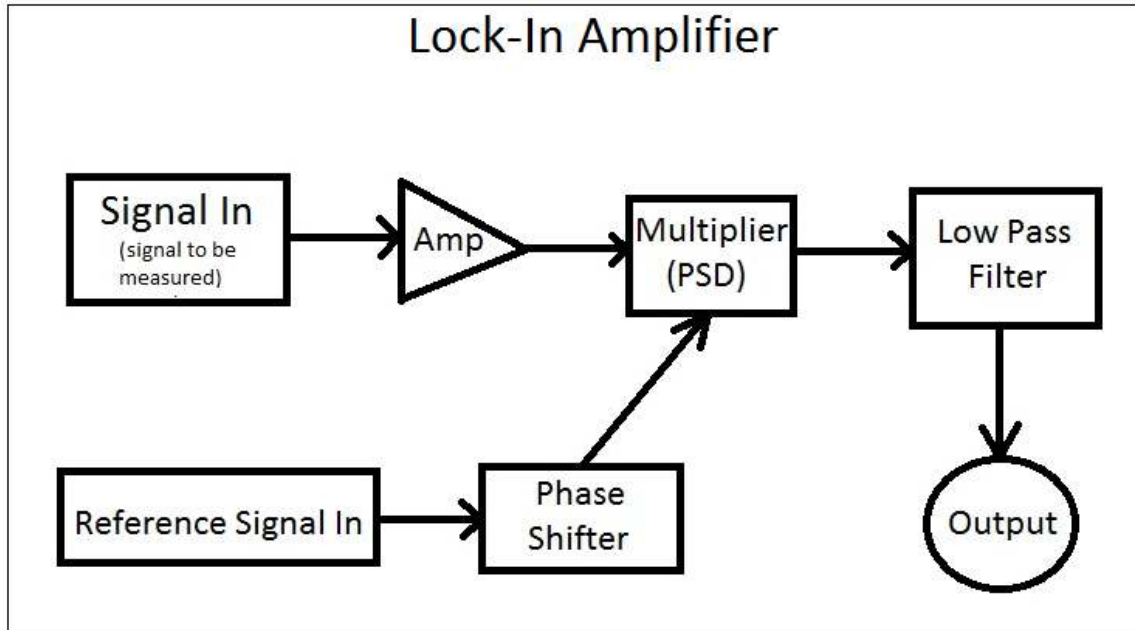


Figure 4: Block diagram for a lock-in amplifier

The code for a simple Matlab program which simulates a lock-in amplifier can be seen in Appendix C. This simple program allows the use of all preset values which can be easily changed if desired. The noisy signal (which is meant to simulate noisy signals read by an IR camera or other measuring device) is generated by summing a sine wave with a constant background temperature and a random number at each data point. The amount of noise can be changed by the user. By default, it is set to create random numbers with a normal distribution with a mean of 0 and a standard deviation of 5. This makes very noisy signals considering that the default amplified signal only varies by 2 from peak to peak.

The results are different each time the program is run with the default settings because of the random number added to each data point. One example of the results from this program can be seen in Figure 6. The graph in the top-left shows the signal with random noise (i.e. what would be obtained by a single pixel from an IR camera). The graph in the top-middle shows the reference signal (i.e. what would be obtained from the loading apparatus or strain gage). The

graph in the top-right shows the signal after it has gone through the “lock-in” process which includes multiplication by the reference signal and filtering through a low-pass Butterworth filter. The Butterworth filter was chosen because it has a flatter passband. The other three graphs show the multiplied signal without going through the low-pass filter, the original signal (not multiplied by the reference signal) going through a low-pass filter, and the original signal passed through a bandpass filter, respectively. These are shown to demonstrate the relative effectiveness of the lock-in procedure.

A related technique that can be used to determine the appropriate frequency for the reference signal is based on the following trigonometric identity, Equation 7.

$$\sin(a) \cdot \sin(b) = 0.5 \cdot \cos(a-b) - 0.5 \cdot \cos(a+b) \quad \text{Equation 7}$$

Using this identity we can express the output of the PSD as two separate signals. The additive one oscillates at the combined frequency of the measured signal and reference signal. The frequency of the subtractive one is the difference between the frequencies of the measured signal and reference signal. Because we have declared that both of the signals operate at 5 Hz in this example, u is constant and v oscillates at double the specified frequency. This is simply a demonstration, but this technique can be used to see if there is a difference between the measured frequency and reference frequency. If the subtractive signal oscillates, the reference signal frequency should be adjusted accordingly.

The text output of one run of this script is below in Figure 5

```

>> buttered
Average of P: 0.5047
Integral of P divided by total time (should be ~= to mean): 0.5080
Average of noisy signal: 99.9875
Extrapolated range of signal: 2.0188
Actual range of signal: 2

```

Figure 5: Lock-in Algorithm Text Output

The extrapolated range in this case is very close to the actual range (without noise) of the signal.

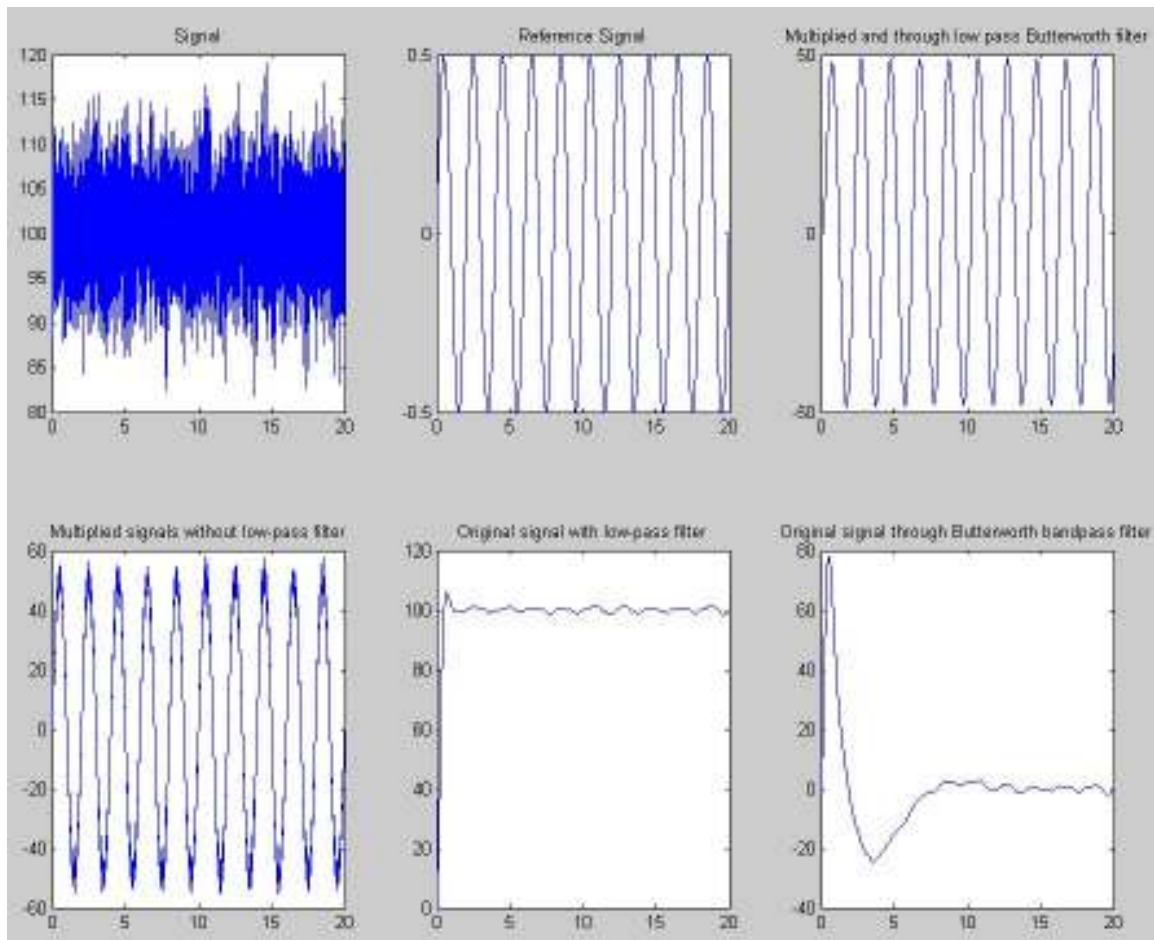


Figure 6: Graphical output of Matlab lock-in algorithm

After the very noisy signal is processed, it looks very clean. Clearly, running the multiplied signal through a low-pass filter also helps clean it up. Taking the average of this over time is the same as taking the integral of the whole wave divided by the total amount of time.

2.4 Fatigue in Steel Bridges

Fatigue in steel bridges is a problem that will only be more prevalent in the coming years. As a bridge is loaded and unloaded time and time again (by trucks passing over it), the cyclical stresses in some components of the bridge can lead to fatigue cracking. There are several different types of details which are particularly susceptible to fatigue problems. One of them is the web gap. When a stiffener or bracing element is attached directly to a web, often times a small gap is left between the element and the flange. This gap avoids welding in on tension flanges. It is also very often the case that the web stiffener is used as a connection for cross frames and diaphragms. When the bridge is loaded by a truck, the bridge deforms and can produce distortion (i.e. a larger displacement in one girder compared to another). This can produce a moment in the stiffener or bracing element which makes it deform (see Figure 7). This deformation can produce very high stress concentrations at the web gap if the flange is restrained, as is the case when it is rigidly attached to a concrete deck. These distortion-induced stresses can approach yield, which often leads to fatigue cracking (see Figure 8). Most fatigue cracking in steel bridges is due to this distortion-induced fatigue (Fisher, Jin, Wagner, & Yen, 1990).

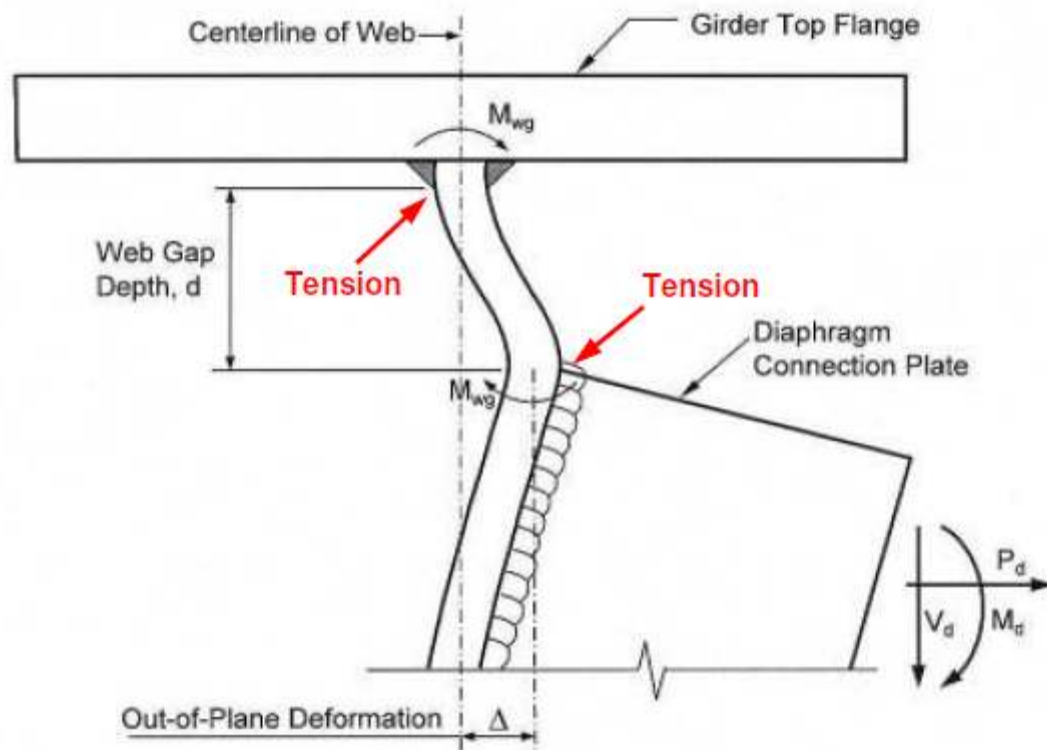


Figure 7: Illustration of web-gap distortion. Borrowed from URS report, p. 11 (URS Corporation, 2011)



Figure 8: Web-gap fatigue crack on I-70 EBR bridge over Antietam Creek in Hagerstown, Md. Photo Borrowed from URS report p. 8 (URS Corporation, 2011)

Bridges undergo random loading, and the loading cycles are slow relative to the mechanical machinery that TSA is often used to diagnose. This is the primary technical problem in applying TSA to civil infrastructure. Generally, for TSA to be accurate, testing must be performed under adiabatic conditions, which generally means that a specimen must be loaded cyclically and at a fairly high rate. Even using advanced analysis techniques, a perfect sinusoidal loading must generally be used at a minimum of 1 Hz (Haldorsen, 1998). Typical loading must be faster to avoid non-adiabatic effects. Bridges, which are loaded by trucks, are loaded at a rate much slower than 1 Hz (see Figure 9), and the intensity of the loading depends on the weight of each truck, its speed, which lane it is in, and so on. These events take place over several seconds. The

simulation seen in Figure 9 shows that the event takes place over about four seconds, but a longer bridge or slower-moving truck can make the event occur at an even slower rate. While the entire loading event has a duration of several seconds, the loading has a rise time of less than 1 second and approaches the theoretical adiabatic conditions. This is a technical hurdle which will be one of the main foci of the next phase of this research.

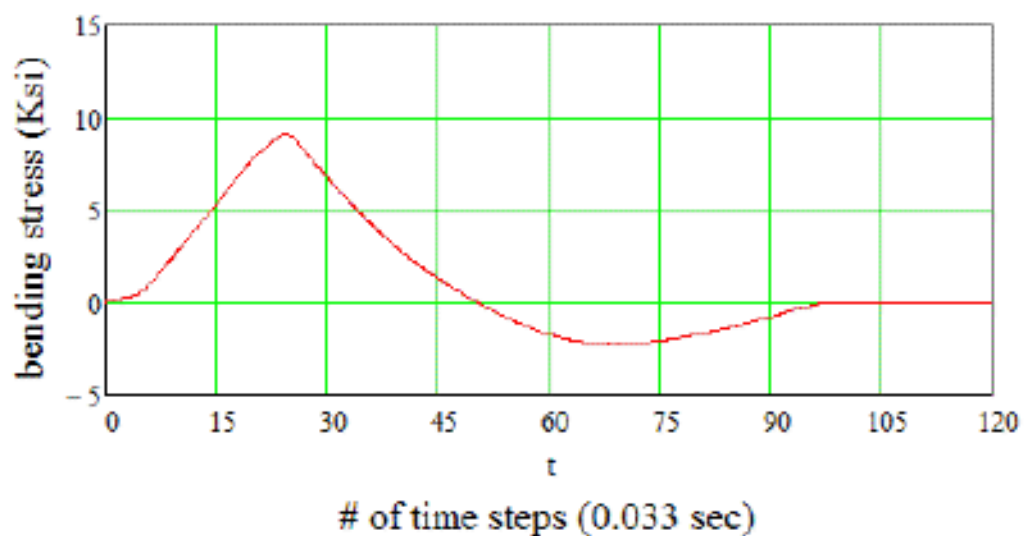


Figure 9: Simulation of a truck passing over the Route 15 bridge over I-66 in Haymarket, VA. Simulated stress response at 0.4L into the first span of a two-span continuous bridge

Actual strain gage data from the URS report on the I-70 bridge over Antietam Creek can be seen in Figure 10. This data is the filtered response of a strain gage located in a web gap of an interior girder of the center span. The strain gage is oriented vertically (URS Corporation, 2011). This data shows that the strains (and therefore stresses) can be quite high in a web gap. These stresses, which can approach the yield strength, are strong enough to be detected with TSA.

Maximum strains seen here are around 375 microstrain, which corresponds to a stress of 11 ksi in steel.

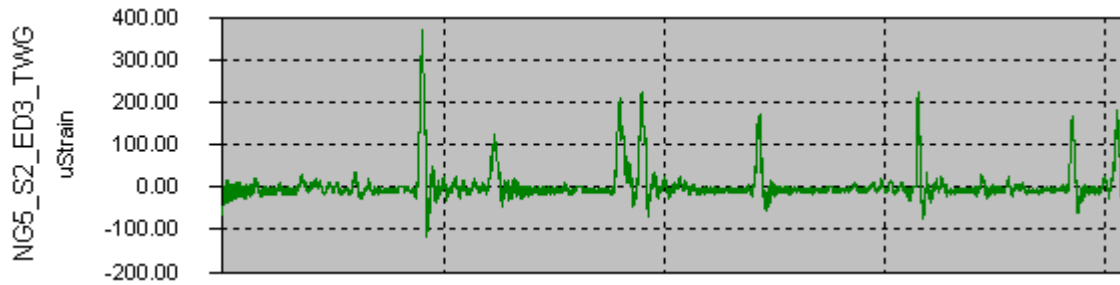


Figure 10: Filtered strain gage data from I-70 bridge over Antietam Creek. Borrowed from URS report p. 122 (URS Corporation, 2011). Dashed vertical lines separate 30 second intervals

Part of the reason that these web gaps are so prone to cracking is that a very small web gap can produce a triaxial constraint which causes there to be a three-dimensional state of stress. When this happens, the steel does not act ductily. Stresses continue to increase beyond the yield strength, but the steel does not actually yield (see section 3.3.3). Cracking occurred on the Hoan Bridge in Milwaukee, Wisconsin because of this phenomenon (Federal Highway Administration, 2010).

3. Multi-physics Modeling

The general purpose Finite Element Modeling software ANSYS was used to model specimens under simulated stresses in order to better understand the possible outcomes of TSA in practice, as well as to have a theoretical benchmark to compare lab and field results against.

ANSYS is a multi-physics finite element modeling software that has a large library of elements which can be used to accurately model very complex physical systems. For the purpose of this research, the element “Solid 226” is used. This element has three-dimensional displacement as well as temperature degrees of freedom. It is possible to model virtually any shape or component with any desired loading using this element in ANSYS. Once a simulation is completed, ANSYS allows the user to isolate any node on the model and view how its properties (stress, strain, temperature, displacement, etc.) change over time. ANSYS can also generate contour plots of any variable at any time, and it can also produce videos of these contour plots changing over time. This is very useful, because the temperature is seen this way with an infrared camera.

3.1 The ANSYS Software

ANSYS is one of the most prominent multi-physics modeling software suites in the world. This project used the Mechanical APDL package of software developed by ANSYS. This software uses finite element techniques to solve problems which would be extremely tedious, if not impossible, to solve by hand. The program has many built-in elements with varying numbers of nodes, degrees of freedoms, geometries, and uses. It also allows users to create their own elements. ANSYS is capable of handling phenomena such as strain hardening, non-linear stress/strain relationships, and large deflections for most elements. Virtually any physical component or process can be modeled using ANSYS, but modeling components for a specific phenomenon, such as thermal changes in a solid under stress, requires only a specific knowledge of the program. ANSYS has command-line input, batch processing, and a GUI which can all be used to set up a problem. Once a problem has been set up, a solution can be found and the results are displayed. The solution can be set to keep track of as many or as few quantities as

desired. There are many different ways to display results, such as contour plots, graphs vs. time, tables, etc.

Once an appropriate element is chosen and an object is modeled and meshed, a variety of different solutions can be formed. The most basic solution is a static solution which provides stresses, strains, displacements, etc. at each node. Another solution option is a modal solution, which extracts the natural frequencies and mode shapes of a model. Videos of mode shapes can be exported and viewed.. Harmonic analysis determines the response of a model to harmonically time-varying loads. A spectrum analysis determines the model's response to random vibrations. A buckling analysis calculates the buckling loads and shapes of the input structure. This is very useful (and compares favorably to the theoretical values) for eigenvalue plate buckling problems. A Transient analysis determines the response of a model throughout varying load steps (ANSYS, Inc., 2010). The transient analysis option is the option which was used most often in this research. Any time-varying load, such as sinusoidally varying temperatures or pressures which vary as time functions, can be used in this solution. Transient solutions produce a large amount of data because the program is essentially running a full static analysis at each time step, and there can be hundreds of time steps. Once a model is created, any number of solutions can be generated. For example, throughout this research a web-gap ANSYS model was created and used for a variety of tests. Different time-varying loadings were applied and transient analyses were run. In addition to the transient solutions, modal and harmonic analyses were run to make sure that the loads weren't varying near natural frequencies.

3.2 "Solid 226" Element

The Solid 226 Element is a “coupled” element, meaning that it has structural properties that are coupled with other physical properties. This element has several different capabilities for modeling coupled phenomena, such as structural-thermal, piezoresistive, electroelastic, and structural-thermoelectric (ANSYS, Inc.). The structural-thermal setting is used for this research. Using this setting, each node has four degrees of freedom: displacement in x, displacement in y, displacement in z, and temperature. The element has four different geometric configurations: brick (20 nodes), wedge (15 nodes), pyramid (13 nodes), and tetrahedron (10 nodes, also called Solid 227). Unless the model is very simple, using the brick geometry is impossible. When ANSYS meshes a fairly complicated surface automatically it generally uses the tetrahedron shape because it can easily accommodate irregular shapes and sharp angles. The matrices and vectors which the Solid 226 element uses to perform its calculations can be seen below in Equation 8 to Equation 14. These come from the Theory Reference for the Mechanical APDL and Mechanical Applications (ANSYS, Inc.). The following image, Figure 11, shows the general form of a tetrahedral element.

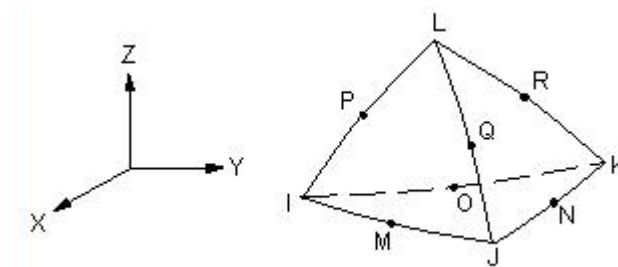


Figure 11: Layout of a 10-Node Tetrahedral Element, from the Element Reference in ANSYS 13.0

The following three equations, which are equations 12-182, 12-183, 12-184 in the Element Reference, are the interpolation functions of the element. These equations, in matrix

form, are used to produce the element stiffness matrices. They are also used to form the thermal expansion vector as well as the mass matrix.

$$u = u_i(2L_1-1)L_1 + u_j(2L_2-1)L_2 + u_k(2L_3-1)L_3 + u_l(2L_4-1)L_4 + 4u_mL_1L_2 + u_nL_2L_3 + u_oL_1L_3 + u_pL_1L_4 + u_qL_2L_4 + u_rL_3L_4$$
Equation 8

$$v = v_i(2L_1-1)L_1 + v_j(2L_2-1)L_2 + v_k(2L_3-1)L_3 + v_l(2L_4-1)L_4 + 4v_mL_1L_2 + v_nL_2L_3 + v_oL_1L_3 + v_pL_1L_4 + v_qL_2L_4 + v_rL_3L_4$$
Equation 9

$$w = w_i(2L_1-1)L_1 + w_j(2L_2-1)L_2 + w_k(2L_3-1)L_3 + w_l(2L_4-1)L_4 + 4w_mL_1L_2 + w_nL_2L_3 + w_oL_1L_3 + w_pL_1L_4 + w_qL_2L_4 + w_rL_3L_4$$
Equation 10

The following two equations, which are equations 12-57 and 12-58 in the Element Reference, are used to form the pressure load vector for the element.

$$u = u_i(2L_1-1)L_1 + u_j(2L_2-1)L_2 + u_k(2L_3-1)L_3 + u_l(4L_1L_2) + u_m(4L_2L_3) + u_n(4L_3L_1)$$
Equation 11

$$v = v_i(2L_1-1)L_1 + v_j(2L_2-1)L_2 + v_k(2L_3-1)L_3 + v_l(4L_1L_2) + v_m(4L_2L_3) + v_n(4L_3L_1)$$
Equation 12

The following equation, which is equation 12-185 in the Element reference, is used to form the thermal conductivity matrix and the heat generation load vector.

$$t = T_i(2L_1-1)L_1 + T_j(2L_2-1)L_2 + T_k(2L_3-1)L_3 + T_l(2L_4-1)L_4 + 4T_mL_1L_2 + T_nL_2L_3 + T_oL_1L_3 + T_pL_1L_4 + T_qL_2L_4 + T_rL_3L_4$$
Equation 13

The following equation, which is equation 12-63 in the Element Reference, is used to form the convection surface matrix and the load vector.

$$T = T_i(2L_1-1)L_1 + T_j(2L_2-1)L_2 + T_k(2L_3-1)L_3 + T_l(4L_1L_2) + T_m(4L_2L_3) + T_n(4L_3L_1)$$
Equation 14

Thermoelastic stiffness and damping matrices are formed by the combination of the stiffness and thermal conductivity matrices. In all of these equations, the “L” terms are barycentric coordinates of the nodes and the “T” terms are temperature.

3.3 Cube Model

3.3.1 Introduction

The easiest way to demonstrate the thermoelastic modeling capabilities of ANSYS is to create a very simple model and apply a time-varying load to it. A simple cube is the perfect model for to demonstrate these capabilities. One of the .lgw files (the text format in which ANSYS saves batch commands) which was used to run a cube simulation can be seen in Appendix B. This simulation uses the Solid 226 element and the “steelSIunits” materials property file, the values of which can be seen in Appendix A. The values in this file were obtained from various online sources, and represent the values for a typical structural steel. The cube itself has 1cm sides. It is tightly meshed.

3.3.2 Uniaxially loaded cube simulation

For the first trial, a uniaxial load is applied. The cube is fully fixed in the corner at the origin (one of the lower corners), and the whole bottom face of the cube is fixed in y (the vertical direction). A pressure (i.e. a uniform load) is applied on the top face of the cube. It is a sinusoidally varying load oscillating between 0 and a maximum value in compression at 5 Hz. The

solution is run every .0025 seconds which is 8 times per oscillation. Because the entire face is loaded and the entire opposite face is fixed there is a spatially constant state of stress throughout the cube which is equal to the applied stress at all times.

As expected the stress is distributed consistently throughout the cube, with the stress throughout being exactly equal to the applied stress at all times. The entered modulus of elasticity is 200 GPa, so the y-strain at any point in the cube should be $-\text{current applied strain}/2 \times 10^{11}$. The Poisson's ratio is 0.30, and therefore the strains in both the x and z directions should be $(\text{current applied strain} \times .30) / 2 \times 10^{11}$. The results reflect this directly. X and z stresses are negligible. Stress in the y direction peaks at 100 MPa and follows a nice sinusoidal shape. Strain throughout the cube is exactly as expected. At max amplitude applied stress, the y strain is -.0005 and the x and z strain are .00015.

Based on Equation 4 we expect a temperature change of 0.101 °C when the total stress is 100 MPa. Anecdotally, Hardwood and Cummings state that a change of .001 °C correlates to a total stress of about 1 Mpa in steel (Hardwood & Cummings, 1991), so a value of around 0.100 °C can be expected from 100 MPa of stress (and 0.05 °C from 50 MPa, etc.). The following graph, Figure 12, shows the actual temperature value for all points on the cube over time.

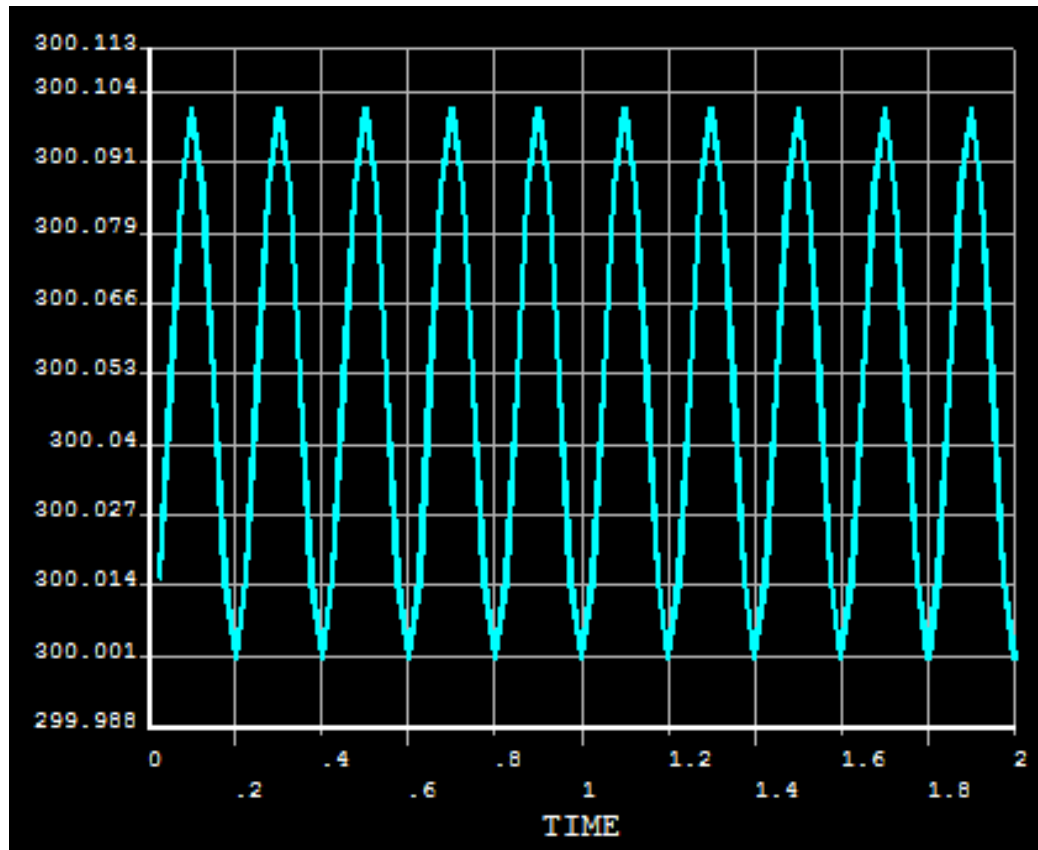


Figure 12: Temperature versus time plot for a cube under uniaxial pressure loading

This graph shows exactly what we expect. The temperature varies sinusoidally from 300.000 K to 300.101 K. This means that the change in temperature from the 100 MPa loading was 0.101 °C, which is very close to the 0.100 °C predicted with Hardwood and Cummings' rule of thumb, and exactly what Equation 4 predicts. The ANSYS modeling software gives us exactly what is predicted by the theory.

3.3.3 Three-dimensionally loaded cube simulation

The next trial tests the ability of ANSYS to deal with a three-dimensional state of stress for thermoelastic applications. A pressure is applied to each of three sides while their

complementary side is held stationary. The maximum pressures are: 50 MPa compression in x, 100 MPa tension in y, and 100 MPa compression in z. All loads are applied sinusoidally, in phase at 5 Hz. As in the first test, the state of stress is spatially constant throughout the cube. Figure 13 shows how the stresses vary with time.

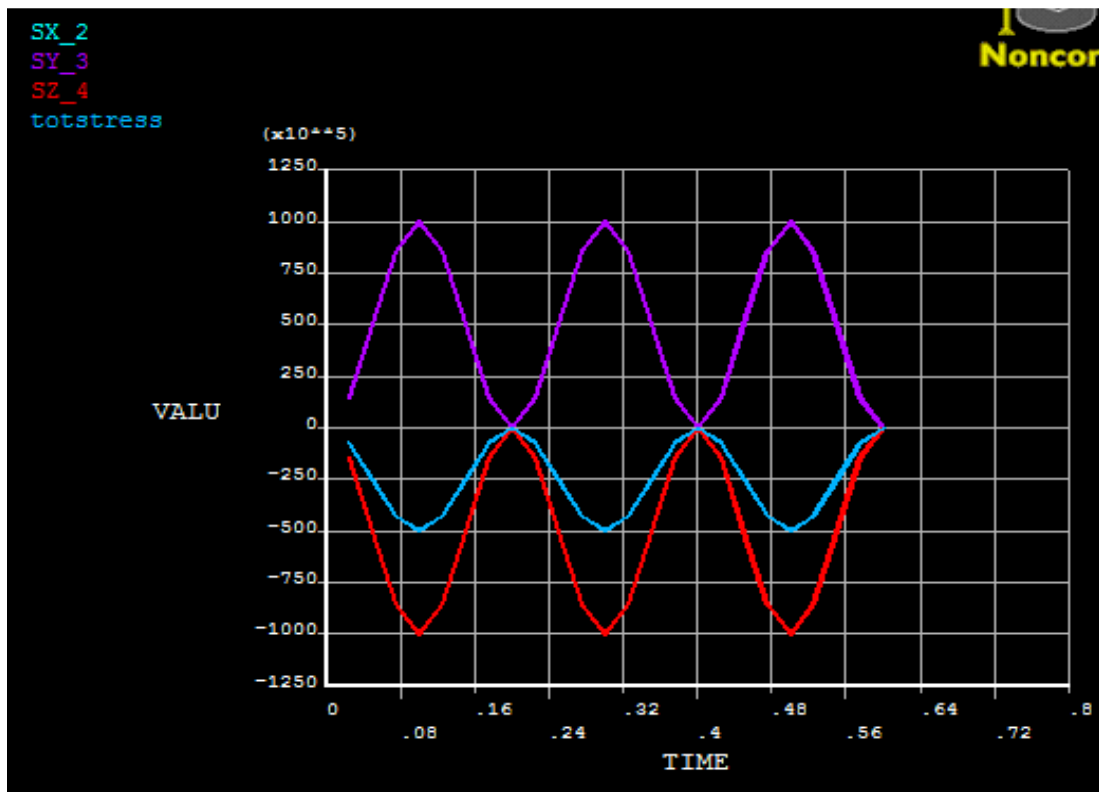


Figure 13: Applied stresses to the cube in x, y, and z. The total (summed) stress is also plotted, and it completely overlaps with the x-direction stress

The graph which shows the strains in the principle directions versus time, Figure 14, is very similar, and represents exactly what is predicted by the entered Young's modulus.

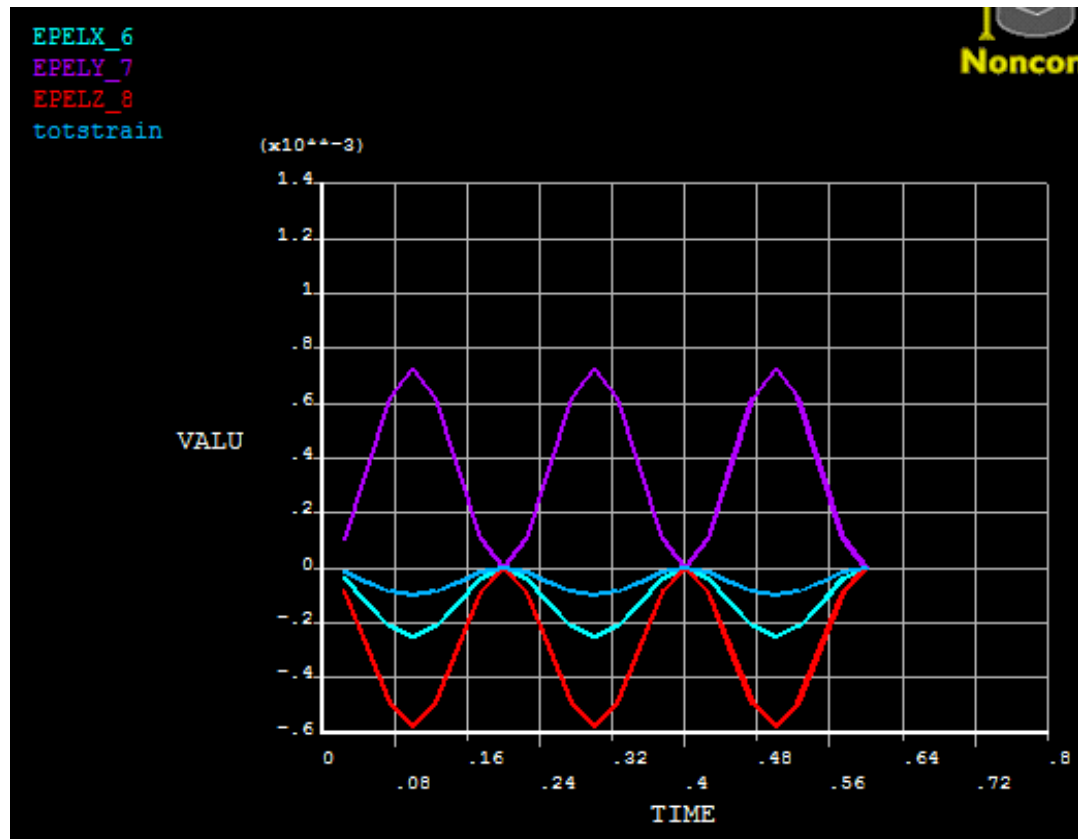


Figure 14: Strain components in second cube simulation

This cube is under a three-dimensional state of stress. To verify that this is what is expected, we will look at some of the peak values of strain. For example, we see that the strain in the y peaks at 0.725×10^{-3} . Theoretically it should be $100 \text{ MPa} / 200000 \text{ MPa}$ (this is the component of strain that comes directly from the 100 MPa tension applied in the y direction) + $.3 \times 50 \text{ MPa} / 200000 \text{ MPa}$ (the component from the Poisson effect from the 50 MPa x-direction compression) + $.3 \times 100 \text{ MPa} / 200000 \text{ MPa}$ (the component from the Poisson effect from the 100 MPa z-direction compression). All of this, of course, assumes that the material is linearly isotropic, as steel is, and that all the stresses are below the yield limit, which they are. This calculation yields a value of $.725 \times 10^{-3}$, exactly what was calculated in ANSYS. Similar calculations can be done for the other peaks, or for any other value along any of the lines. All of the hand

calculations agree exactly with the values predicted by ANSYS. The temperature plot for the cube can be seen below in Figure 15.

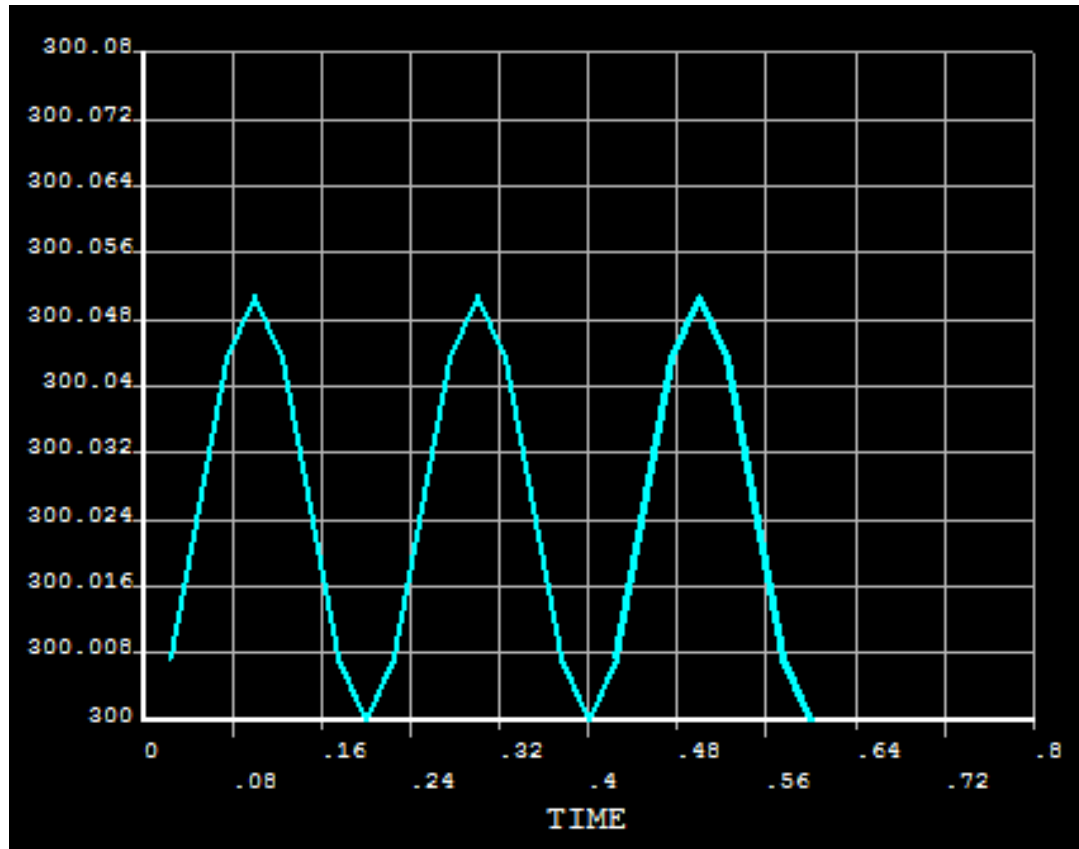


Figure 15: Temperature plot for the cube under synchronized three-dimensional loading

From the total stress of 50 MPa in compression, Equation 4 predicts a temperature change of 0.505 °C. This is exactly what is predicted by the ANSYS model as well. Furthermore, when the cube is totally unloaded, the temperature always drops back down to exactly the base level of 300 K, as it should. The ANSYS simulation behaves exactly as expected.

3.3.4 Out-of-phase three-dimensional loading cube simulation

In the third trial, the cube is subjected to three dimensional stress, but the stresses are not all in phase with each other. As before, the stresses are applied to full sides of the cube and the opposite sides are always fixed. This creates a spatially consistent state of stress throughout the cube. Figure 16 shows the applied stresses over time.

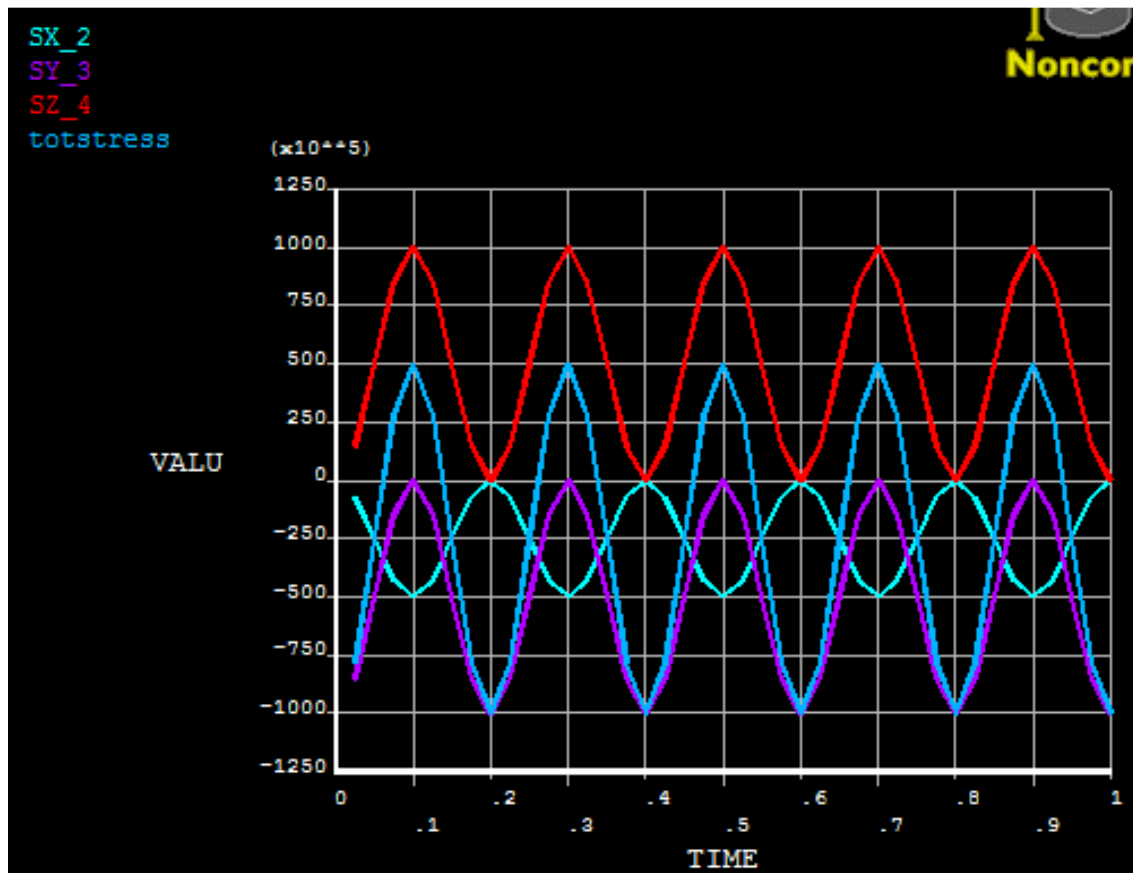


Figure 16: Third cube trial applied stresses

It can be seen from Figure 16 that all of the applied stresses oscillate from zero to their maximum value at 5 Hz. In this case, however, the x and z stresses start at zero, but the y stress is at a maximum value at $t=0$, so the y-stress is out of phase 180° with the other two stresses. The combination of these stresses over time causes a total stress that oscillates from 50 MPa in

tension to 100 MPa in compression at 5 Hz. The three-dimensional state of stress gives rise to the expected strains in each of the primary directions which can be seen in Figure 17.

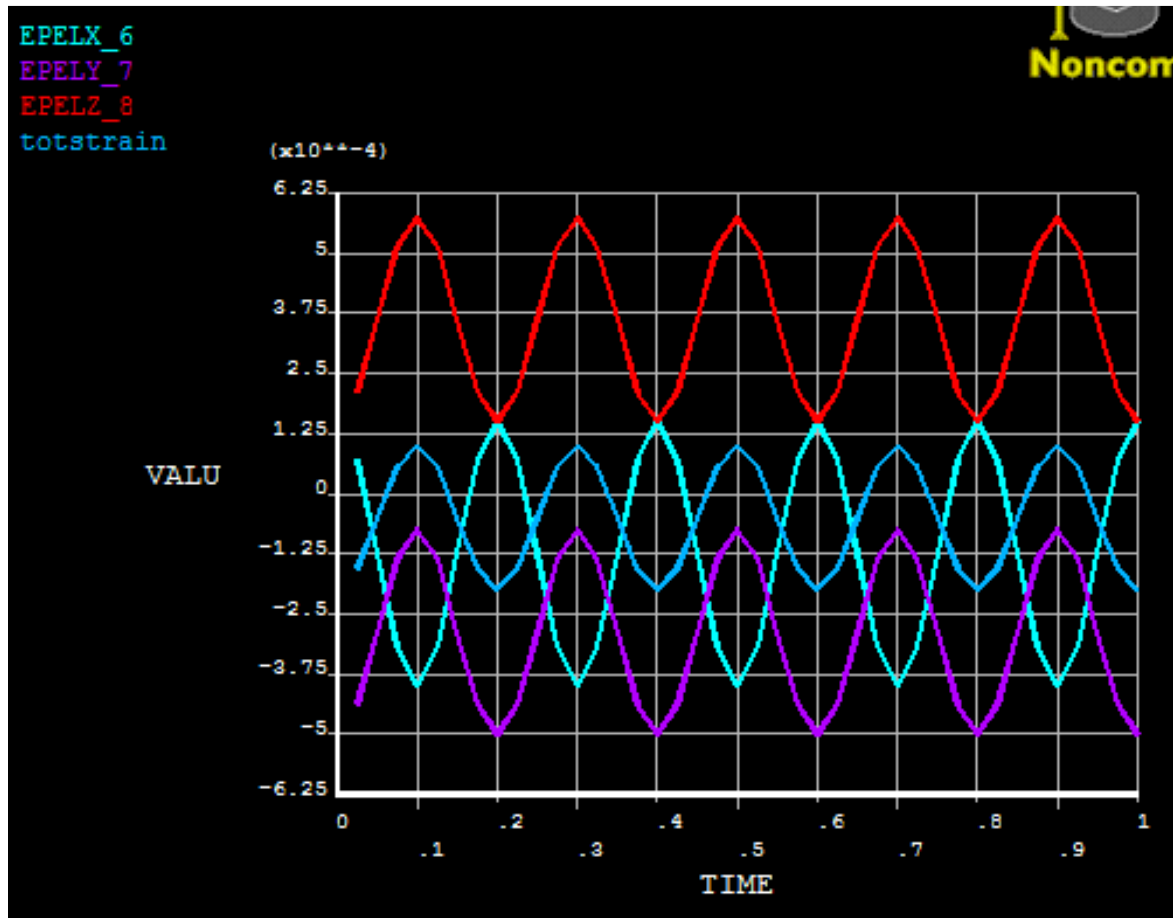


Figure 17: Strains in the third cube trial with out of phase stresses

Based on Equation 4 we know that the temperature should oscillate from 299.949K to 300.102K. This is exactly what the ANSYS model produces, as can be seen in Figure 18.

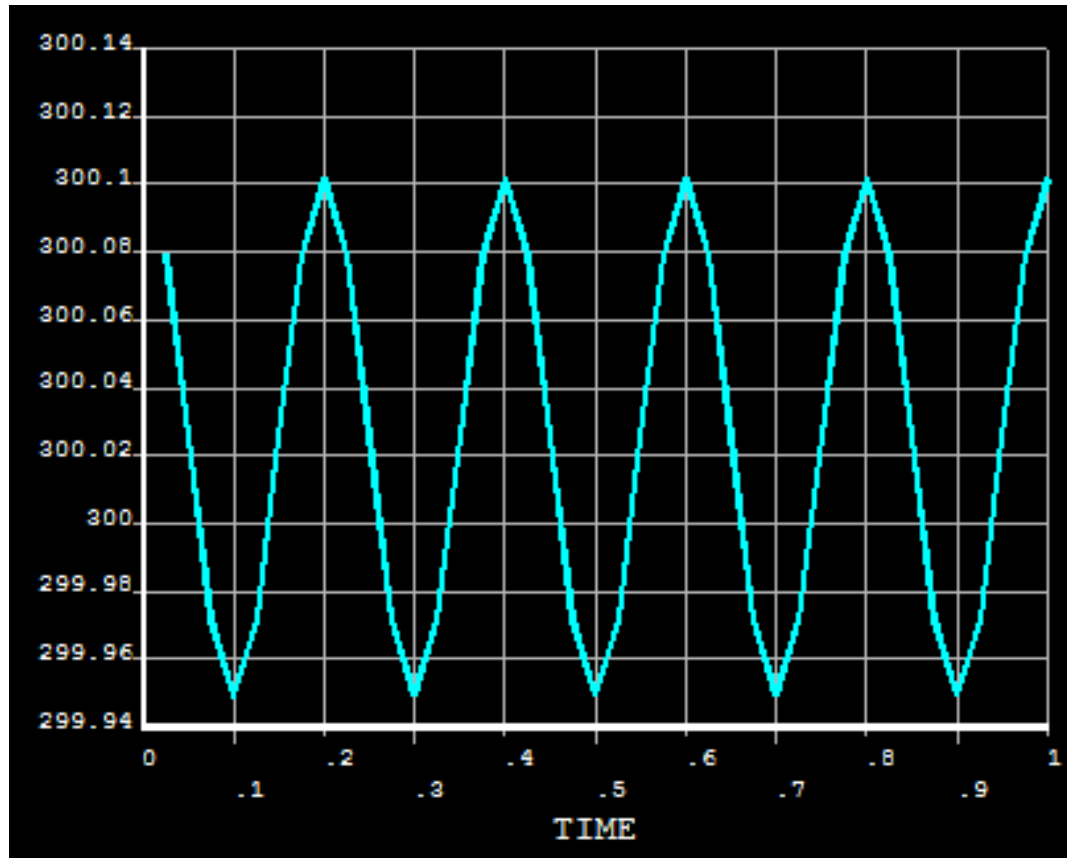


Figure 18: Temperature versus time graph for the out of phase stresses on the cube model

3.3.5 Non-uniform fixed load cube example

One more test on the cube sheds some light onto non-spatially uniform stresses. For this test, stresses are applied as seen in Figure 19. The proper fixities are applied so that the cube does not move or twist. For this test, a load step file was set up that increases these stresses from zero to their respective maximum values over the time interval from zero to one second. Then, the stresses remain at the values indicated in Figure 19 until the termination of the test at ten seconds.

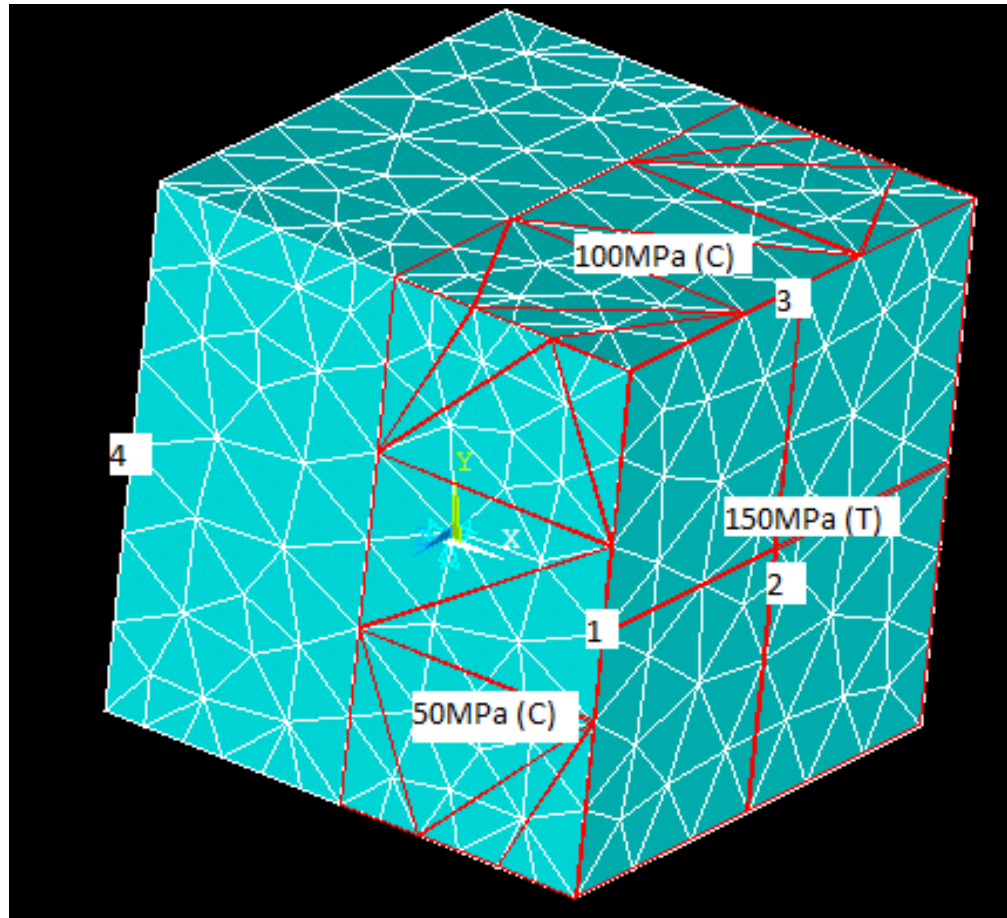


Figure 19: Loading diagram for the final cube trial

Based on this loading, there is an expected residual temperature change. The net pressure on the whole cube is equivalent to 75 MPa tension on one whole side. Therefore, from Equation 4, we expect that the temperature around the whole cube should go to 299.924 K. The following panel, Figure 20, shows the temperature versus time plots for the four points labeled on the cube in Figure 19.

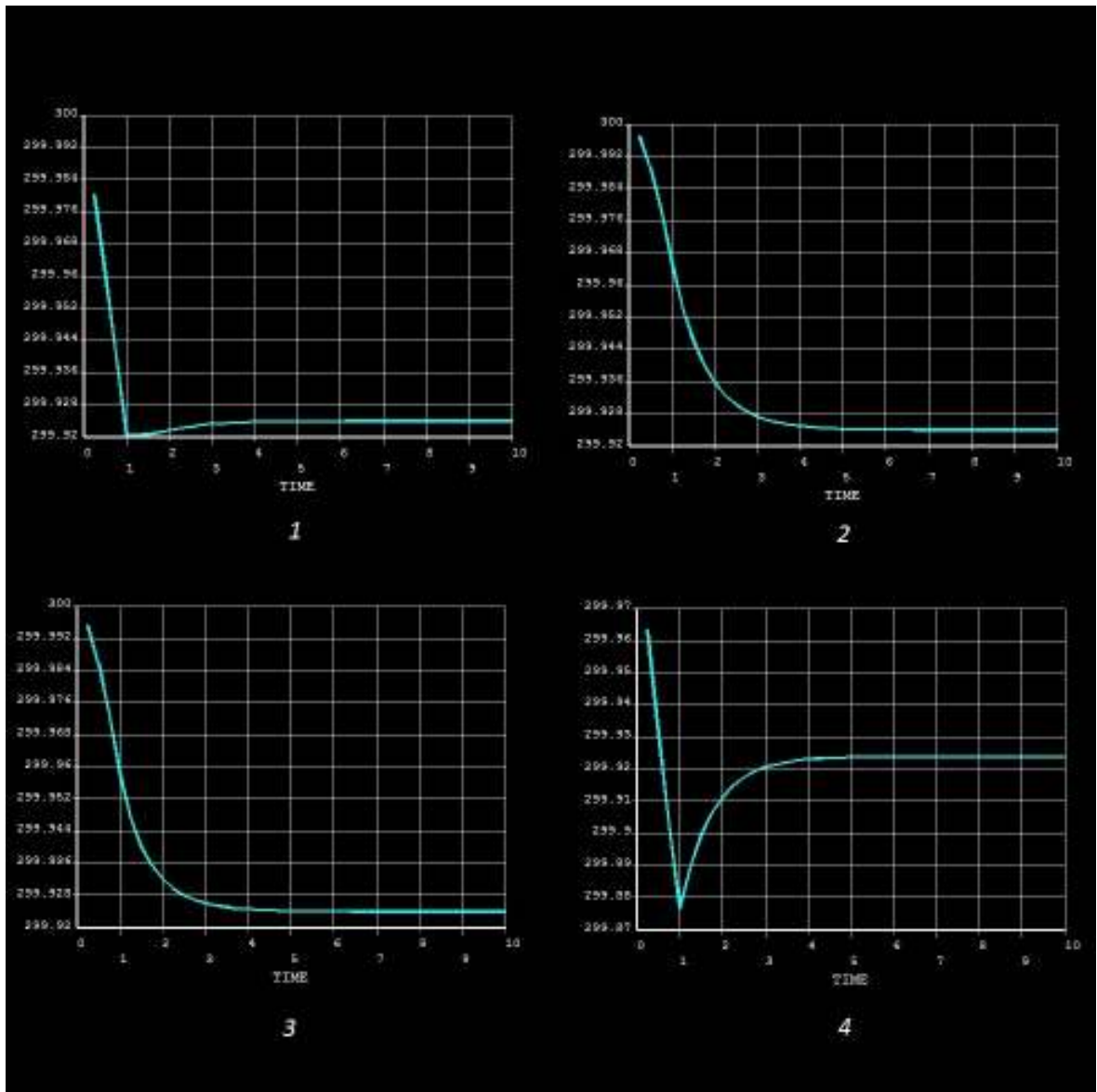


Figure 20: Temperature versus time plots for the four points on the cube indicated in Figure 19

In the first second (while the stresses are increasing linearly) all of the points experience decreasing temperature due to the overall state of stress which is tensile. Point 4 experiences the fastest and most drastic temperature drop in the first second due to the fact that it is away from the compressive forces acting on the other side of the cube. After the first second, the temperature of each point goes asymptotically towards an equilibrium value. After about eight seconds the equilibrium value, 299.924 K, is reached. This is exactly the value which is predicted

with the hand calculation. Once again it can be seen that the simulation acts exactly as predicted by the theory. In addition to these findings, some insight is gained as to how quickly the cube reaches equilibrium. For this example, where the maximum difference in temperature throughout the cube is about 0.1 °C, the temperatures move about two-thirds of the way towards the equilibrium value in the first second. After about 2.5 seconds the temperatures have moved about 95% of the way towards the equilibrium temperature. Within about seven seconds the equilibrium value is achieved.

3.3.6 Conclusions from cube simulations

Several short tests were done with stepping loading functions, to see the thermal response when a load was instantaneously removed. In this case, the temperature curve followed the step exactly, because there is no environmental loss in the ANSYS model. This is also due to the fact that the entire cube is under the same state of stress so there is no thermal flux throughout the cube. This is how the model is expected to act in the absence of environmental effects.

It can be concluded that using element 226 to try to predict thermal effects due to stress is a very accurate method in theory. In each of the examples, the ANSYS model agrees exactly with what is predicted by basic stress strain equations and basic thermoelastic theory. However, finite element models are limited in their ability to replicate actual behavior because of imperfect simulation of boundary conditions, imperfections in actual material, and a variety of environmental factors which cannot be accounted for in a basic model. Despite all of these downfalls however, it has been shown that ANSYS models thermoelastic stress effects very well.

4. Hole-In-Plate

In order to provide a link between the theory and simulations and the applications in the field, a steel specimen was tested in the laboratory. Four specimens were used for redundancy. The specimens are steel plates. Each one is 12" long, 2" wide, and 1/8" thick, with a 1/2" diameter hole in the middle. This section presents the theory, simulations, and laboratory analysis of the hole-in-plate model with applications for TSA.

4.1 Hole-in-Plate Theory

One of the classic texts in elasticity theory is Timoshenko and Goodier's *Theory of Elasticity* (Timoshenko & Goodier, 1951). This text has a nice derivation of the formulas which govern the stresses around a hole in an infinite plate under pure one-dimensional tension. After establishing parameters, plugging into the compatibility equation, and solving the differential equation, the integration constants can be determined by setting d/H to zero (where d is the diameter of the hole and H is the width of the plate), which means that this result is relevant only for an infinite plate. Equation 15, in polar coordinates, show the stresses around a hole in an infinite plate which is under uniaxial tension of magnitude σ .

$$\begin{aligned}\sigma_r &= \frac{1}{2}\sigma\left(1 - \frac{a^2}{r^2}\right) + \frac{1}{2}\sigma\left(1 - \frac{4a^2}{r^2} + \frac{3a^4}{r^4}\right)\cos(2\theta) \\ \sigma_\theta &= \frac{1}{2}\sigma\left(1 + \frac{a^2}{r^2}\right) - \frac{1}{2}\sigma\left(1 + \frac{3a^4}{r^4}\right)\cos(2\theta) \\ \tau_{r\theta} &= -\frac{1}{2}\sigma\left(1 + \frac{2a^2}{r^2} - \frac{3a^4}{r^4}\right)\sin(2\theta)\end{aligned}$$

Equation 15

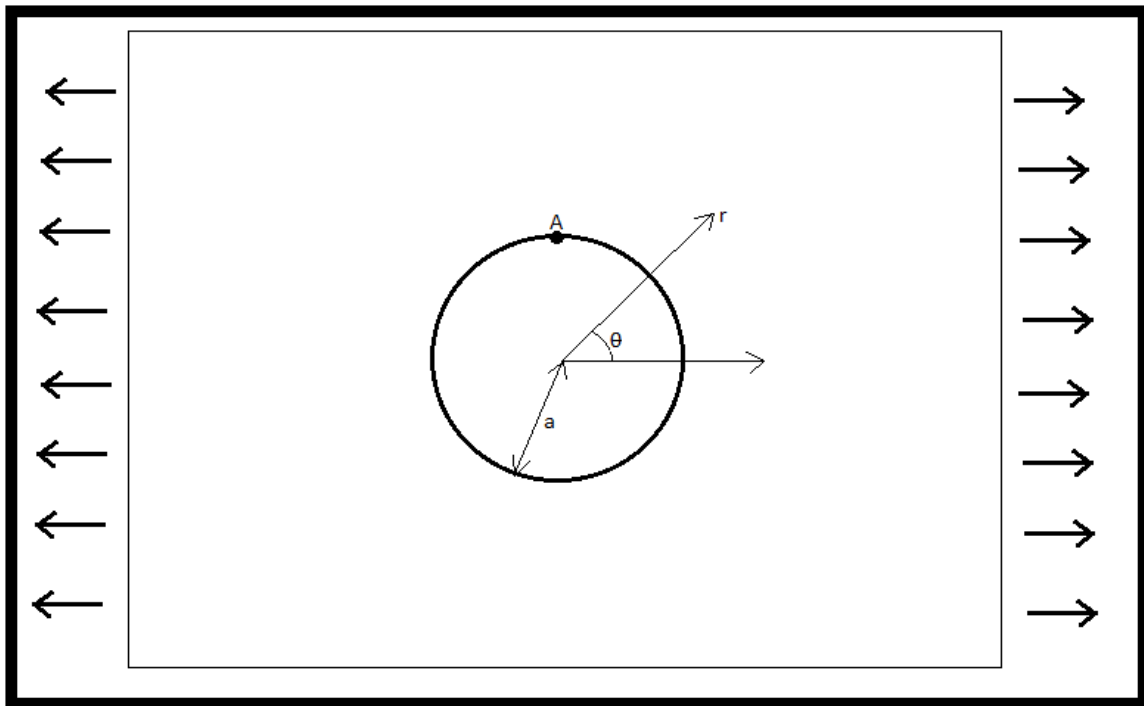


Figure 21: Diagram for infinite plate with a hole

From Equation 15, we can set $a=r$ to find the stresses on the edge of the hole. We find that the stresses in the radial direction and shear stresses are zero, while the stresses in the angular direction are given by $\sigma_\theta = \sigma(1 - 2\cos(2\theta))$. This has a maximum value of 3σ when $\theta=\pi/2$ (i.e. at point "A" on Figure 21). Of course everything is symmetric about the horizontal axis, so the stress is also 3σ at $3\pi/2$. This is the maximum stress value anywhere around the circle, so this value is the stress concentration factor, K_{tg} . This stress concentration factor uses the

stress far away from the hole as a reference, i.e. σ . This factor takes loss of cross-sectional area into account, but because this is an infinitely wide plate, the loss of cross-sectional area is irrelevant. A related stress concentration factor, K_{tn} does not take loss of section into account, so it is equal to $K_{tg} \cdot (1-d/H)$. This factor compares the max stress to the nominal stress across the hole (Pilkey, 1997).

When a finite width is considered, this has an effect on the stress concentration factor. Multiple formulas have been proposed which take into account various ranges of d/H and their effect on the stress concentration factor. Figure 22 shows a plot for both K_{tg} and K_{tn} based on formulas from Howland (Pilkey, 1997). The plates used in this experiment have a 0.5" diameter hole and a 2" width. Plugging these values into the equation for K_{tg} on the graph, we find a stress concentration factor of 3.24, which is almost 10% larger than the infinite plate value. Another formula (Equation 16), which was proposed by Heywood gives a value of 3.23 for $d/H=0.25$ (Pilkey, 1997).

$$K_{tg} = \frac{2 + (1 - \frac{d}{H})^3}{1 - \frac{d}{H}}$$

Equation 16

Copyrighted Materials

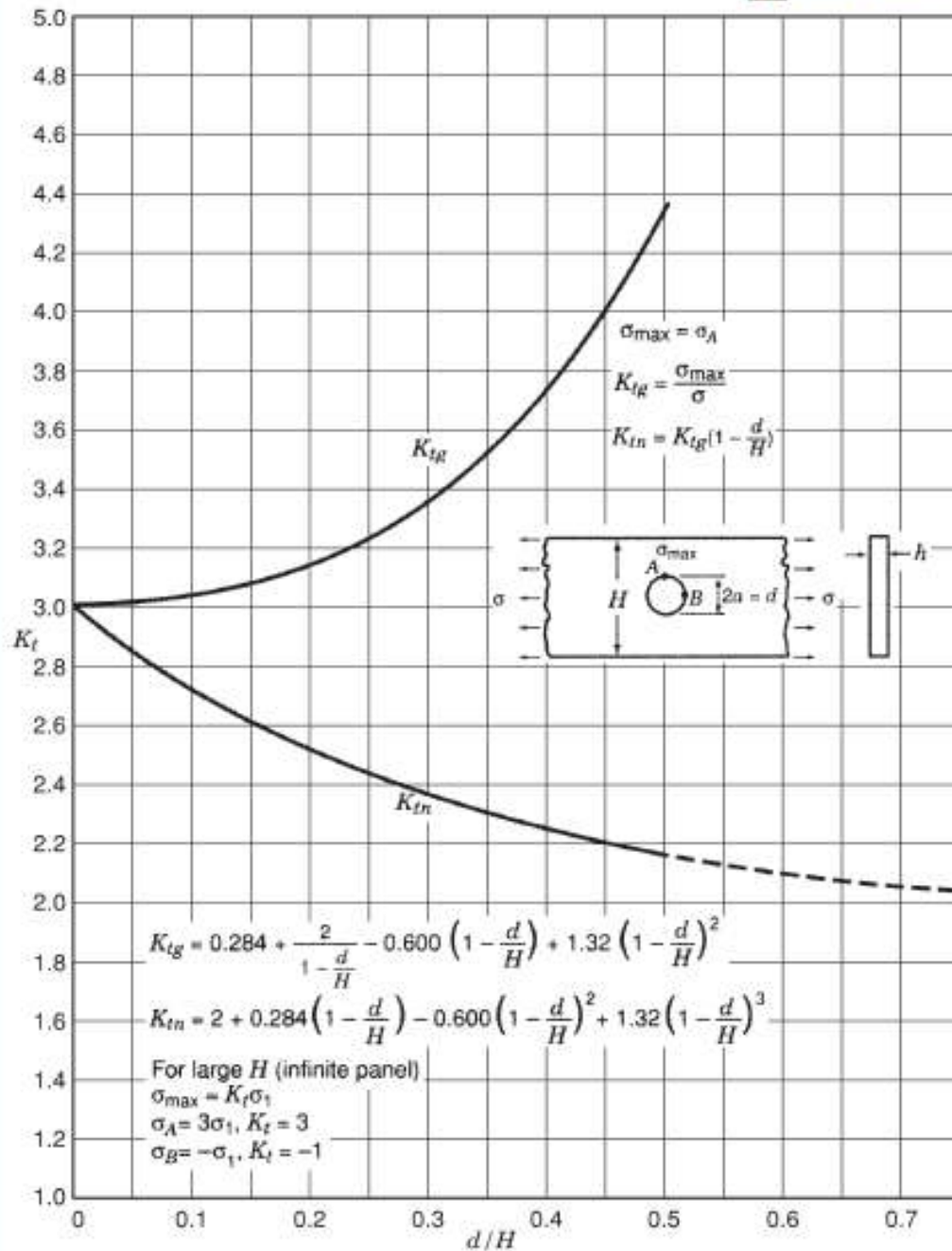
Copyright © 1997 John Wiley & Sons Retrieved from www.knovel.com

256

HOLES



LIVE GRAPH

Figure 22: Effect of d/H on stress concentration factor. Borrowed from Pilkey (1997)

From the theory, we can expect the maximum stress to be about 3.23 times the nominally applied value on the outer edges of the hole. Simulations were run in an attempt to confirm this, and will be discussed in section 4.2.

4.2 ANSYS Simulations

An ANSYS model was created to compare stress levels with theoretical computations, as well as to establish expected temperature ranges for the laboratory testing. The .lgw file for the ANSYS model can be seen in Appendix D. The model is set up with a transient solution running eight times for every loading cycle. The 12" long specimen is loaded under load control from a gross stress of 0 to 10 ksi at 3 Hz. The model is meshed tighter near the hole in order to get more accurate results.

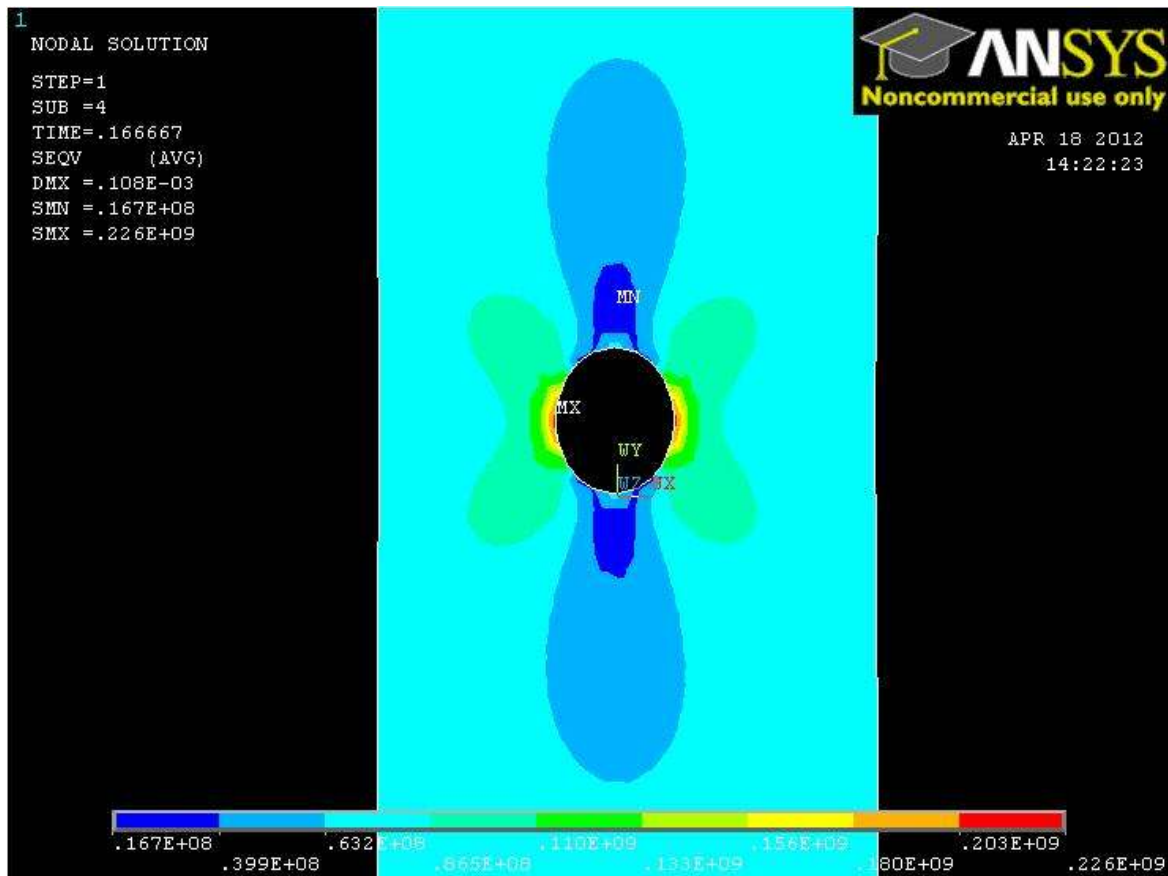


Figure 23: Von Mises stresses in the hole-in-plate ANSYS simulation

Figure 23 shows the Von Mises stresses obtained in the ANSYS simulation. Von Mises stresses are given by Equation 17. The Von Mises stresses are a good indicator of when a material will yield, so these results can be used as a guideline for the laboratory experiment. The maximum value of the Von Mises stress occurs at the lateral sides of the hole as expected, and reach a magnitude of about 226 MPa (32.8 ksi). Figure 24 shows the principal stresses from the ANSYS simulations at the point of maximum stress (i.e. point “A” from Figure 21) versus time.

$$\sqrt{\frac{(\sigma_x - \sigma_y)^2 + (\sigma_y - \sigma_z)^2 + (\sigma_z - \sigma_x)^2 + 6(\sigma_{xy}^2 + \sigma_{yz}^2 + \sigma_{zx}^2)}{2}} \quad \text{Equation 17}$$

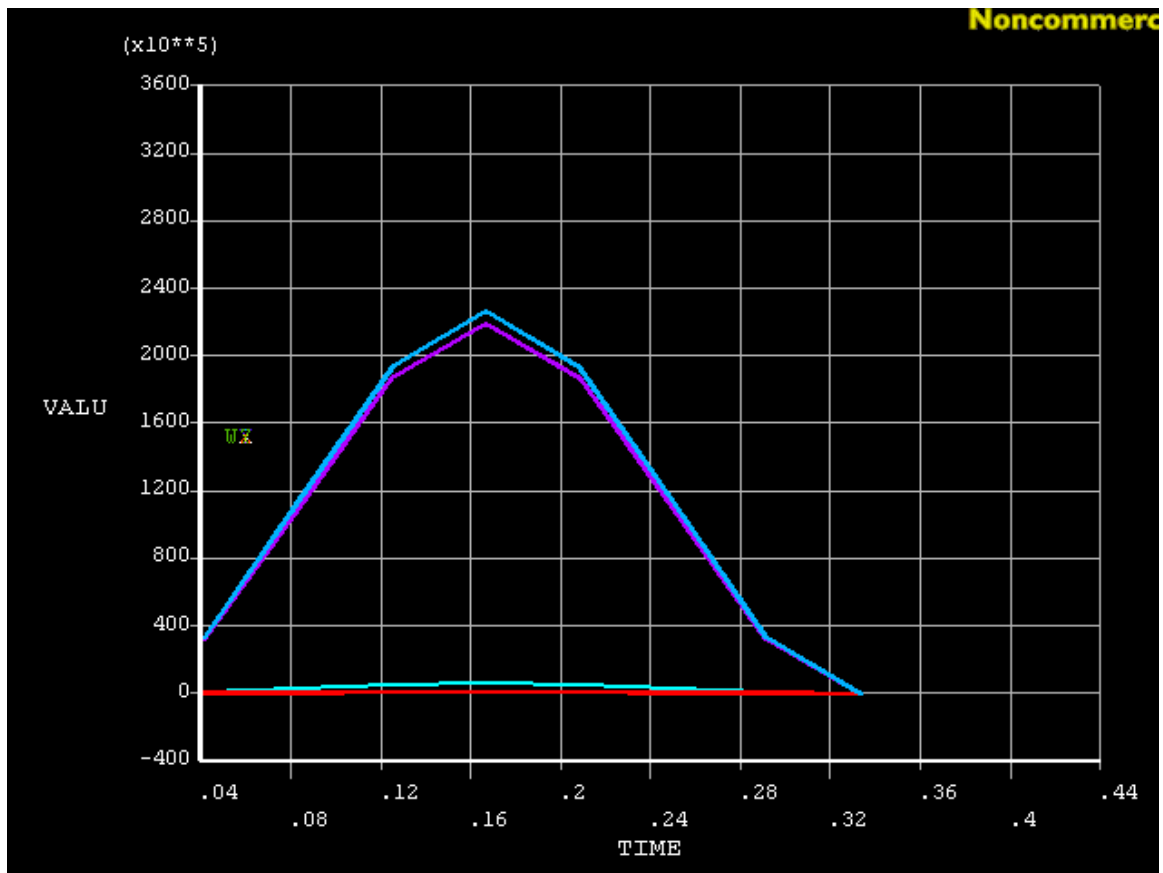


Figure 24: Principal stresses at point "A" of ANSYS simulation. Turquoise is total (the largest amplitude), purple is principal stress in y, light blue is principal stress in x, red is principal stress in z

Having the sum of the principal stresses is useful, because the temperature change is proportional to the change in volume which is proportional to the sum of the principal stresses. Almost all of the total stress comes from the y component of stress, which is intuitive because that is the direction the specimen is being pulled in. The total stress here is about 223 MPa (32.3 ksi).

Recall that the gross stress in the specimen is 10 ksi. This means that the gross stress concentration factor for this simulation is $32.3 \text{ ksi} / 10 \text{ ksi} = 3.23$. This is exactly what is expected

from the theoretical and empirical formulas discussed in section 4.1. Figure 25 shows the temperature results from the ANSYS simulation.

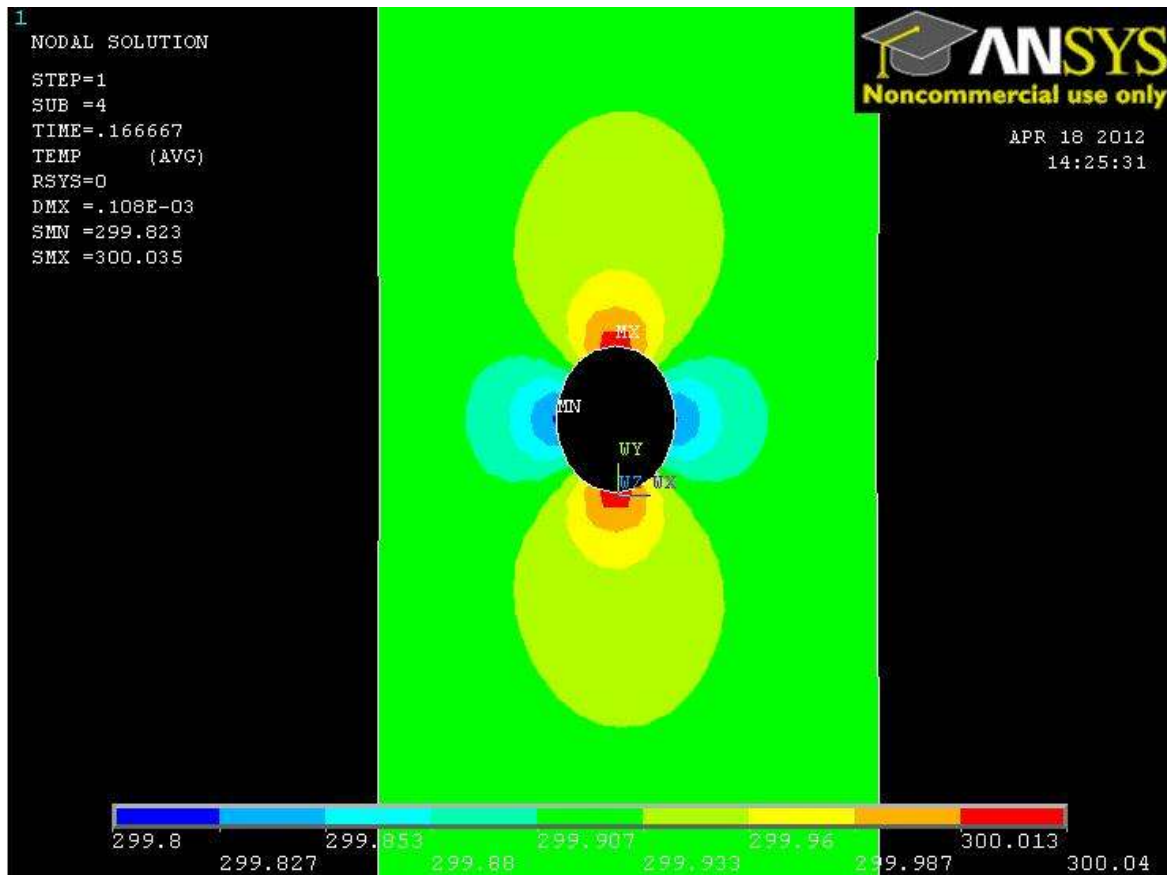


Figure 25: Temperature results from ANSYS hole-in-plate simulation

When the applied stress is near zero there will be no temperature change (300 K in this simulation). This image is taken at the maximum loading, and shows that the temperature change at point "A" is -0.173°C and it is 0.040°C at the top and bottom of the hole. Although these are small ranges, they are within the sensitivity of microbolometer detectors. Because this is in the elastic range, any displacement or stress loading can be scaled down linearly in order to achieve the desired stresses and temperature ranges. Note that this image appears to be the

inverse of the stress image because of convention. We consider tension to be positive, but a large tensile stress causes a decrease in temperature. Therefore the areas with high tensile stress in the stress images are red, and those same areas are blue in temperature images because that high stress leads to a decreased temperature.

4.3 Matlab Simulations

4.3.1 Sinusoidal reference signal

The stress levels that will be seen in the laboratory will produce temperature changes that are barely visible with the IR camera. In order to test the feasibility of using a relatively inexpensive microbolometer camera, Matlab simulations were run which include a variable level of noise. The first set of simulations simulate the test which is performed in the laboratory with a sinusoidal loading. Lock-in thermography is used to pull out the signal which is buried in noise, as it is in the laboratory and field. The Matlab files which produce these simulations can be seen in Appendix E.

The Matlab function `IRCamera` simulates the results that would be achieved using a microbolometer camera. Based on a theoretical temperature, it outputs a temperature in an unsigned 16-bit integer format (just as the camera does). It automatically adds noise using a random number generator (See Figure 26).

The function `TES` calculates the thermoelastic temperature change for an infinite thin plate subjected to uniaxial tension. The program converts Cartesian into polar coordinates, then

finds the stresses around the hole based on Equation 15. It does not include shear stresses because shear stresses do not contribute to thermoelastic effects (shear stresses do not affect the volume). Finally it calculates the temperature changes based the sum of the principal stresses.

The SimulateDataEdit file calls on IRCamera and TES to create images which are representative of what can be attained with a microbolometer camera. This file also processes the images, so that a final image which can be used to determine areas of high stress can be achieved. The image processing uses a virtual lock-in amplifier which multiplies the images, pixel by pixel, by a reference signal. Then the signal that comes out is goes through a virtual low-pass filter to get out even more noise. An averaged image is then obtained from this output, which is very clear, and become better as the record time is increased (See Figure 27).

This simulation shows that the lock-in algorithm is capable of pulling a signal out of a very noisy environment, but applying this technology in the field or the lab has many more complications than a simulation. Section 4.3.2 discusses the results of a more field-oriented simulation, and section 4.4 covers the laboratory testing, and emphasizes further complications when the noise is due to actual phenomena, and not simply a random number generator.

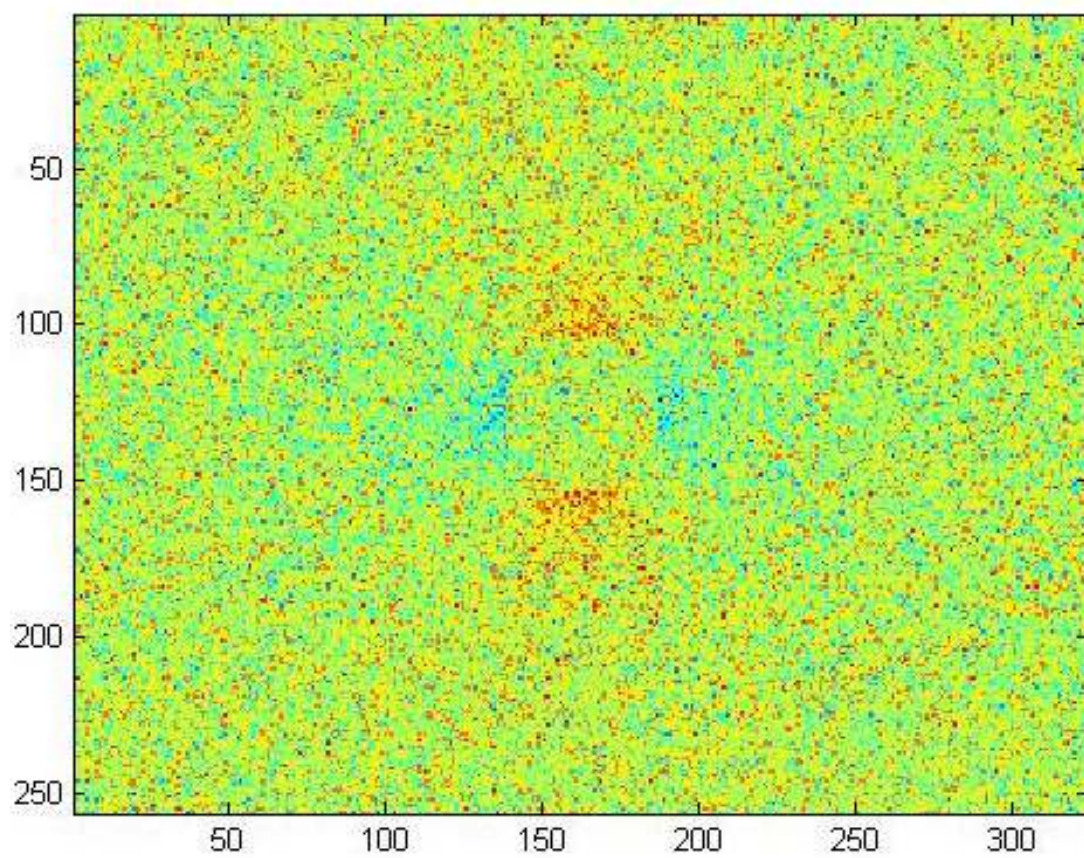


Figure 26: Unfiltered image from Matlab camera simulation. This image is taken at the maximum applied stress

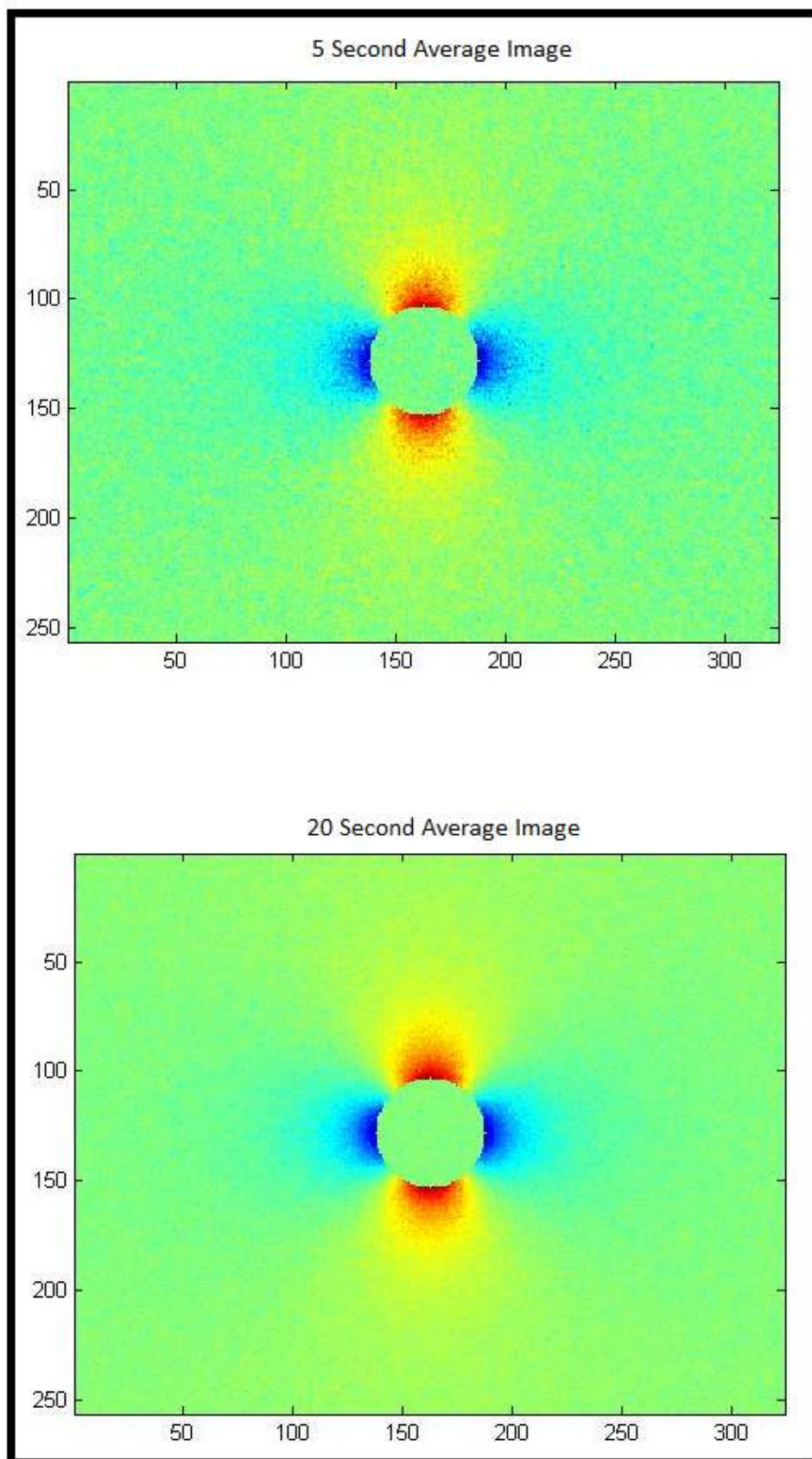


Figure 27: Images from Matlab simulation which have been filtered and averaged with the SimulateDataEdit file. Data acquired for 5 and 20 seconds respectively

4.3.2 Truck Event Simulations

Another simulation was done in Matlab that simulates loading that is typical of a truck passage over a bridge. This simulation uses the previously mentioned TES and IRCamera files, so the goal of the processing is to come up with an image that looks like the stresses around a hole in a plate in uniaxial tension (i.e. Figure 27, 20 second average). The simulated loading in Figure 9 is used as the basis for this simulation. Changes in temperature occur due to changes in the sum of the principal stresses. The actual loading signal that causes changes in temperature in this simulation can be seen in Figure 28.

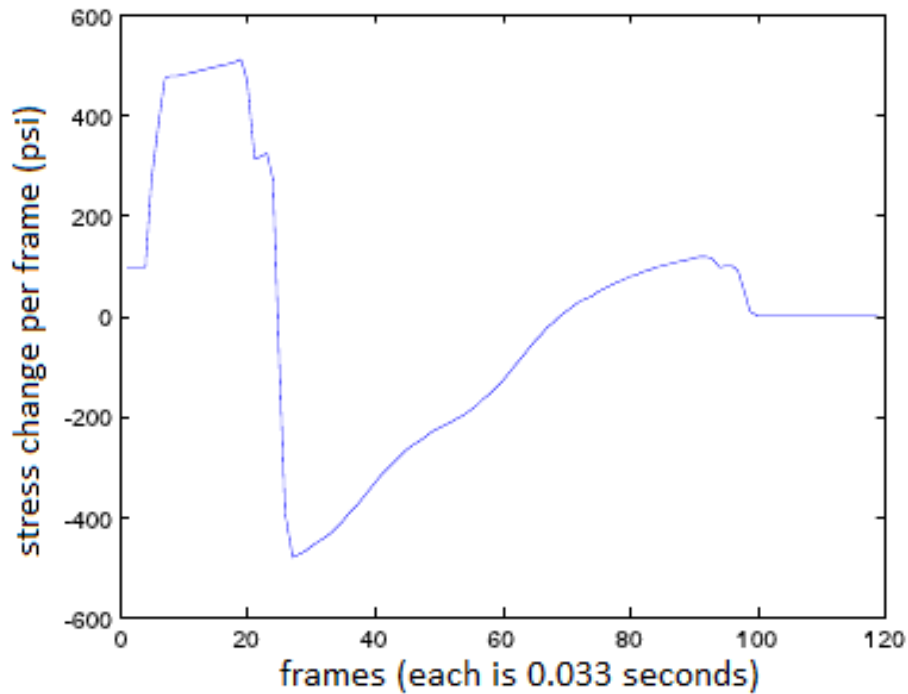


Figure 28: Change in principal stresses in truck simulation, used as loading signal for truck simulation

This reference signal can be used without additional processing because its mean is already at zero. The Matlab file that runs this simulation can be seen in Appendix F. One result, which shows the final image pulled out of ten aggregated truck simulations (all exactly the same), can be seen in Figure 29. This signal is not as strong as one with a pure sinusoidal reference, but after only five truck events, it is visible. In the field, we expect this to be even more difficult to obtain, but many more truck events can be used in the averaging. Based on this simulation, it appears as though it should be possible to perform TSA with a microbolometer on a slowly-varying specimen, such as a bridge.

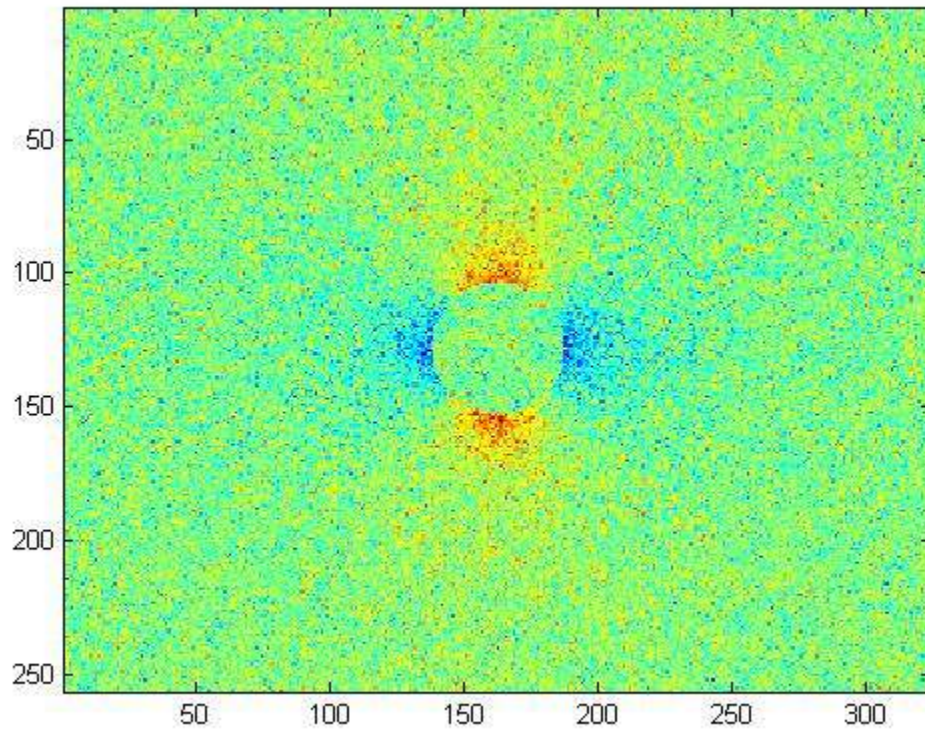


Figure 29: Final image from 5 simulated truck events

4.4 Laboratory Tests

4.4.1 Testing Setup

Laboratory tests on the hole-in-plate specimens were done on March 21, 2012. Two specimens were used, numbered #1 and #2. The specimens are each 12" long by 2" wide by 1/8" thick. Directly in the middle of each specimen is a 1/2" diameter hole. The front of each specimen

was coated with flat black paint (Krylon 1602Ultra Flat Black) around the hole (see Figure 30). These specimens are SteelWorks flat weldable steel. Steel with these characteristics are usual ASTM A569 steel. This is a commercial quality steel with a yield strength between 30 ksi and 50 ksi. Yield strength testing of unaltered specimens of this same steel showed yield strengths between 38 ksi and 42 ksi.



Figure 30: One test specimen ready to be tested

A microbolometer camera with specifications very similar to the FLIR A325 camera was used for this testing (see Figure 31). This camera does not have all of the features of the A325,

such as mechanical zoom, onboard data processing, and 60 Hz capability. These shortcomings are not a problem for this testing because the camera stays in one place (24 inches from the specimen), the data is all post-processed, and the 30 Hz capability of this camera is sufficient. The analog signal from the camera runs straight into a monitor for real-time viewing. The digital output runs into a custom-built computer by Fuchs Consulting Inc. which saves the digital files and can do some processing. The digital images are 256 by 324 pixels and have a 14 bit depth.



Figure 31: Microbolometer imager used in laboratory testing

The reference signal was obtained directly from the load signal on the MTS-810 machine, using a National Instruments data acquisition center and Labview signal processing software on a notebook computer. A schematic for the testing setup can be seen in Figure 32.

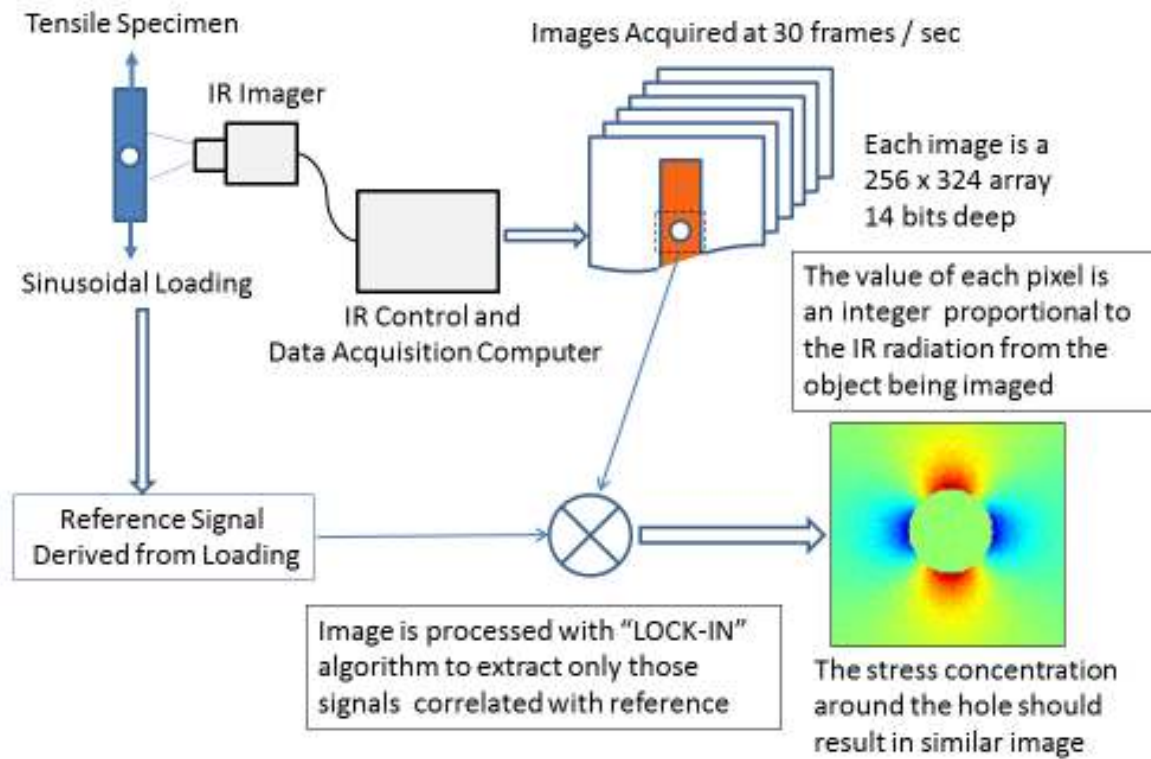


Figure 32: Testing schematic

4.4.2 Testing Procedure

After all of the components (microbolometer detector, MTS machine, imaging computer, data acquisition center and laptop) were set up, testing could begin. Because this was simply a proof-of-concept test, no triggering processes were developed to record IR camera data simultaneously with reference signal data. The record button on the camera's acquisition software was simply pressed at the same time as the record button for the MTS output in

Labview. The frequencies which the device was tested at (3 Hz and 10 Hz) are fast enough that this crude synchronizing is not sufficient to match up the reference signal with the image output signal. Applying an appropriate phase shift, largely by trial and error, will be discussed later in the paper in sections 4.4.3.2 and 4.4.3.3.

In between tests the MTS machine continued to load the specimen. This is acceptable because the loading was in the elastic range, so no permanent deformation took place. Some higher magnitude testing was done (which could have gone above the yield strength), but always after the lower magnitude tests which were known to be in the elastic range. These higher amplitude tests gave peak stresses of around 50 ksi at the edges of the hole. This amount of stress is on the upper limits of the yield capacity of the steel used in the experiment.

The specimens were all loaded under load-control. The gross cross sectional area of each specimen is 0.25 in^2 . Therefore, the gross stress in the specimen is four times the applied load. We know that the stress concentration factor around the outer sides of the hole should be 3.23, so the max stress that was anticipated from each loading is $4 \times 3.23 = 12.92$ times the applied load (e.g. when a 3.8 kip max load is applied from the MTS machine, a 49.1 ksi maximum stress should be expected on the outer edges of the hole). The analog signal which comes out of the MTS machine is a voltage signal with a range of $\pm 10 \text{ V}$. This signal is based on a cartridge which is inserted into the machine. For example, for a load cartridge that is $\pm 4 \text{ kips}$, an output of 3V would correspond to a load of 1.2 kips (calculation: $(3\text{V}/10\text{V}) \times 4 \text{ kips}$).

The microbolometer detector was preset to record for specified durations, normally 60 seconds. Once the data was recorded it was saved as an avi video file. This was then converted into frame by frame mim images (an image format that is produced by the FCI computer). Therefore, at a rate of 30 Hz, each 60 second file was stored as 1800 mim files which can be read into Matlab for processing. One of these images, cropped around the hole, can be seen in Figure

33. It is clear from this image that some advanced signal processing techniques are needed to acquire a useful image. The output from the MTS machine was recorded with a Labview Signal Express routine. The voltage levels were recorded at a sampling rate of 100 Hz. The recording had to be manually started and stopped. Once stopped, the routine automatically saved a Labview data file with unfiltered data, as well as another file with data that was processed through a low-pass filter to filter out noise. It was found that the unfiltered data was clean enough that the filtered data was never used.

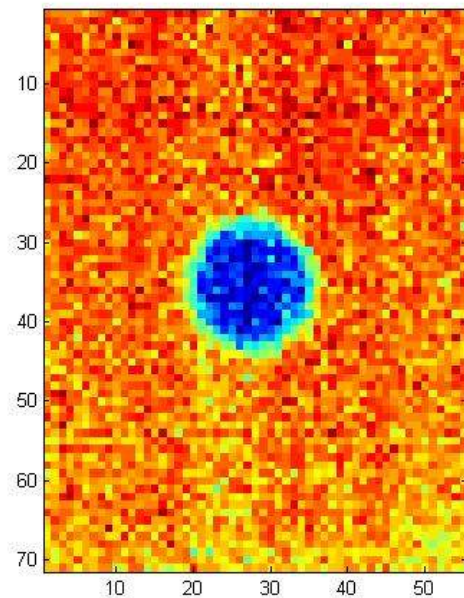


Figure 33: A cropped, raw image taken from test A1. No TSA is possible without advanced filtering of these images

4.4.3 Processing Methods

4.4.3.1 Determining Loading Rate with Beats

The principle of acoustic beats was used in order to calculate the actual frequency of the MTS output. When two waves have a similar frequency and are multiplied together, the output produces “beats” which can be seen in the waveform. These beats occur due to constructive interference at wave peaks and destructive interference at low amplitudes. This phenomenon can be described by the trigonometric identity in Equation 7, where the first term on the right side represents the beating frequency. The unknown frequency of one signal can be calculated with the known signal using Equation 18, where f_1 and f_2 are the frequencies of the two signals being multiplied and f_{beat} is the frequency of the beat.

$$f_{beat} = f_1 - f_2 \quad \text{Equation 18}$$

For example, two sine waves oscillating from zero to one at frequencies of 10 Hz and 11 Hz respectively produce a beat which oscillates at 1 Hz. This can be seen in Figure 34. The actual frequency of the MTS loading machines was determined using this method. This method was applied to every MTS output file, although it was eventually determined that the frequency remained constant throughout groups of tests. This data (sampled 100 times per second) was multiplied by an idealized sine wave (also “sampled” at 100 Hz) at the frequency that was input into the MTS machine. Beats were observed, and Equation 18 was used along with some trial and error to obtain the exact, actual loading frequency. Once the actual loading frequency is known for each test it can be used for processing in Matlab. One example of processed data (load multiplied by a sine wave of the actual frequency) can be seen in Figure 35. Although there are small variations in the amplitude of the multiplied waves, it is very consistent overall. This means

that an idealized sine wave can be used as the reference signal (i.e. the MTS machine did not load the specimens at exactly the prescribed rate, but the magnitudes were consistent between waves, and the frequency never varied during any one test).

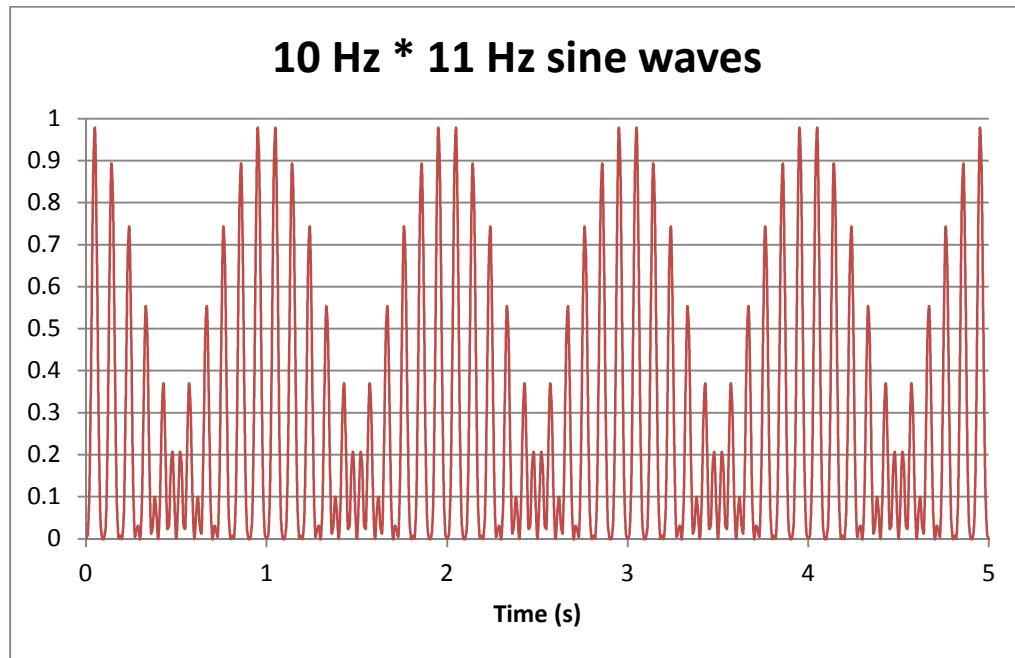


Figure 34: Beats example: Sine waves at 10 Hz and 11 Hz are multiplied together and the result produces beats which occur at 1 Hz

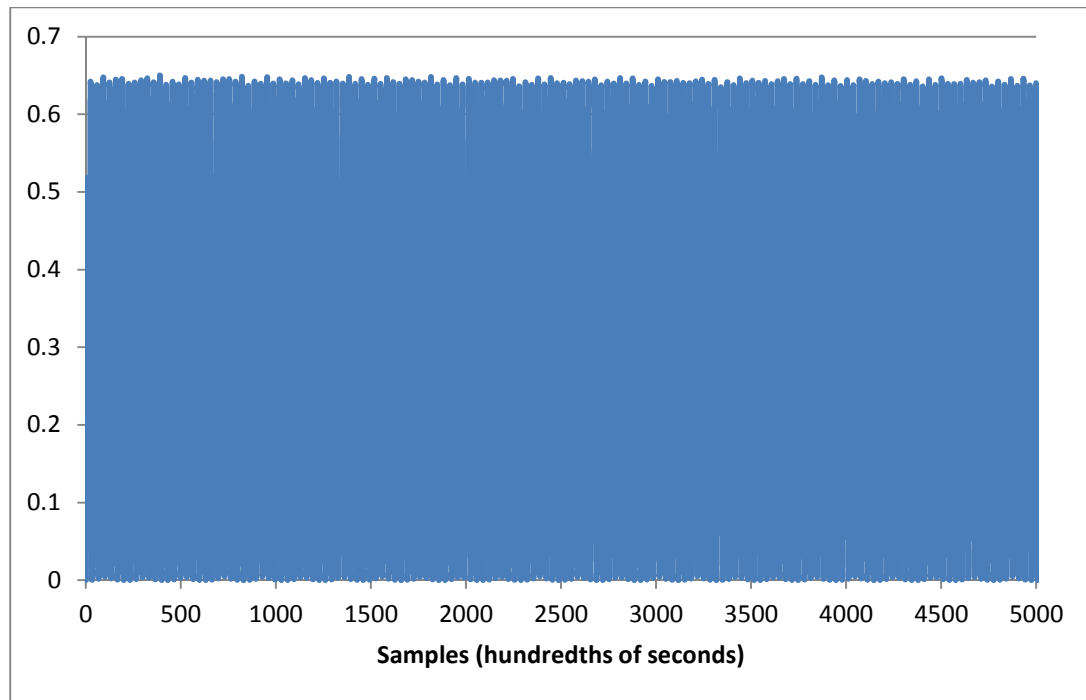


Figure 35: Sample of method used to determine actual loading frequency. This graph shows the loading signal from test C4 multiplied by a sine wave at 3.0177 Hz. The peaks are flat because 3.0177 Hz is the actual loading frequency

4.4.3.2 Idealized Sine Wave Reference Signal

Two different, but similar methods were used to provide a reference signal to the lock-in amplifier. The first method, discussed here, uses an idealized sine wave function. The loading function generated in the MTS machine was very close to an ideal sine wave. The frequency varied from set to set of tests, but always stayed consistent within any one test. Additionally, the amplitudes were always consistent, and the shape was very close to an ideal sine wave (the built in Haversine function in the MTS controller uses many small ramped segments to simulate a sine wave). For optimum lock-in response, a sine wave is generated in Matlab at the frequency of the test which is being processed. This “ideal” sine wave oscillates in magnitude from -1 to 1. This gives the best results with the lock-in amplifier.

The phase shift for the reference signal is the only unknown variable (because MTS output recording and video capture did not begin simultaneously). The brute-force method of applying varying phase-shifts and looking at the resulting images was used because there were not a lot of tests to process, and there is no better way to achieve qualitative output without a triggering mechanism. The full algorithm which reads in the image files, processes them, and produces a final, averaged image can be seen in Appendix G.

4.4.3.3 MTS Output Reference Signal

Using the MTS output as the reference signal for the lock-in process has some advantages and some disadvantages. Unfortunately the MTS machine was sampled at 100 Hz which makes it impossible to pull out 30 evenly-spaced values to multiply the images with, unless numerical methods are used to estimate most of the values. Also, the phase-shift is more limited than the idealized sine wave because it is discretized. On a positive note, however, using this as the reference signal has more applications for in-field testing, because loadings in the field will not be able to be modeled as sine waves.

The output from the MTS machine (in volts) is automatically saved to a labview measurement file. This file can be opened and edited in a variety of software packages, including Labview, Labview Signal Express, and Microsoft Excel. For this research, Excel was used to manipulate the output. Once the voltages were moved to a blank sheet with an Excel Macro, another Macro was applied to essentially decrease the sampling rate from 100 to 30 Hz. These Macros can be seen in Appendix H. The second one basically works by deleting 28 out of every 40 data points, and repeating throughout the data. Table 1 shows the data points that are retained. Even though interpolating would have yielded slightly better results, the increase in final image

quality would have been minimal. Interpolating would have also involved more manipulation of the signal which is not desired, because the goal of using this reference signal is to get as close as possible to the way processing will be done with field measurements.

Table 1: Graphic displaying deleted / retained data when reduced from 100 to 30 Hz sampling rate

1	21
2	22
3	23
4	24
5	25
6	26
7	27
8	28
9	29
10	30
11	31
12	32
13	33
14	34
15	35
16	36
17	37
18	38
19	39
20	40

grey cells are retained

white cells are deleted

process repeats every 40 cells

Once the data is reduced down to the necessary 30 Hz, it can be used as the reference signal. The issue of an unknown phase-shift presents itself here again. Ten data points in this reference signal represents a full loading cycle because the specimen is loaded at approximately 3 Hz and the data here is sampled at 30 Hz. Therefore, by changing the starting data point from the first cell to the second cell, a phase shift of approximately $\pi/5$ is attained. Starting with cells

one through ten will provide all the possible phase shifts with this discrete data. The code for a fixed phase shift can be seen in Appendix I.

Some liberties were taken with the data due to the fact that it is a sine wave. The data goes through a normalizing routine in Matlab (embedded in Appendix I) before it is used in the lock-in process. This routine shifts all of the data so that the mean is at zero. It then normalizes it to oscillate from -1 to 1 for optimum lock-in output. This normalization algorithm is crucial to the success of the lock-in amplifier, as can be seen in the comparison in Figure 36, although the only crucial step in this process is shifting to curve so that it oscillates around zero.

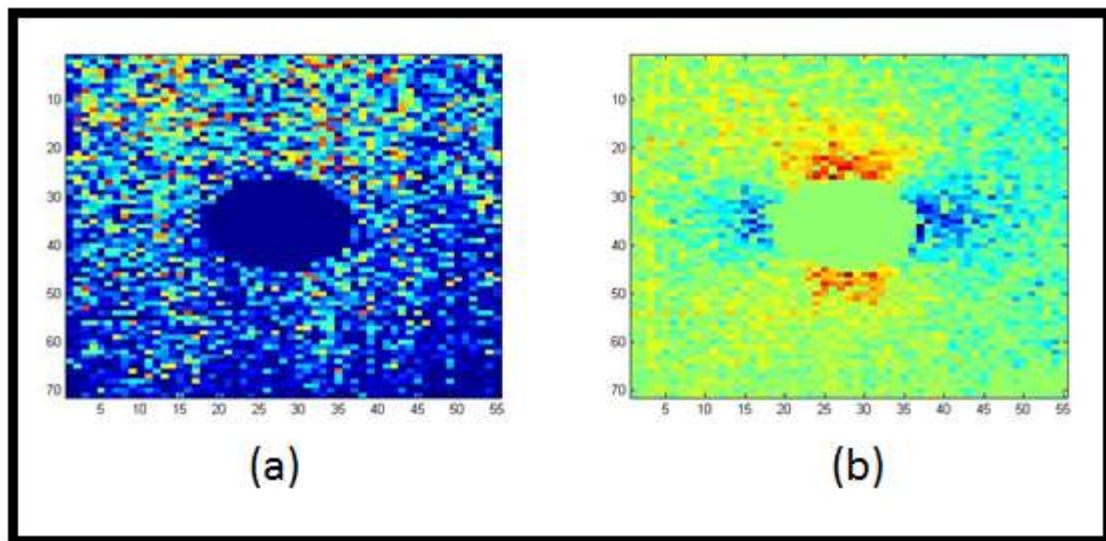


Figure 36: Comparison of results from the MTS-referenced test A1 : (a) no normalizing algorithm for reference signal
(b) normalized

4.4.4 Data and Analysis

Several tests were run on both specimen #1 and specimen #2. A table which acts as an index for all of the results can be seen below (Table 2). All of the tests were done chronologically in the order seen in Table 2.

Table 2: Index for tests and phase-shift results

						WITH IDEALIZED SINE WAVE	WITH MTS REFERENCE SIGNAL
index	specimen	load	gross stress (ksi)	duration (s)	loading freq.	optimum phase shift (*pi) *	optimum start cell**
A1	1	125- 2200#	0.5 - 8.8	60	3.0157	0.55	7
A2						1.95	8
A3						1.80	9***
A4						0.95	6
A5						1.50	3
B1		125 - 3800#	0.5 - 15.2		3.0277	1.25	8
B2						1.50	6
C1	2	125- 2200#	0.5 - 8.8		3.0157	1.50	1
C2						1.65	6
C3						0.60	1
C4						0.35	3
C5						0.10	8
D1						125 - 3800#	0.5 - 15.2
D2		1.75****	8****				

*where the phase shift (ps) is

$\sin(\text{time}(k) * \text{LoadRate} * 2 * \pi + \pi/2 + \text{ps})$

**this refers to the phase shift. Phase is shifted by starting the reference signal at a different point from the MTS output

***low-quality image because leads were touching at beginning of MTS output recording

****averaged over 180 seconds

The loading frequency values are the actual frequencies at which that the MTS machine loaded the specimens. The analog controller for the MTS machine is over 20 years old and uses a

combination of digital and analog electronics. It loads the specimens at a frequency accurate to within about 2 percent of the value entered by the user. For the “TEN” tests the entered frequency was 10.0000 Hz. For tests “A” through “D” the entered frequency was 3.0000 Hz. Because the lock-in algorithm works over a long period of time (usually 60 seconds in this testing), a difference between the assumed reference frequency and actual reference frequency of less than 1% can make a large difference. The actual loading frequencies seen in this table were found using the acoustic beats method discussed in section 4.4.3.1.

Interestingly, it was found that the frequency changed slightly when larger amplitude loadings were used, but the frequency returned to exactly the original level once the low-magnitude testing was done on the specimen #3. The frequency also returned to the same rate for specimen #3 high-amplitude tests as it was during specimen #1 high-amplitude testing.

Once the actual loading frequencies are known, true data processing can begin. The two Matlab scripts that were discussed in sections 4.4.3.2 and 4.4.3.3 were used to process data. These routines read in the image files that come directly from the microbolometer detector and put them in a large three-dimensional matrix. A mean value for a large spatial area of the image was calculated for each frame and was then subtracted from every pixel on a frame-by-frame basis. This was done because there were some variations of temperature across the entire image that varied slowly over time. These variations could be due to drafts in the room, heat coming off of the MTS machine, or the people in the laboratory. An example of how the value related to temperature for one pixel in one experiment varied over time can be seen in Figure 37.

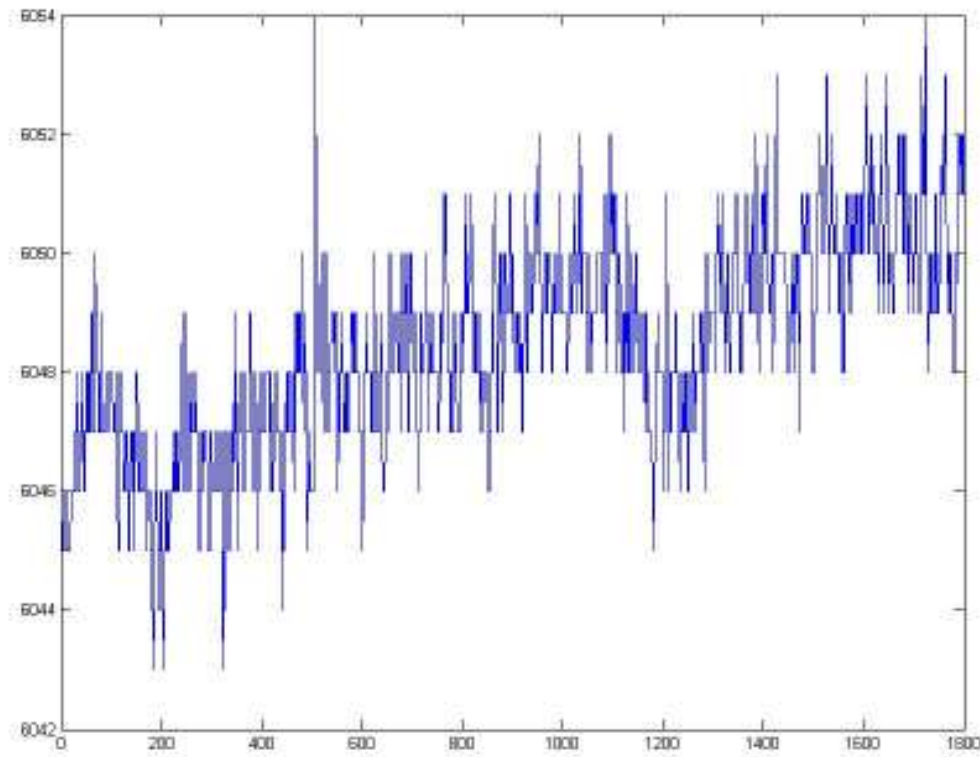


Figure 37: Camera recorded values for a pixel directly to the right of the hole (where the highest stress concentrations are) from test A1 vs. frame (30 frames per second)

After a few arithmetic operations, the images are converted from the unsigned 16-bit integer format into a double format. This requires a substantial increase in memory over the uint16 format, but it is necessary for negative values and accurate averaging. Then the lock-in algorithm is applied. Depending on the program, the reference signal is either the idealized sine wave or comes directly from the MTS output. The multiplication is applied to every pixel in the vicinity of the hole. Most of the image is cropped out for this part because the results away from the hole are uninteresting and expensive in terms of computing power. After this multiplication takes place for every pixel around the hole, the average image over time is calculated. The appropriate phase shift is found by trial and error, using the algorithm “phaseshift” (seen at the

end of Appendix G) for the idealized sine wave, and by use of a for-loop which calculates the image for every possible phase shift for the MTS-generated reference signal.

All of the final images can be seen in Appendix J for both reference signal sources. All of these images were obtained using the optimum phase shift for each test. A few conclusions can be drawn from these images. First and foremost, TSA is possible in the laboratory using a microbolometer camera. With stress ranges below yield at the edges of the circle, the images are still quite clear. Secondly, having a higher stress range does not necessarily produce a clearer image, as can be seen by comparing sets A with B and C with D. No quantitative data relating directly to the actual temperature or stresses can be directly obtained from the images, although known theoretical values could be used for calibration in future work. The images could have been clearer if the camera had been moved closer to the specimen. The interesting part of the image was only 71 by 55 pixels, a small portion of the cameras full capability.

All of the final images exhibit the same stress pattern which has a higher intensity on the right side of the hole. This was unexpected, but Figure 30 shows that perhaps it should not have been. It appears as though the specimens were not centered in the clamps during testing. This induced a moment in the specimen which caused greater stress on the right side than the left side. Using some basic beam equations (Equation 19 - moment-induced stress at a distance y from the centroid, and Equation 20 - moment of inertia of a rectangular cross-section), it is easily seen that even a small eccentricity in the loading can cause a large increase in stress on the side with the eccentricity. An eccentricity of 0.25" increases the stress at the right edge by a 75% and decreases the stress at the left edge by 75%. In this scenario, the stress to the immediate right of the hole (where max stress is expected under uniaxial stress) is increased by 19%. Correspondingly, the stress immediately to the left of the hole is decreased by 19%. Although the

actual eccentricity is unknown, it is assumed that there is some eccentricity and it causes the final images to favor the right side of the specimen.

$$\sigma = \frac{M * y}{I}$$
Equation 19

$$I = \frac{1}{12} b * h^3$$
Equation 20

Where: σ = stress (e.g. ksi)

M = moment (=P*e where P is applied force and e is eccentricity) (e.g. in-kip)

y = distance from centroid (e.g. in.)

I = moment of inertia (e.g. in.⁴)

b = base (e.g. in.)

h = height (e.g. in.)

Although temperatures, and therefore stresses, cannot be accurately obtained from these images, some quantitative data can be gathered. The values that correspond to the color of each pixel in the image have been highly processed so they have little physical meaning, but they are still related to the overall state of stress at each point (that is the whole idea of all the processing). Therefore, comparing their magnitudes can give some insight into the stress ranges. Table 3 shows the values from the pixel with the minimum and maximum value for each processed image. These values are averaged over each set and then compared to each other. As expected, both the average minimum and maximum values from each higher-level load test have greater magnitude than the corresponding lower-level load tests. Although the correlation between these values and actual stresses is muddled, these could be used to estimate stresses, especially if calibrated on a specimen with known stress.

Table 3: Quantitative analysis of final processed images

						Averages by set		high avg. / low avg.	
index	specimen	load	gross stress (ksi)	min value	max value	min	max	min	max
A1	1	125-2200#	0.5 - 8.8	-0.0094	0.0100	-0.0151	0.0118	1.391	1.385
A2				-0.0132	0.0107				
A3				-0.0188	0.0144				
A4				-0.0149	0.0104				
A5				-0.0190	0.0137				
B1		125 - 3800#	0.5 - 15.2	-0.0155	0.0116	-0.0210	0.0164		
B2				-0.0264	0.0212				
C1	2	125-2200#	0.5 - 8.8	-0.0231	0.0161	-0.0177	0.0122	1.501	1.524
C2				-0.0134	0.0088				
C3				-0.0204	0.0118				
C4				-0.0191	0.0135				
C5				-0.0126	0.0110				
D1		125 - 3800#	0.5 - 15.2	-0.0248	0.0174	-0.0266	0.0187		
D2				-0.0284	0.0199				

Several iterations of the idealized sine wave routine were run in order to see the effect of the phase shift. The same test was used, D2, and everything was held constant except for the phase shift. The resulting images can be seen in Appendix K. A few conclusions can be drawn from these images. First, any image can be “reversed” by adding π to its phase shift. This makes sense, because a phase shift of π keeps the same magnitudes but reverses the sign of its values. Secondly, there is a wide range of phase shifts that create an acceptable image. Although only one of them is “correct” (i.e. synchronized with the IR camera recordings), many of the phase shifts produce usable images. For the example illustrated in Appendix K, phase shifts between 1.4π and 1.9π all produce acceptable images.

The amount of video that must be recorded in order to make a quality image will be an important consideration when applying TSA to civil infrastructure in the field. Appendix L contains several images that were all taken from test D2 at the optimal phase shift. Each image has been averaged over a different amount of time, which is labeled under the image. The results are unsurprising; the longer the averaging period, the better the image quality. A discernible image is achieved with a 5 second averaging (which is 15 cycles at 3 Hz). Increasing the averaging time from 1 to 5 seconds has a very large effect, but increasing it from 30 to 180 seconds has a small effect.

One miscellaneous result was obtained when a specimen was stretched well beyond yield. After all sinusoidal tests were completed, a test which ramped the loading at a rate of 100# per second up to a maximum value of 10 kips was run. The load curve and displacement curve can be seen in Figure 38. It appears as though the specimen begins to yield roughly 50 seconds into the test which corresponds to a load of 5 kips. This is consistent with the finding that the specimens were still behaving elastically at peak loads of 3.8 kips.

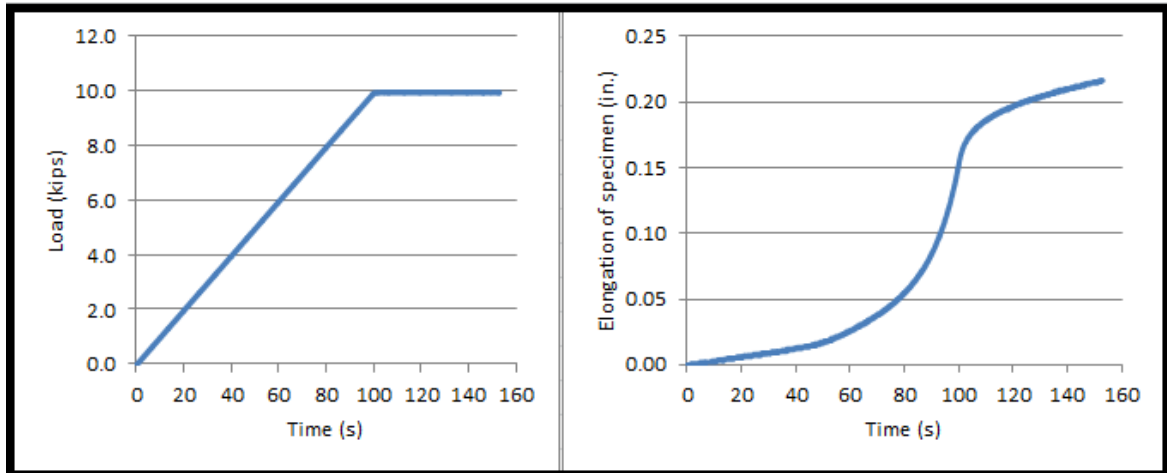


Figure 38: Load curve and elongation curve for the ramped test

At an applied load of 10 kips, the stress around the side of the hole is calculated to be about 129 ksi. This led to visible deformation of the specimen. An image taken 90 seconds into the testing, at a load of 9 kips, can be seen in Figure 39. This image is completely unprocessed. The temperature changes were so large that no processing was needed to see the stress pattern. When materials yield they release a relatively large amount of heat, which is why the areas on the outside of the hole are red where the thermoelastic images are normally blue in this region.

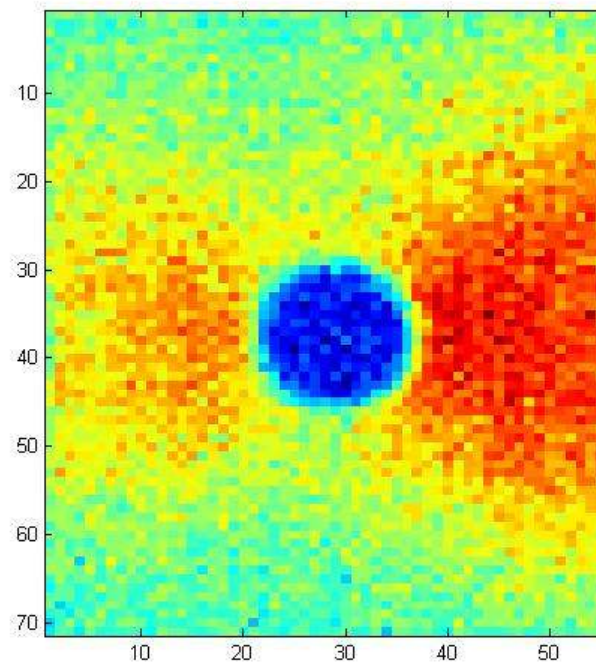


Figure 39: Unprocessed image showing temperature variations in a specimen due to plastic deformation

5. Conclusions

A few conclusions can be drawn from this research. First, thermoelastic stress analysis in the laboratory is possible with a relatively inexpensive microbolometer camera. Moderate to high stress levels are required, but the stresses do not need to be at or beyond the yield limits of structural steel. Thermoplastic stress analysis, although less understood and less applicable to steel bridges, is also possible. For laboratory sinusoidal loading, long time-averaging durations are not required. Images that are obtained from the lock-in processing are high enough quality to determine the size, shape, and location of anomalies in the surface, as well as the relative level of

stress at any point. These are all very useful things to know when dealing with spatially varying stress concentrations like in a steel bridge web gap.

It can also be concluded that ANSYS is a very valuable tool for simulating thermoelastic effects. ANSYS can be used to predict or validate tests performed in the laboratory or in the field. ANSYS can also be used to model particular bridge details and evaluate the feasibility of performing thermoelastic stress analysis.

The results from the testing performed for this report are very encouraging. This was a successful proof of concept test, and if future projects based on this one continue to go well, this will produce a very useful tool for monitoring fatigue cracks in bridges. It could also have many other applications in civil infrastructure and elsewhere.

6. Future Work

Because this is the first attempt at using TSA for civil infrastructure in the field, there is a lot of future work that can be done. This research proved that today's relatively inexpensive infrared cameras can be used to "see" stresses below yield in steel. Future projects should take this proof-of-concept and turn it into a product which can be used by state DOTs. This product will consist of a detector similar to the one used in the laboratory testing in this experiment, a computer for storing images, a device used to trigger recording and generate a reference signal (such as a strain gage), and software to process the recorded images. If this technology is successful in this application, it could have other applications as well where much more expensive cameras could be replaced with a microbolometer camera.

The next step towards the production of this final product is to perform laboratory tests with loadings that simulate truck loadings. These tests should involve a trigger that causes the camera to record when a load is detected via a strain gage. If these tests achieve desirable results, then the next step would be to use the setup on an actual bridge.

Moving forward, this research should develop a stronger TSA capability for field and laboratory testing. Other applications for nondestructive thermal evaluation should be investigated, such as crack detection under paint, coating evaluation, and void detection in post tension ducts.

7. Appendices

Appendix A Physical properties of steel

Quantity	Symbol	Value	Units
Specific Heat	Cp	490	J/kg*K
Density	P	7850	Kg/m ³
Young's Modulus	E	2.0*10 ¹¹	Pa
Poisson's Ratio	v	0.30	(unitless)
Thermal Conductivity	k	50	W/m*K
Coeff. Of Thermal Expansion	α	13*10 ⁻⁶	K ⁻¹

Appendix B Lgw file for cube simulation

```

/BATCH
/input,menust,tmp,'',,,,,,,,,,,,,,1
WPSTYLE,,,,,,,,,0
/PREP7
BLOCK,0,.01,0,.01,0,.01,
FINISH
/SOL
FINISH
/PREP7
ET,1,SOLID226,11
KEYOPT,1,1,11
KEYOPT,1,2,0
KEYOPT,1,4,0
MPREAD,'steelSIunits','mp','J:\RESEARCH ansys\'
ESIZE,,6,
MSHAPE,0,3D
MSHKEY,1
CM,_Y,VOLU
VSEL,,,,1
CM,_Y1,VOLU
CHKMSH,'VOLU'
CMSEL,S,_Y
VMESH,_Y1
CMDELE,_Y
CMDELE,_Y1
CMDELE,_Y2
FINISH
/SOL
TREF,300,

```

```

FLST,2,1,1,ORDE,1
FITEM,2,2
/GO
D,P51X, , , , , ,UX, , , , ,
FLST,2,1,1,ORDE,1
FITEM,2,2
/GO
D,P51X, , , , , ,UY,UZ, , , ,
FLST,2,1,5,ORDE,1
FITEM,2,3
/GO
DA,P51X,UY,
FLST,2,1225,1,ORDE,2
FITEM,2,1
FITEM,2,-1225
IC,P51X,TEMP,300, ,
ANTYPE,4
TRNOPT,FULL
LUMPM,0
OUTRES,ALL,ALL,
TIME,10
AUTOTS,-1
DELTIM,.025, , ,1
KBC,0
TSRES,ERASE
*DEL,_FNCNAME
*DEL,_FNCMTID
*DEL,_FNCCSYS
*SET,_FNCNAME,'cube'
*SET,_FNCCSYS,0
*DIM,%_FNCNAME%,TABLE,6,14,1,,,,,%_FNCCSYS%
*SET,%_FNCNAME%(0,0,1), 0.0, -999
*SET,%_FNCNAME%(2,0,1), 0.0
*SET,%_FNCNAME%(3,0,1), 0.0
*SET,%_FNCNAME%(4,0,1), 0.0
*SET,%_FNCNAME%(5,0,1), 0.0
*SET,%_FNCNAME%(6,0,1), 0.0
*SET,%_FNCNAME%(0,1,1), 1.0, -1, 0, 10, 0, 0, 0
*SET,%_FNCNAME%(0,2,1), 0.0, -2, 0, 3.14159265358979310, 0, 0, -1
*SET,%_FNCNAME%(0,3,1), 0, -3, 0, 1, -1, 3, -2
*SET,%_FNCNAME%(0,4,1), 0.0, -1, 0, 1, -3, 3, 1
*SET,%_FNCNAME%(0,5,1), 0.0, -2, 0, 3.14159265358979310, 0, 0, 0
*SET,%_FNCNAME%(0,6,1), 0.0, -3, 0, 2, 0, 0, -2
*SET,%_FNCNAME%(0,7,1), 0.0, -4, 0, 1, -2, 4, -3
*SET,%_FNCNAME%(0,8,1), 0.0, -2, 0, 1, -1, 2, -4
*SET,%_FNCNAME%(0,9,1), 0.0, -1, 9, 1, -2, 0, 0
*SET,%_FNCNAME%(0,10,1), 0.0, -2, 0, 50000000, 0, 0, -1
*SET,%_FNCNAME%(0,11,1), 0.0, -3, 0, 1, -2, 3, -1
*SET,%_FNCNAME%(0,12,1), 0.0, -1, 0, 50000000, 0, 0, -3
*SET,%_FNCNAME%(0,13,1), 0.0, -2, 0, 1, -3, 1, -1
*SET,%_FNCNAME%(0,14,1), 0.0, 99, 0, 1, -2, 0, 0
FLST,2,1,5,ORDE,1

```

```

FITEM, 2, 4
/GO
SFA, P51X, 1, PRES, %CUBE%

```

Appendix C Simple lock-in Matlab simulation

```

m=5000; %number of data points
i=0:m-1; %sets up a vector from zero to the number of points-1
time=20; %total record time
t=i*(time/m); %time at each point
Tb=100; %allows user to input a background temp
f1=.5;%frequency of the signal
f2=.5;%frequency of the reference signal
A=1;%amplification factor of signal (1 corresponds to a range of 2)
stddev=5;%standard deviation of the noise
fc=2;%cutoff frequency for low-pass Butterworth filter

mult=.5;%multiplier of reference signal. range is 2 with mult of 1
y1=A*sin(2*pi*f1*t)+Tb+stddev*randn(1,m); %signal from device
y2=mult*(sin(2*pi*f2*t));%reference signal
Px=y1.*y2;%multiplied together

order=2;%order of the Butterworth filter
fcnorm=fc/(m/time);%normalized cutoff frequency for filter
[b,a]=butter(order,fcnorm);%gets the input arguments needed for the filter
P=filter(b,a,Px);%passes the multiplied signal through a low-pass Butterworth filter

disp('Average of P: ');%this is essentially the DC signal (the integral
disp(mean(P));
disp('Integral of P divided by total time (should be ~= to mean): ');
trapz(t,P)/time;
disp(trapz);
disp('Average of noisy signal: ');
disp(mean(y1));

disp('Extrapolated range of signal: ');
disp(mean(P)*2/mult);
disp('Actual range of signal: ');
disp(2*A);

subplot(2,3,1);plot(t,y1);title('Signal');
subplot(2,3,2);plot(t,y2);title('Reference Signal');
subplot(2,3,3);plot(t,P);title('Multiplied and through low pass Butterworth filter');

subplot(2,3,4);
plot(t,Px);title('Multiplied signals without low-pass filter');

```

```

%apply a low pass filter to original signal
sigfiltered=filter(b,a,y1);

subplot(2,3,5);
plot(t,sigfiltered);title('Original signal with low-pass filter');

%apply a bandpass signal to original signal

fc_low=.2;
fc_low_norm=fc_low/(m/time);%low cutoff for bandpass filter
[d,c]=butter(order,[fc_low_norm,fc_norm]);
doubfiltered=filter(d,c,y1);
subplot(2,3,6);plot(t,doubfiltered);title('Original signal through Butterworth bandpass filter');

```

Appendix D Lgw file for hole-in-plate simulations

!this program sets up a HIP model to be tested for TSA.
!everything is ready to go except for the loading which must be applied to the top edge
!the solution is set up to work best with a 3Hz load

```

/BATCH
/input,menust,tmp,",,,,,,,,,,,,,1
WPSTYLE,,,,,,,,,0
*SET,length,12*.0254
*SET,width,2*.0254
*SET,thick,0.0254/16
*SET,hole_rad,.25*.0254
*SET,mesh_length,4*.0254

*SET,cycles,1
/PREP7

!set material properties and element type
MPREAD,'steelSIunits','mp','J:\RESEARCH ansys'
ET,1,SOLID226,11
KEYOPT,1,1,11
KEYOPT,1,2,0
KEYOPT,1,4,0
KEYOPT,1,6,0
KEYOPT,1,9,0

!make keypoints
k,1,0,0,0
k,2,width,0,0

```

```

kgen,2,1,2,1,0,length/2-mesh_length/2,0
kgen,2,3,4,1,0,mesh_length,0
kgen,2,1,2,1,0,length,0
kgen,2,1,8,1,0,0,thick

```

```

!make areas

```

```

a,7,8,16,15
a,7,5,13,15
a,5,3,11,13
a,1,3,11,9
a,1,2,10,9
a,2,4,12,10
a,12,14,6,4
a,14,16,8,6
a,5,6,14,13
a,3,4,12,11
a,5,6,8,7
a,3,4,6,5
a,1,2,4,3
a,13,14,16,15
a,11,12,14,13
a,9,10,12,11

```

```

!make volumes

```

```

va,11,1,2,9,8,14
va,12,3,10,7,9,15
va,13,4,5,6,10,16

```

```

!make and then delete the hole

```

```

k,12345,width*.475,length/2,0
WPSTYLE,,,,,,,,1
KWPAVE, 12345
CYL4, , ,hole_rad, , ,thick
VSBV, 2, 4

```

```

!Mesh

```

```

ESIZE,thick*4,0,
MSHAPE,0,3D
MSHKEY,1
FLST,5,2,6,ORDE,2
FITEM,5,1
FITEM,5,3
CM,_Y,VOLU
VSEL, , , ,P51X
CM,_Y1,VOLU
CHKMSH,'VOLU'
CMSEL,S,_Y
VMESH,_Y1
CMDELE,_Y

```

```

CMDELE,_Y1
CMDELE,_Y2
SMRT,6
SMRT,5
MSHAPE,1,3D
MSHKEY,0
CM,_Y,VOLU
VSEL, , , , 5
CM,_Y1,VOLU
CHKMSH,'VOLU'
CMSEL,S,_Y
VMESH,_Y1
CMDELE,_Y
CMDELE,_Y1
CMDELE,_Y2
/UI,MESH,OFF

```

!fully fix keypoint 1, then fix the bottom area (area 5) in y

```

/SOL
FLST,2,1,3,ORDE,1
FITEM,2,1
/GO
DK,P51X, , , ,0,UX,UY,UZ, , , ,
FLST,2,1,5,ORDE,1
FITEM,2,5
/GO
DA,P51X,UY,
FLST,2,20812,1,ORDE,14
FITEM,2,1
FITEM,2,-16724
FITEM,2,16726
FITEM,2,-16979
FITEM,2,16981
FITEM,2,-17237
FITEM,2,17239
FITEM,2,-17384
FITEM,2,17386
FITEM,2,-18187
FITEM,2,18189
FITEM,2,-18618
FITEM,2,18620
FITEM,2,-20818

```

!set initial condition (300K), ref temp, save all substeps

```

IC,P51X,TEMP,300, ,
TREF,300,
OUTRES,ALL,ALL,

```

!transient analysis, set up for a 3Hz load (runs 8 times per cycle)


```

ANTYPE,4
TRNOPT,FULL
LUMPM,0
TIME,cycles/3
AUTOTS,-1
DELTIM,1/24,1/24,1/24,1
KBC,0
TSRES,ERASE

```

Appendix E Matlab hole-in-plate simulation files

```

function t = IRCamera(Temp)
%IRCamera simulates transformation of a surface temperature value to a 16
% Temp is degrees Kelvin
% e = emissivity
% add random noise with mean of 0 and stdev of 0.05 degree K
Temp = Temp + 0.050*randn(size(Temp));
e=0.85;%emmisivity coefficient
m =(2^14)/800;
t = e.*Temp.*m;
% convert to unsigned integer
t = uint16(t);
end

```

```

function S = TES(x,y,ds,a)
%TES Summary of this function goes here
% This function calculates the thermoelastic temperature change
% due to a specific change in stress for a circular hole of radius a
% in an infinite thin plate
% The Input arguments are
% x, coordinate
% y, coordinate
% note coordinates are relative to center of hole
% ds, change of uniaxial tension stress
% a, radius of hole
% calculate radius R from x and y coordinates
R = sqrt(x.^2+y.^2);
% calculate theta from x and y coordinates
theta = atan(y./x);
k = R<=a;
S(k) = 0;%stress is zero in the hole
Sr = 1/2*ds*(1-(a.^2)./(R.^2))+1/2*ds*(1-4*(a.^2)./(R.^2)+3*(a.^4)./(R.^4)).*cos(2*theta);
Sr(k)=0;

```

```

St = 1/2*ds*(1+(a.^2)./(R.^2))-1/2*ds*(1+3*(a.^4)./(R.^4)).*cos(2*theta);
St(k)=0;
S=(Sr+St)*0.000013;%this constant is the coeff. of thermal expansion for steel
% remove the small contribution due to the uniform stress field.
S=S-mean(mean(S));
% assure the temperature in the hole is zero.
S(k)=0;
% set temperature variation relative to an ambient temp of 300 K
S = S +300;
end

```

```

% creates a simulated sequence of image files
[X,Y] = meshgrid(-1.62:0.01:1.61,-1.27:0.01:1.28);
timedepth = 10;
FrameRate=30;
time1 = (0:1/FrameRate:timedepth + 1);
time2 = (1/FrameRate:1/FrameRate:timedepth + (1+1/FrameRate));
time = (time1+time2)/2;
LI = zeros(256,324,timedepth * FrameRate,'double');
pixel = zeros(timedepth * FrameRate,1,'double');
li = zeros(256,324,'double');
P = 10000;
video1=zeros(256,324,timedepth * FrameRate,'uint16');
Stress=P*((1/2+1/2*sin(time2*3*2*pi)-(1/2+1/2*sin(time1*3*2*pi))));

for i=1:timedepth*30
    video1(:,i)=IRCamera(TES(X,Y,Stress(i),.25)).*4;
    % multiply by 4 to take advantage of full span of 16 bit integer
    colormap(jet);
    %m(i) = mean(mean(video1(:,i)));
    LI(:,i)=double(video1(:,i)) ./ 20.4800;
    imagesc(LI(:,i));
    pause(0.033);
end

%lockin section
fc=12;%cutoff frequency (Hz) for low-pass filter
order=2;%order of the Butterworth filter
fcnorm=fc/FrameRate;%normalized cutoff frequency for filter
[b,a]=butter(order,fcnorm);%produces the needed input arguments for the filter algorithm to do a
Butterworth filter

for i= 1:256
    for j = 1:324
        for k=1:timedepth * 30
            pixel(k)=LI(i,j,k)*sin((time(k)+.081)*3*2*pi);

```

```

        end;
        PIXEL=filter(b,a,pixel(:));
        li(i,j)=mean(PIXEL);%averaged image
    end;
    i
end;

imagesc(li);%displays the average image

```

Appendix F Matlab file which performs TSA on truck-based signals

```

% creates a simulated sequence of image files
[X,Y] = meshgrid(-1.62:0.01:1.61,-1.27:0.01:1.28);
timedepth = 40;
FrameRate = 30;
Tc=1/FrameRate;
time1 = (0:Tc:timedepth + 1);
time2 = (Tc:Tc:timedepth + (1+Tc));
time = (time1+time2)/2;
LI = zeros(256,324,timedepth * 30,'double');
pixel = zeros(timedepth * 30,1,'double');
li = zeros(256,324,'double');
P = 1000;
video1=zeros(256,324,timedepth * 30,'uint16');
load('3AxleTruck');
Stress = zeros(timedepth*FrameRate,1);
% create a simulated stress file for 10 consecutive 3 axle truck passages.
for j= 0:119:1190-119
    for i = 1:119
        Stress(i+j) =P*(data(i+1)-data(i));
    end;
end;
% lock in image processing
for i=1:timedepth*30-1
    video1(:, :,i)=IRCamera(TES(X,Y,Stress(i),.25)).*4;
    % multiply by 4 to take advantage of full span of 16 bit integer
    colormap(jet);
    %m(i) = mean(mean(video1(:, :,i)));
    LI(:, :,i)=double(video1(:, :,i)) ./ 20.4800;
    imagesc(LI(:, :,i));
    pause(0.033);
end
for i= 1:256
    for j = 1:324
        for k=1:timedepth * 30 -1

```

```

        pixel(k)=LI(i,j,k)*Stress(k);
    end;
    li(i,j)=mean(pixel);
end;
end;
imagesc(li);

```

Appendix G

Matlab image processing code with idealized sine reference (pp1uva2.m) & phaseshift routine (phaseshift.m)

```

% POST PROCESS IR DATA
% Thermal Stress Analysis
%
% Read Sequence of IR data stored as individual frame files.
% Data in Matrox MIM format
%
% P.A. Fuchs (Fuchs Consulting, Inc.)
% 2/19/12
%
%with additions by Dr. Steve Chase and Matt Kantner

%-----
%THINGS TO CHANGE FOR EACH FILE
%currentpath ~ line 23 (per run)
%zoom window (per specimen) ~line 65
%loadRate (per set) ~ line 33
%-----

% Specify the directory with the image files to process.
% This algorithm assumes that only image files are in the directory
% and that the number of files equals the number of frames in a sequence.
% File format is Matrox binary file format (MIM).
currentPath = 'E:\image_files\D\1';

%-----
% Find the number of frames to process
% Create an array of filenames that make up the image sequence
%currentDirectory = fullfile(matlabroot,'toolbox','images','imdemos');
dirOutput = dir(fullfile(currentPath,'Image*.mim'));
fileNames = {dirOutput.name}';
numFrames = numel(fileNames);
timedepth = 60;

```

```

LoadRate = 3.0277;
%frequency for test TEN ----- 10.025
% test A,C ----- 3.0157
% test B,D ----- 3.0277

%-----

% LOAD FRAMES
% Read the first frame
totalFile = sprintf('%s\\%s',currentPath, fileNames{1});
I = imread(totalFile);

% Make a zero filled array for the sequence
% Fill the first frame in the sequence
video1 = zeros([size(I) numFrames],class(I));
videoNew = zeros([71 55 numFrames],class(I));
LI = zeros(71,55,numFrames);
video1(:,:,1) = I;

% Fill the sequence with data from the individual frame files.
for p = 2:numFrames
    totalFile = sprintf('%s\\%s',currentPath, fileNames{p});
    video1(:,:,p) = imread(totalFile);
end
%-----
%-----
%-----

%PROCESSING

%zoom in on the interesting part
%for all tests with specimen 1 this is (90:160,128:182)
%for all tests with specimen 2(3) it is (99:169,127:181)
%this makes the images 71x55, about 5% the size of the original
zoom=video1(99:169,127:181,:);
clear video1

%subtract an average value from every pixel at each frame to nullify
%long-duration oscillations in the data
for i=1:numFrames
    videoNew(:,:,i) = (zoom(:,:,i)- mean(mean(zoom(:,1:27,i)))).*4;
    LI(:,:,i)=double(videoNew(:,:,i))./50;%converts uint16 to double
end;
%-----
%-----
%-----

%preallocate these values to speed up calculation time

```

```

pixel=zeros(1,numFrames);
li = zeros(71,55);
time = zeros(1,numFrames);

%lock-in algorithm - only apply it to the area around the hole in order to
%cut out uninteresting data, and to speed up processing
ps=0;%phase shift

for i= 1:71
    for j = 1:55
        for k=1:numFrames
            time(k)=k*1/30;
            pixel(k)=LI(i,j,k)*sin(time(k)*LoadRate*2*pi+pi/2+ps);
        end;
        li(i,j)=mean(pixel);
    end;
end;

%display the final image
imagesc(li);

```

```

phaseshift:
ps=input('phase shift: ');

for i= 1:71
    for j = 1:55
        for k=1:numFrames
            time(k)=k*1/30;
            pixel(k)=LI(i,j,k)*sin(time(k)*LoadRate*2*pi+pi/2+ps);
        end;
        li(i,j)=mean(pixel);
    end;
end;

%display the final image
imagesc(li);

```

Appendix H

Excel Macros for MTS data processing

```

Sub primer()
'
' primer Macro
'

```

```

Range("B22:B6121").Select
Selection.Copy
Sheets.Add After:=Sheets(Sheets.Count)
Sheets("Sheet1").Select
Sheets("Sheet1").Name = "export"
Range("A1").Select
Selection.PasteSpecial Paste:=xlPasteValues, Operation:=xlNone, SkipBlanks _
:=False, Transpose:=False
End Sub
Sub to30()
For i = 2 To 6100 Step 39
    Rows(i).Delete
Next
For i = 2 To 6100 Step 38
    Rows(i).Delete
Next
For i = 3 To 6100 Step 37
    Rows(i).Delete
Next
For i = 3 To 6100 Step 36
    Rows(i).Delete
Next
For i = 4 To 6100 Step 35
    Rows(i).Delete
Next
For i = 4 To 6100 Step 34
    Rows(i).Delete
Next
For i = 4 To 6100 Step 33
    Rows(i).Delete
Next
For i = 5 To 6100 Step 32
    Rows(i).Delete
Next
For i = 5 To 6100 Step 31
    Rows(i).Delete
Next
For i = 5 To 6100 Step 30
    Rows(i).Delete
Next
For i = 6 To 6100 Step 29
    Rows(i).Delete
Next
For i = 6 To 6100 Step 28
    Rows(i).Delete
Next
For i = 7 To 6100 Step 27
    Rows(i).Delete
Next
For i = 7 To 6100 Step 26
    Rows(i).Delete
Next
For i = 8 To 6100 Step 25
    Rows(i).Delete
Next
For i = 8 To 6100 Step 24

```

```

    Rows(i).Delete
Next
For i = 8 To 6100 Step 23
    Rows(i).Delete
Next
For i = 9 To 6100 Step 22
    Rows(i).Delete
Next
For i = 9 To 6100 Step 21
    Rows(i).Delete
Next
For i = 10 To 6100 Step 20
    Rows(i).Delete
Next
For i = 10 To 6100 Step 19
    Rows(i).Delete
Next
For i = 11 To 6100 Step 18
    Rows(i).Delete
Next
For i = 11 To 6100 Step 17
    Rows(i).Delete
Next
For i = 12 To 6100 Step 16
    Rows(i).Delete
Next
For i = 12 To 6100 Step 15
    Rows(i).Delete
Next
For i = 12 To 6100 Step 14
    Rows(i).Delete
Next
For i = 13 To 6100 Step 13
    Rows(i).Delete
Next
For i = 13 To 6100 Step 12
    Rows(i).Delete
Next
End Sub

```

Appendix I

Matlab image processing routine with MTS
reference signal (pprealref.m)

```

% POST PROCESS IR DATA
% Thermal Stress Analysis
%
% Read Sequence of IR data stored as individual frame files.
% Data in Matrox MIM format

```



```

%
% P.A. Fuchs (Fuchs Consulting, Inc.)
% 2/19/12
%
%with additions by Dr. Steve Chase and Matt Kantner

%-----
%THINGS TO CHANGE FOR EACH FILE
%currentpath ~ line 23
%zoom window (per specimen) ~line 65
%refsignal file ~ line 80
%-----

% Specify the directory with the image files to process.
% This algorithm assumes that only image files are in the directory
% and that the number of files equals the number of frames in a sequence.
% File format is Matrox binary file format (MIM).
currentPath = 'E:\image_files\A\1';

%-----
% Find the number of frames to process
% Create an array of filenames that make up the image sequence
%currentDirectory = fullfile(matlabroot,'toolbox','images','imdemos');
dirOutput = dir(fullfile(currentPath,'Image*.mim'));
fileNames = {dirOutput.name}';
numFrames = numel(fileNames);
timedepth = 60;

%-----

% LOAD FRAMES
% Read the first frame
totalFile = sprintf('%s\\%s',currentPath, fileNames{1});
I = imread(totalFile);

% Make a zero filled array for the sequence
% Fill the first frame in the sequence
video1 = zeros([size(I) numFrames],class(I));
videoNew = zeros([71 55 numFrames],class(I));
LI = zeros(71,55,numFrames);
video1(:, :, 1) = I;

% Fill the sequence with data from the individual frame files.
for p = 2:numFrames
    totalFile = sprintf('%s\\%s',currentPath, fileNames{p});
    video1(:, :, p) = imread(totalFile);
end
%-----
%-----

```

```

%-----

%PROCESSING

%zoom in on the interesting part
%for all tests with specimen 1 (A,B) this is (90:160,128:182)
%for all tests with specimen 2/3 (C,D) it is (99:169,127:181)
%this makes the images 71x55, about 5% the size of the original
zoom=video1(90:160,128:182,:);
clear video1 %clearing this huge array frees up memory

%subtract an average value from every pixel at each frame to nullify
%long-duration oscillations in the data
for i=1:numFrames
    videoNew(:, :, i) = (zoom(:, :, i) - mean(mean(zoom(:, 1:27, i)))) * 4;
    LI(:, :, i) = double(videoNew(:, :, i)) / 50; %converts uint16 to double
end;
%-----
%-----

%preallocate these values to speed up calculation time
pixel=zeros(1,numFrames);
li = zeros(71,55);

%lock-in algorithm - only apply it to the area around the hole in order to
%cut out uninteresting data, and to speed up processing
refsignal=xlsread('E:\refsignals\A1','A1:A1800');
%change the range to dial in the correct phase shift

%this normalizing routine shifts the mean of the sine wave to zero and
%normalizes it to oscillate from -1 to 1
tozero = refsignal-mean(refsignal); %shift all of the data so that the mean is at zero
rms=sqrt(sum(tozero.^2)/length(tozero)); %calculate the root mean square
peak=rms*sqrt(2); %calculate the peak (only works for sin / cos waves)
normalized=tozero./peak; %normalize the data to be a sin wave oscillating from -1 to 1

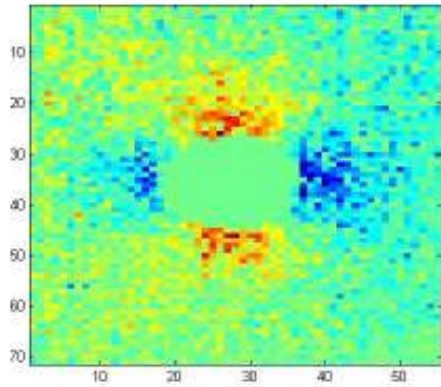
%lock-in
for i= 1:71
    for j = 1:55
        for k=1:numFrames
            pixel(k)=LI(i,j,k)*normalized(k);
        end;
        li(i,j)=mean(pixel);
    end;
end;

%display the final image
imagesc(li);

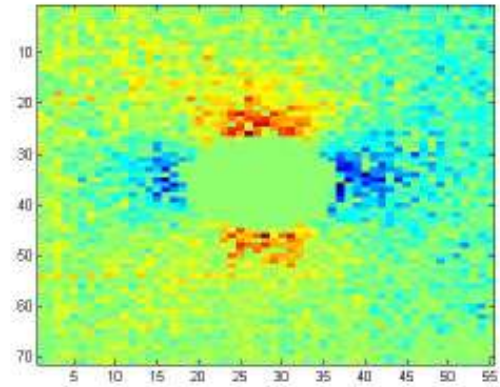
```

Appendix J

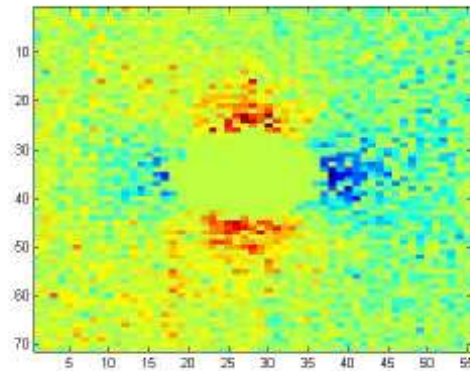
Final Averaged Images from Laboratory Testing



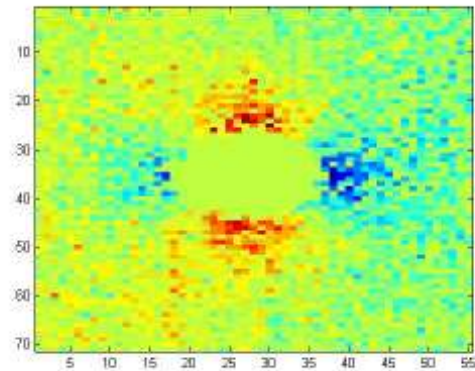
A1 ideal reference



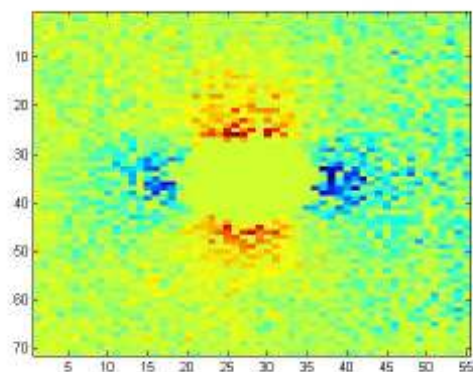
A1 MTS reference



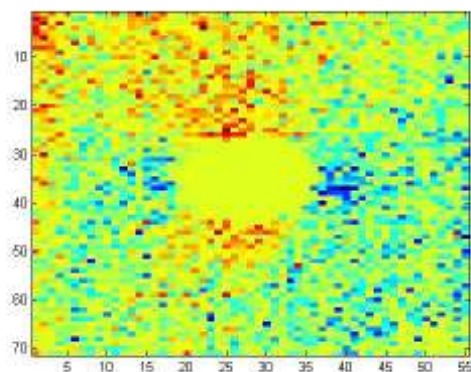
A2 ideal reference



A2 MTS reference

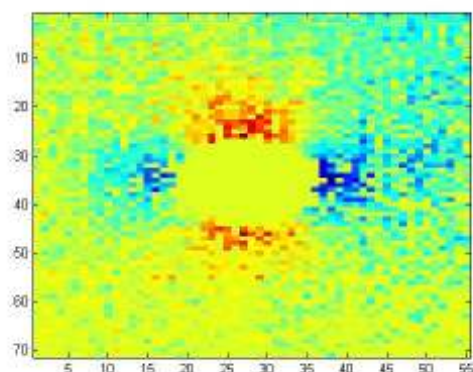


A3 ideal reference

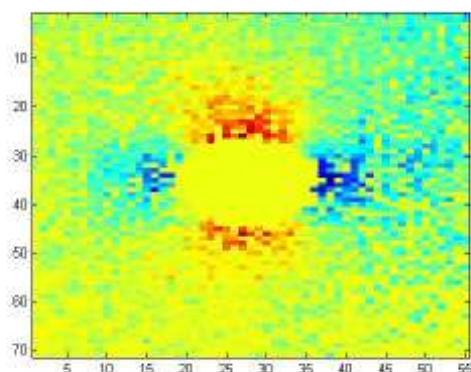


A3 MTS reference

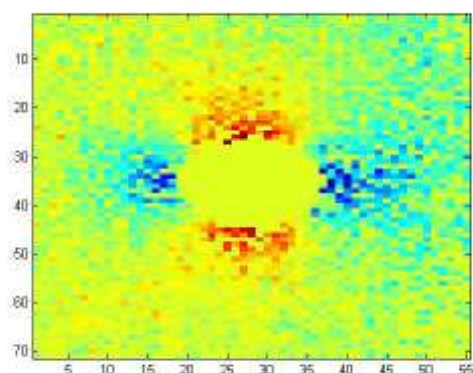
*A3 MTS reference is low-quality because the leads on the MTS output were touching for several seconds



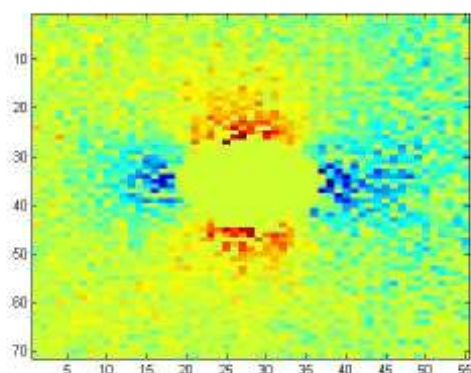
A4 ideal reference



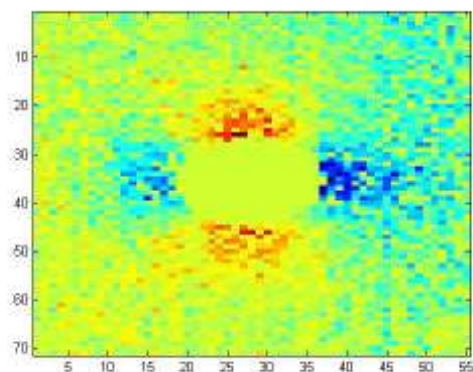
A4 MTS reference



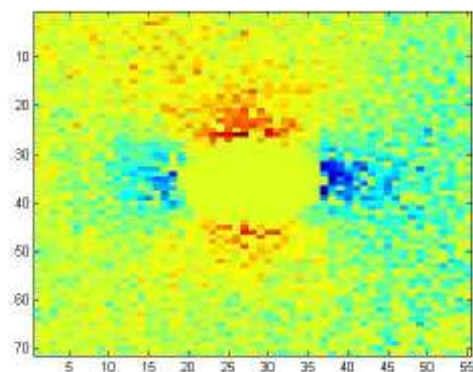
A5 ideal reference



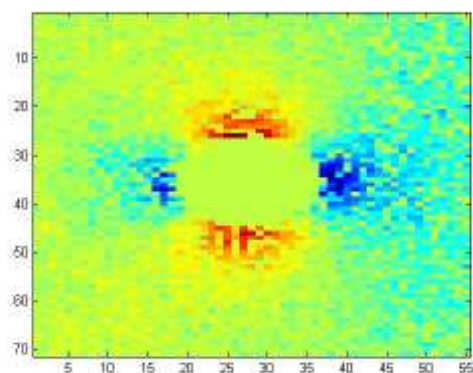
A5 MTS reference



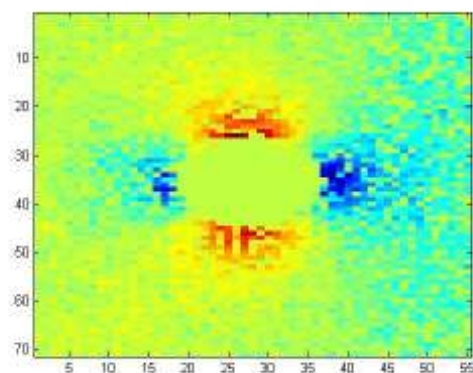
B1 ideal reference



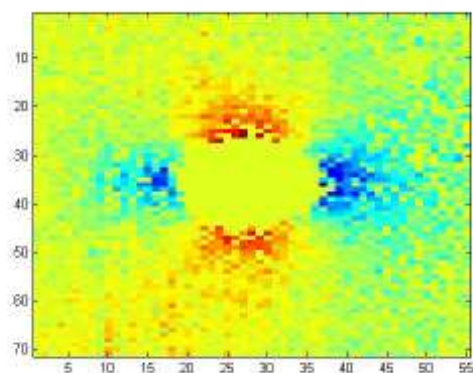
B1 MTS reference



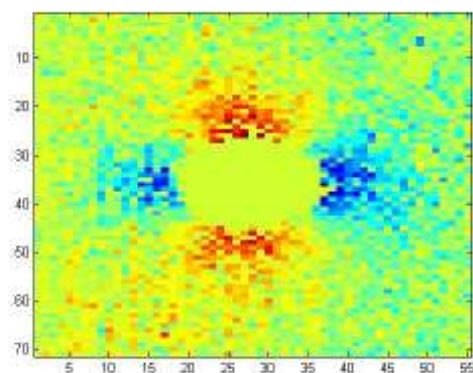
B2 ideal reference



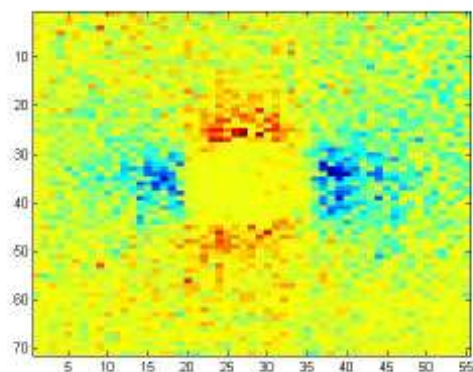
B2 MTS reference



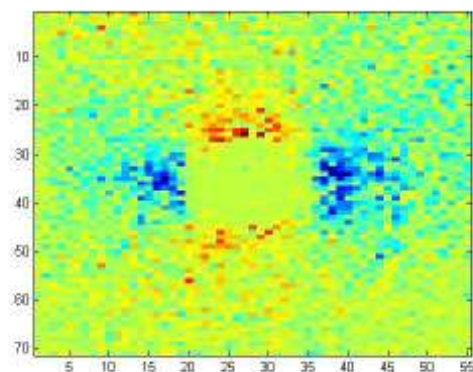
C1 ideal reference



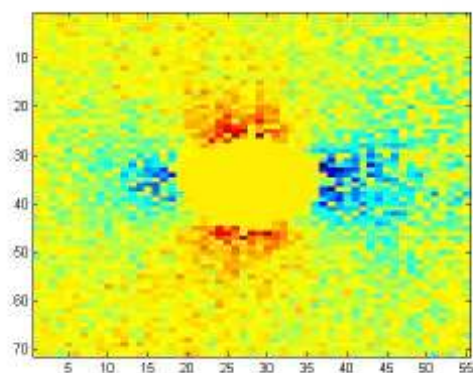
C1 MTS reference



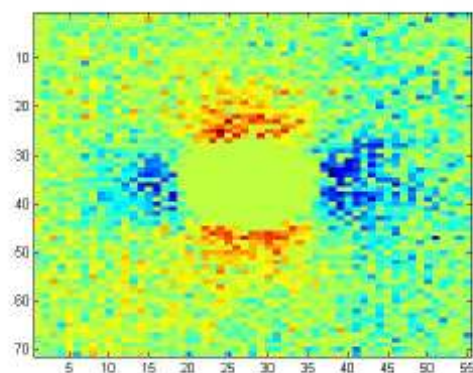
C2 ideal reference



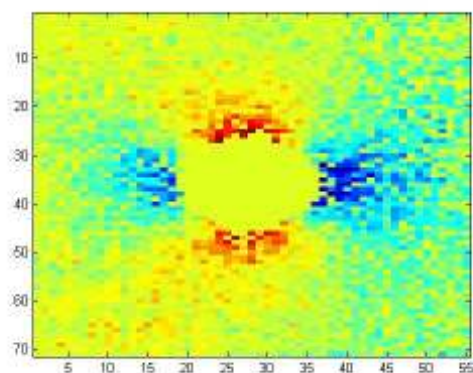
C2 MTS reference



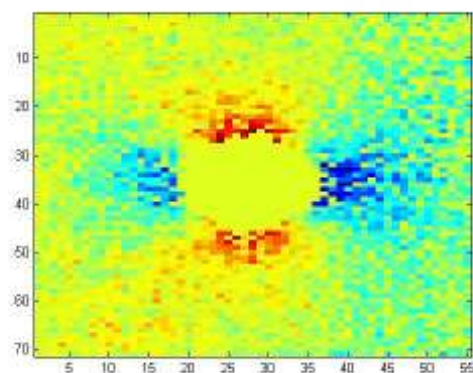
C3 ideal reference



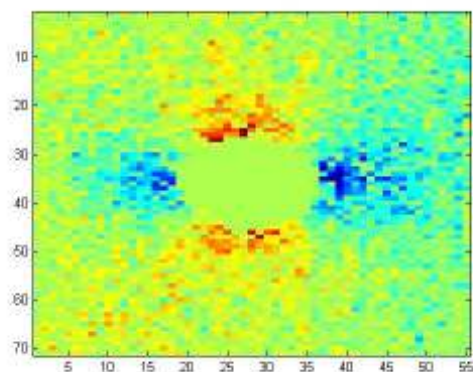
C3 MTS reference



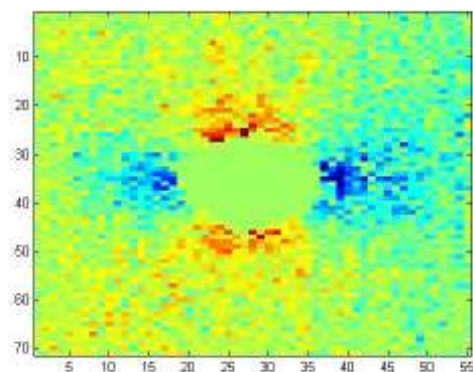
C4 ideal reference



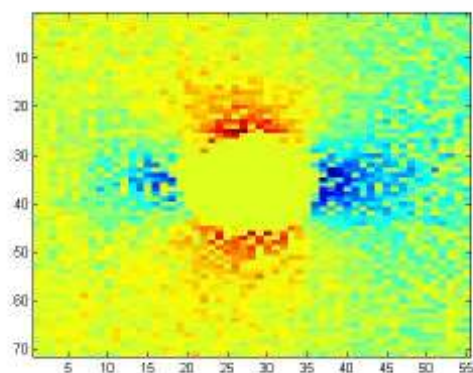
C4 MTS reference



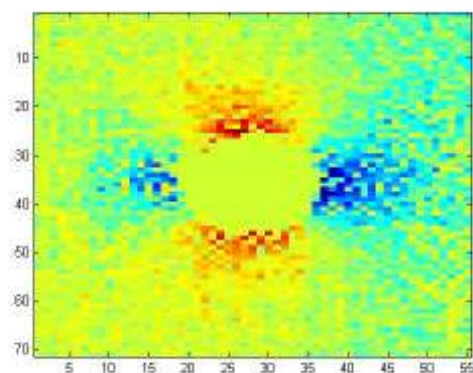
C5 ideal reference



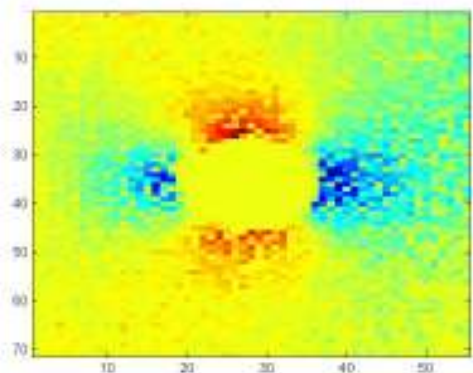
C5 MTS reference



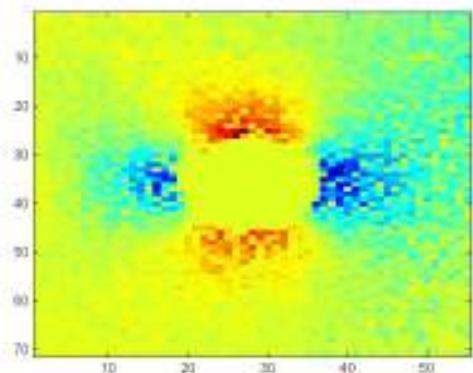
D1 ideal reference



D1 MTS reference



D2 ideal reference

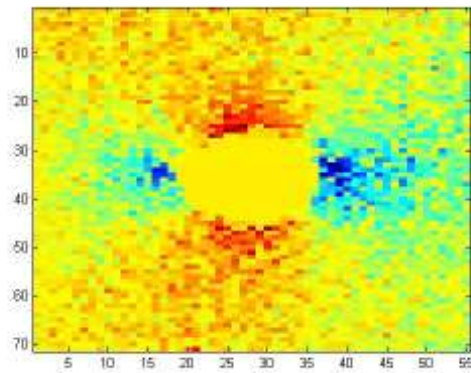


D2 MTS reference

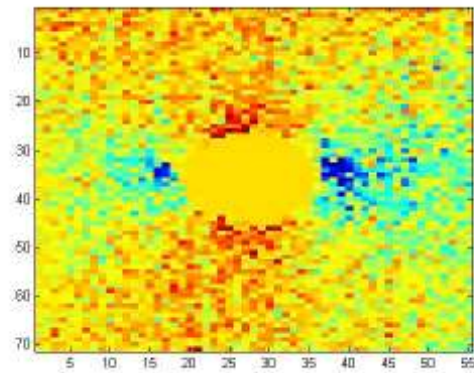
*both D2 images are 180 second averages

Appendix K Effect of Phase-shift on Final Images

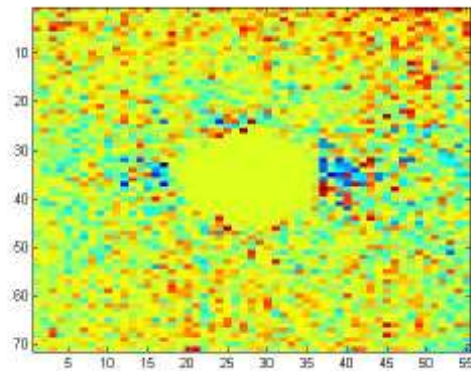
All of these images come from test D2.



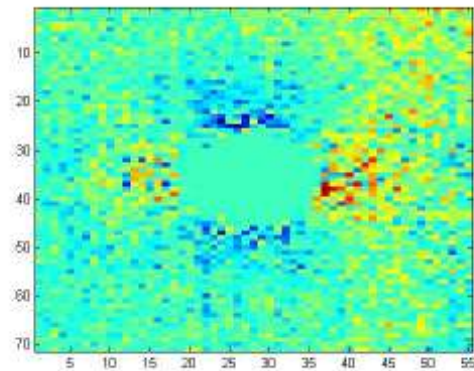
Phase Shift = 0



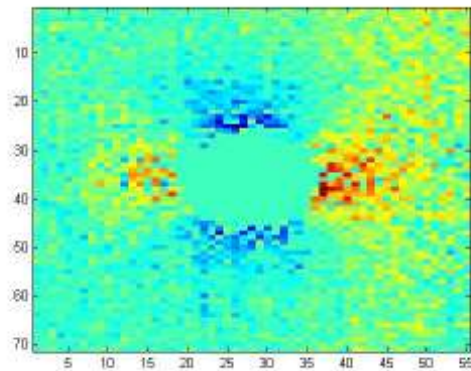
Phase Shift = 0.1π



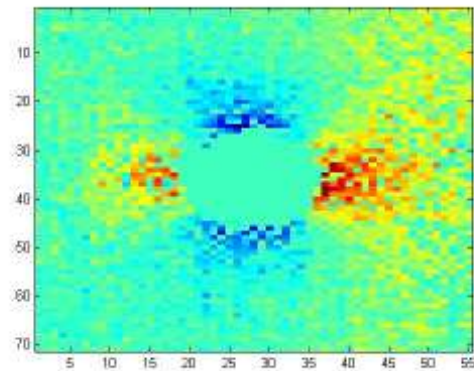
Phase Shift = 0.2π



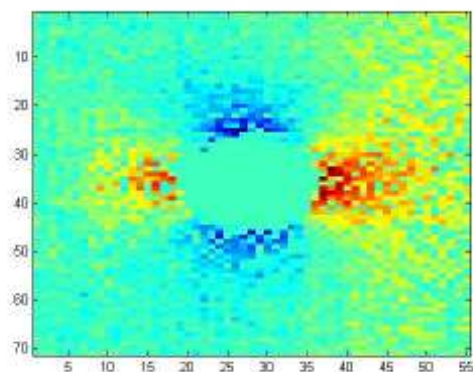
Phase Shift = 0.3π



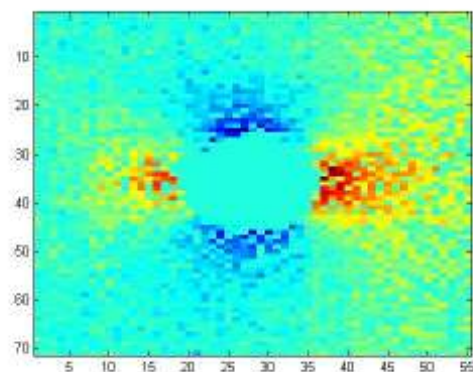
Phase Shift = 0.4π



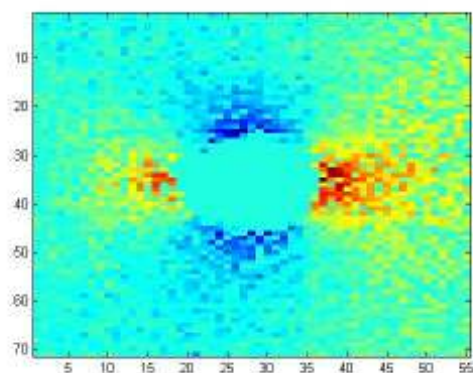
Phase Shift = 0.5π



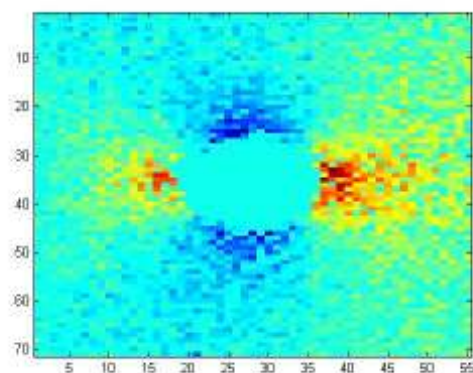
Phase Shift = 0.6π



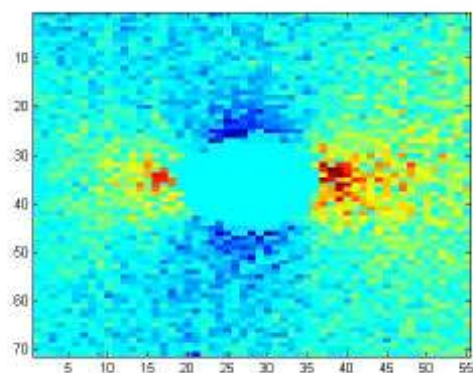
Phase Shift = 0.7π



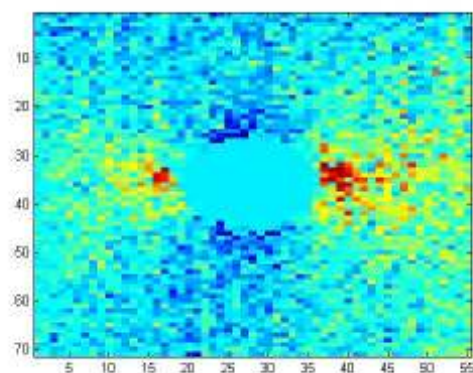
Phase Shift = 0.8π



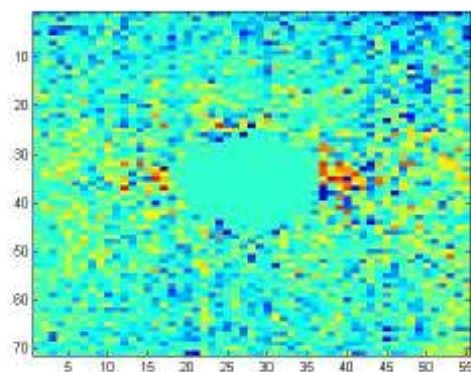
Phase Shift = 0.9π



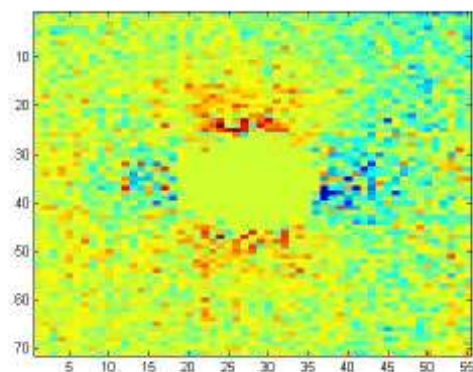
Phase Shift = π



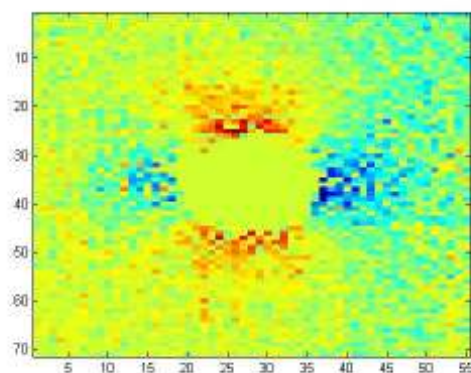
Phase Shift = 1.1π



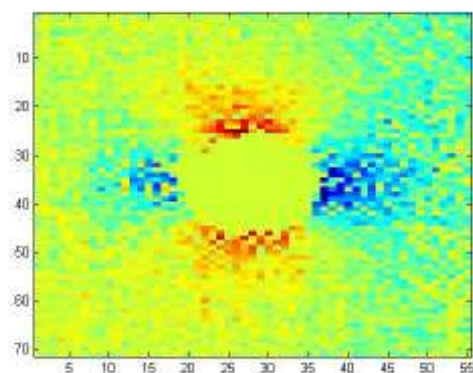
Phase Shift = 1.2π



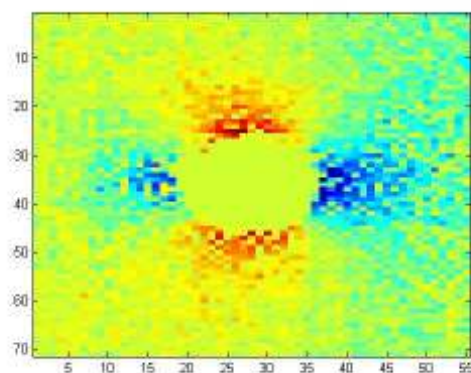
Phase Shift = 1.3π



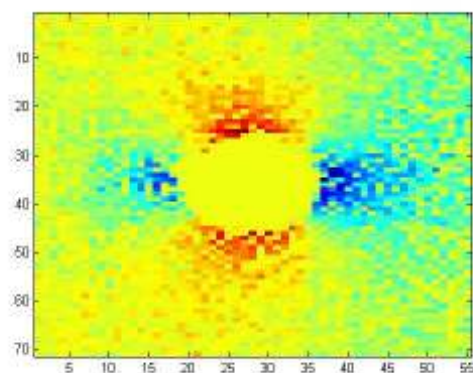
Phase Shift = 1.4π



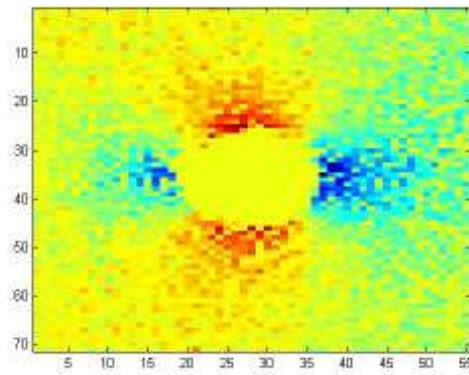
Phase Shift = 1.5π



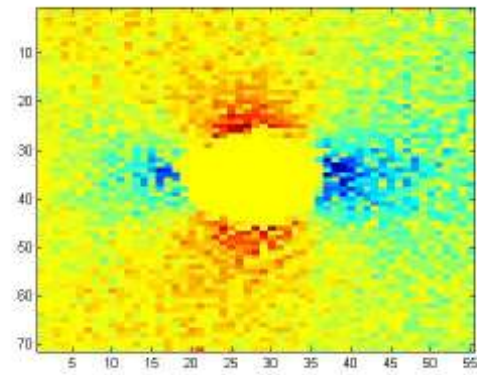
Phase Shift = 1.6π



Phase Shift = 1.7π



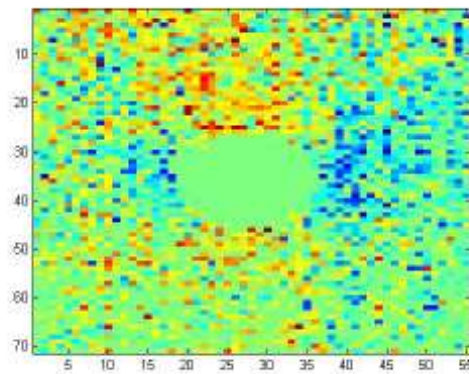
Phase Shift = 1.8π



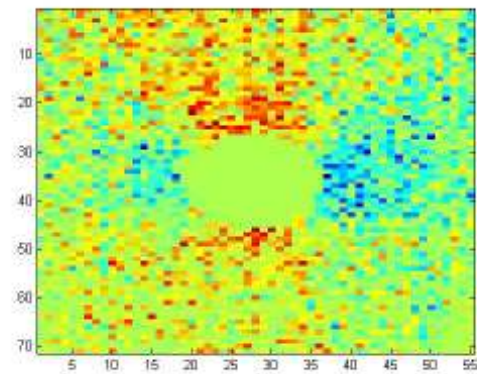
Phase Shift = 1.9π

Appendix L Effect of Averaging Time Duration on Final Images

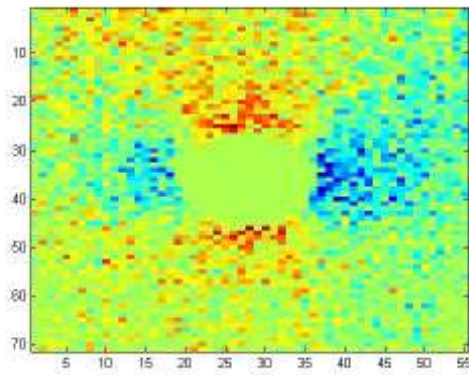
All images taken from test D2 with a 1.75π phase-shift



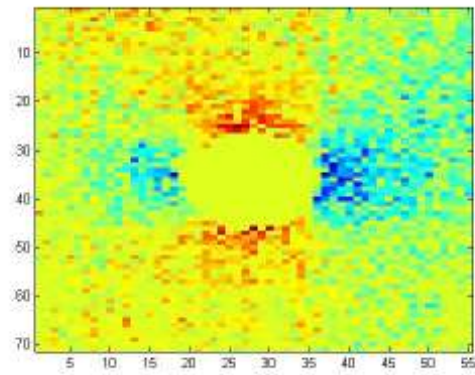
Averaging Time Duration = 1 s



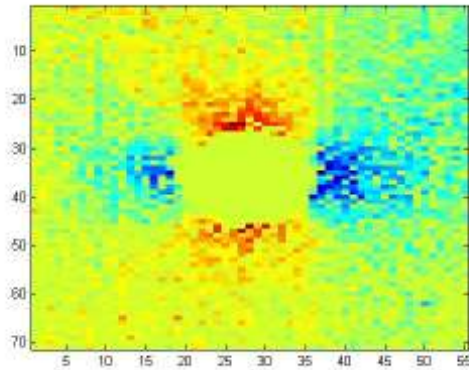
Averaging Time Duration = 2 s



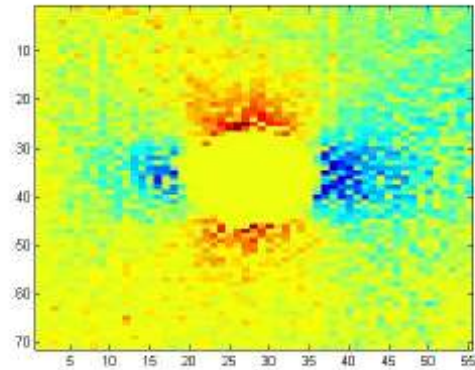
Averaging Time Duration = 5 s



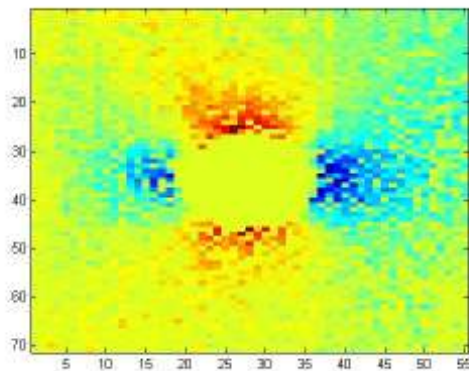
Averaging Time Duration = 10 s



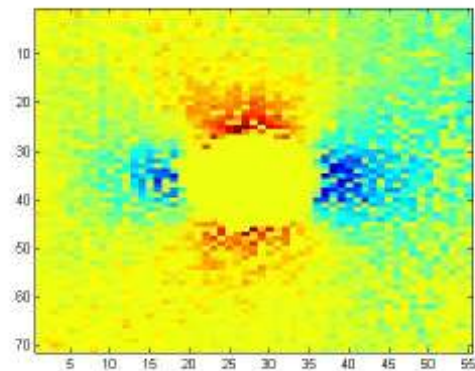
Averaging Time Duration = 20 s



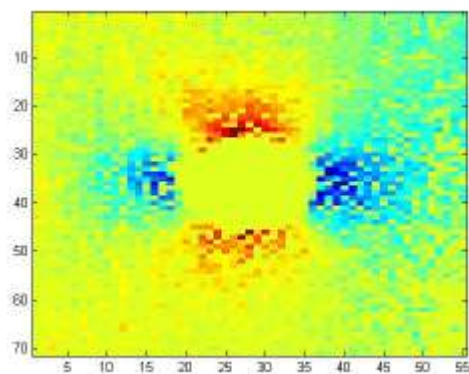
Averaging Time Duration = 30 s



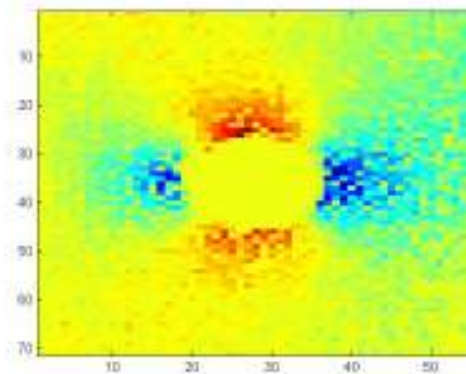
Averaging Time Duration = 45 s



Averaging Time Duration = 60 s



Averaging Time Duration = 90 s



Averaging Time Duration = 180 s

Works Cited

- (AASHTO), A. A. (July 2008). *Bridging the Gap*.
- ANSYS, Inc. (n.d.). 14.222. SOLID226 - 3-D 20-Node Coupled-Field Solid. Canonsburg, PA.
- ANSYS, Inc. (2010). ANSYS Mechanical APDL Structural Analysis Guide. Canonsburg, PA.
- ANSYS, Inc. (n.d.). SOLID226. Canonsburg, PA.
- Dulieu-Barton, J. (1999). Introduction to Thermoelastic Stress Analysis. *Strain*, 35(2).
- Federal Highway Administration. (2010). *Fracture Critical Inspection Techniques for Steel Bridges*. Arlington, VA.
- Fisher, J. W., Jin, J., Wagner, D. C., & Yen, B. T. (1990). *Distortion-Induced Fatigue Cracking in Steel Bridges*. Washington, D.C.: Transportation Research Board.
- FLIR Systems, Inc. (2008). *FLIR A325 Thermal Camera Data Sheet*. Retrieved January 17, 2012, from www.flira325.com: <http://www.flira325.com/PDF/flir-a325-thermal-camera-datasheet.pdf>
- Guinon, J., Ortega, E., García-Antón, J., & Pérez-Herranz, V. (n.d.). Lock-In Amplifier Response Simulation Using Mathcad. Valencia, Spain.
- Haldorsen, L. (1998). *Thermoelastic Stress Analysis System Developed for Industrial Applications*. Aalborg, Denmark: Aalborg University.
- Hardwood, N., & Cummings, W. (1991). *Thermoelastic Stress Analysis*. Bristol, England: IOP Publishing Ltd.
- Kaplan, H. (2007). *Practical Applications of Infrared Thermal Sensing and Imaging Equipment*. Bellingham, Washington: SPIE.
- Pilkey, W. D. (1997). *Peterson's Stress Concentration Factors (2nd Edition)*. John Wiley & Sons.
- Timoshenko, S., & Goodier, J. (1951). *Theory of Elasticity (2nd Edition)*. McGraw-Hill Book Company, Inc.
- URS Corporation. (2011). *Strain Measurement Summary Report: I-70 EBR Bridge over Antietam Creek, Hagerstown, Maryland*. Hunt Valley, Maryland.